

ALMA MATER ALBERTINA LUDOVICIANA  
FREIBURG

MASTER THESIS

---

Comparison of quantum sensors for magnetic fields using diamond NV<sup>-</sup> centers and trapped  $^{25}\text{Mg}^+$  ions

---



Author:  
Ole Pikkemaat

Supervision:  
Prof. Dr. Tobias Schätz  
Apurba Das

Freiburg, 19.07.2024



**Selbstständigkeitserklärung**

Hiermit versichere ich, die eingereichte Masterarbeit selbstständig verfasst und keine anderen als die von mir angegebenen Quellen und Hilfsmittel benutzt zu haben. Wörtlich oder inhaltlich verwendete Quellen wurden entsprechend den anerkannten Regeln wissenschaftlichen Arbeitens (lege artis) zitiert. Ich erkläre weiterhin, dass die vorliegende Arbeit noch nicht anderweitig als Masterarbeit eingereicht wurde.

Ort, Datum ..... Unterschrift .....

## Abstract

This thesis is about the comparison of  $B$ -field quantum sensors from two distinct platforms, namely the trapped  $^{25}\text{Mg}^+$ -ion and the  $\text{NV}^-$ -center in diamond. Magnetic fields were sensed with relative uncertainties of  $2.1 \times 10^{-6}$  and  $> 10^{-3}$ , respectively. A new algorithm was employed to calculate the  $B$ -field strength for the diamonds based on the linear Zeeman effect. Further, also off-diagonal influences of the B-field on the  $\text{NV}^-$ -centers spin-1 Hamiltonian were identified. As a more 'hands on' part of the thesis, a magnetic field setup for an future ion trap was designed and assembled.

# Contents

<b>List of Figures</b>	i
<b>List of Tables</b>	ii
<b>1 Introduction</b>	1
<b>2 Methods</b>	1
2.1 Important specifications of a sensor . . . . .	1
2.2 Classical systems as sensors . . . . .	2
2.3 Quantum systems as sensors . . . . .	2
2.4 The Hall sensor and magnetic field setup . . . . .	3
2.4.1 The principle of the Hall sensor . . . . .	3
2.4.2 The magnetic field for $^{25}\text{Mg}^+$ -ion-trapping . . . . .	5
2.5 Implementation of the magnetic field setup at Octagon . . . . .	6
2.5.1 The magnetic field of ring magnets and coils . . . . .	9
2.5.2 The test setup . . . . .	10
2.6 Properties of the $^{25}\text{Mg}^+$ ion . . . . .	11
2.6.1 The Ramsey sequence . . . . .	13
2.6.2 The frequency scan . . . . .	14
2.7 The Bermuda experiment . . . . .	14
2.7.1 The uncertainties in trapped ion experiments . . . . .	16
2.8 Properties of the NV-centers in diamond . . . . .	17
2.8.1 Energy level structure . . . . .	18
2.8.2 The spin 1 Hamiltonian of the NV-center ground state . . . . .	20
2.8.3 The ODMR technique . . . . .	21
2.9 The diamond experiment setup . . . . .	22
<b>3 Establishing a stable magnetic field setup for the Octagon ion trap vacuum chamber</b>	25
3.1 Calibration and systematics . . . . .	25
3.1.1 Systematic influence of the Hall sensors current supply . . . . .	25
3.1.2 Positioning of the Hall sensor . . . . .	25
3.2 Choosing a suitable ring magnet thickness . . . . .	27
3.3 Tuning parameters towards $B = 109.64\text{ G}$ . . . . .	29
<b>4 The <math>^{25}\text{Mg}^+</math> ion as quantum sensor</b>	30
4.1 Coherence time extraction . . . . .	30
4.2 $B$ -field estimation . . . . .	36
4.3 Sensitivity of the $ 3, 3\rangle \leftrightarrow  2, 2\rangle$ transition . . . . .	37

<b>5 The diamond NV-center as quantum sensor</b>	<b>41</b>
5.1 System characterization . . . . .	41
5.1.1 Laser calibration . . . . .	41
5.1.2 Contrast and SNR vs. power . . . . .	41
5.1.3 Noise floor . . . . .	44
5.1.4 The microwave and the spectrum analyser . . . . .	44
5.1.5 Time to frequency conversion . . . . .	48
5.1.6 Temperature influence . . . . .	50
5.2 Results . . . . .	51
5.2.1 Lorentzian fits for the data . . . . .	52
5.2.2 The linear Zeeman effect . . . . .	54
5.2.3 $B_0$ reconstruction . . . . .	54
5.2.4 Other B-field related influences . . . . .	60
<b>6 Summary and Outlook</b>	<b>63</b>
<b>Appendix</b>	<b>68</b>

## List of Figures

1	The Hall effect . . . . .	4
2	Establishment of a stable hybrid magnetic field setup . . . . .	5
3	Model of the Octagon vacuum chamber . . . . .	6
4	The magnet-and-coil-fixer . . . . .	7
5	Magnet holder . . . . .	7
6	The magnet-and-coil-fixer mounted to the vacuum chamber . . . . .	8
7	Coil overgrowth of the vertical coil pair . . . . .	9
8	The test setup for the coils and magnets . . . . .	10
9	Breit-Rabi formula for the ground state manifold . . . . .	12
10	Transition frequencies . . . . .	12
11	The Ramsey sequence . . . . .	14
12	Frequency scan sequence . . . . .	15
13	Energy level hyperfine structure and laser transitions of the $^{25}\text{Mg}^+$ ion . . . . .	16
14	The lattice structure in Diamond . . . . .	17
15	Energy level structure of the NV <sup>-</sup> center in a diamond . . . . .	19
16	Fluorescence spectrum of the NV-centers in diamond . . . . .	20
17	0 G ODMR example . . . . .	22
18	Electric field of the coplanar waveguide . . . . .	23
20	Systematic influence of the Hall sensors current supply . . . . .	25
21	Axial measurement of the $B$ -field strength . . . . .	26
22	Radial measurement of the $B$ -field strength . . . . .	27
23	The relative magnetic field around the center of the 16 mm magnets . . . . .	28
24	The relative magnetic field around the center of the 20 mm magnets . . . . .	29
25	$B$ -field change per turn of the magnet . . . . .	31
26	$B$ -field change per current of the coils . . . . .	32
27	Phase scan for fixed $t_{\text{Ramsey}}$ . . . . .	34
28	Coherence time extraction . . . . .	35
29	$\Delta\omega$ extraction . . . . .	37
30	Exemplary sinc function fit . . . . .	39
31	Linear impact of the coil current $I_{Z\text{coil}}$ on the $B$ -field . . . . .	40
32	Measured ion $B$ -field sensitivity . . . . .	40
33	Excitation laser calibration . . . . .	42
34	Contrast and SNR vs. power . . . . .	43
35	Technical noise floor . . . . .	44
36	Circuits for MW signal strength estimation . . . . .	45
37	Microwave signal of the setup . . . . .	46
38	Circuits for MW back-reflected signal strength estimation . . . . .	47
39	Back-reflected MW signal of the waveguide . . . . .	48
40	Start, stop and additional sweep time estimation . . . . .	49
41	Temperature change . . . . .	50
42	All ODMR signals . . . . .	51

43	8-Lorentzian fit . . . . .	52
44	Dip position change under $B$ -field . . . . .	53
45	$\Delta\omega$ vs. $B_{\text{set}}$ . . . . .	55
46	The diamond lattice coordinate system . . . . .	56
47	Coarse $B_0$ calculation . . . . .	57
48	Fine $B_0$ calculation . . . . .	58
49	Redefinition of the G/A value for the large coil . . . . .	60
50	Shift of the center frequency dependent on the $B$ -field . . . . .	61
51	Center frequency shift possibilities . . . . .	62
52	Appendix: Blurred ODMR signal . . . . .	68
53	Appendix: center shift due to different coils . . . . .	69
54	Appendix: Gamma variation vs B-Field . . . . .	70
55	Appendix: Amplitude variation vs B-Field . . . . .	70
56	Appendix: Height variation vs B-Field . . . . .	71

## List of Tables

1	Transition properties . . . . .	11
2	Current control voltage conversion . . . . .	38
3	Recalculated B-field values from ODMR signal . . . . .	59
4	Magnetic field setup summary . . . . .	63
5	Summary of the quantum sensor properties . . . . .	64

## 1 Introduction

As soon as the power of observation of mankind based on the human senses failed to explain a phenomena, tools were employed to measure or characterize it or alternatively, it was worshipped as a deity. Over the centuries and in a more sophisticated and technical way, one could call this a sensor. From everyday use to highly specific applications, sensors are integral part of human, and for the latter case, a physicists life. With the establishment of quantum mechanics, people started developing techniques exploiting the quantum nature of objects to sense certain quantities. An very early example is the Rabi oscillation to measure the nuclear magnetic moment introduced by [Rabi et al., 1938]. His successor Ramsey employed the famous Ramsey sequence [Ramsey, 1950], which is still in use today, also in this thesis using a trapped ion as sensor. With the detection of single NV<sup>-</sup> centers in diamond by Gruber et al. in 1997, the field of quantum technology using diamonds became wide [Doherty et al., 2013]. In this thesis, both platforms are employed and compared as quantum sensors to detect magnetic fields. In a more 'hands on' part of the thesis, a magnetic field setup for a vacuum chamber was designed and established.

## 2 Methods

This section provides all needed definitions, physical background and measurement methods to describe the work of this thesis. It starts with an overview of sensor specifications, followed by definitions of classical and quantum sensors. Last, the three platforms used as sensors are introduced with their physical motivation to use them for sensing and the measurement protocols matching to do so.

### 2.1 Important specifications of a sensor

The purpose of a sensor is to detect properties of a physical quantity  $Q$ . For scalar fields like temperature, the strength of it is of interest, while for vector fields like electric or magnetic fields, also the orientation can be important. Logically, a sensor needs to interact with the physical quantity, providing an measurable output  $O$  like an electric current or voltage. Ideally, there are well defined correlations. Expressed with formulas, one defines the change of the sensor output with respect to the change of the physical quantity  $Q$  as sensitivity  $S$

$$S = \frac{\partial^p O}{\partial Q^p} \quad (2.1)$$

where  $p$  is the order of the interaction. Linear ( $p = 1$ ) and quadratic ( $p = 2$ ) responses are the most common and easiest to handle.

Next to define is the operating range of the sensor, which is the range of  $Q$ , in which the sensitivity stays for example linear. In frequency detection, this is also known as bandwidth of the sensor.

Further, all kinds of noises disturb the sensor's output signal, blurring the measured signal. As a quality factor, the signal-to-noise ratio (SNR) is established as the ratio of their amplitudes

$$\text{SNR} = \frac{A_{\text{Signal}}}{A_{\text{Noise}}}. \quad (2.2)$$

A good representation for the noise amplitude can be the (averaged) uncertainty of the signal. Setting the SNR equal one and finding expressions for both amplitudes gives rise to the smallest detectable signal of the sensor. Although many other properties of sensors can be defined and studied, for the sake of this thesis these three are sufficient.

## 2.2 Classical systems as sensors

Classical sensors are using classical physical systems, exploiting mechanical, electrical and optical effects, to detect and measure all kinds of environmental variables. These sensors operate based on principles of classical physics and are widely relevant from a daily use to a high precision industry and research standard, due to their reliability, precision, and established technology. To push the limits of the classical sensors, in the last decades numerous quantum platforms have been established to archive even higher precision. Their definition is object of the next chapter.

## 2.3 Quantum systems as sensors

Any kind of quantum system is prone to external influences, which mainly limits the applications in quantum simulation and computation. For quantum sensing, this disadvantage is turning into the central feature of the field, exploiting these quantum systems as excellent sensors. To call a system a quantum sensor, there are four criteria which have to be satisfied. This subsection is mainly derived from [Degen et al., 2017].

The first three match with three of the original DiVincenzo criteria for quantum computing [DiVincenzo, 2000], where the fourth attribute is specific to quantum sensing:

1. The quantum system has discrete, resolvable energy levels. Most of the times, like in this thesis, there is a focus on two-level systems with a ground state  $|0\rangle$  and an excited state  $|1\rangle$ , separated by a transition energy  $E = \hbar\omega$
2. It must be possible to initialize the quantum system into a well-known state and to read out its state afterwards.
3. The quantum system can be coherently manipulated, typically by time-dependent fields.
4. The quantum system needs to interact with the physical quantity  $Q(t)$  one wants to measure. This coupling is quantified by the coupling parameter  $\gamma =$

$\frac{\partial^p E}{\partial Q^p}$ , relating the change of the energy to the change of  $Q(t)$ . Usually, this change is of linear or quadratic order ( $p = 1$  or  $p = 2$ , respectively). This interaction leads to a relative shift of or a transition rate  $\Gamma$  between the two energy levels.

Further, quantum sensors can be split into three different types:

I is a quantum object, which is defined by quantized energy levels like electronic or spin states, to measure a classical or quantum physical quantity.

II relies on quantum coherence (wavelike spatial or temporal superposition states)

III can be of both types I or II with the important addition that quantum entanglement is involved to improve the sensitivity of the measurement.

Note that the sort of measurement also influences the type assignment of the quantum sensor, for example  $B$ -field measurements with the NV-centers of diamond. Using an optically detected magnetic resonance (ODMR) signal like in [section 5](#), makes it a type I quantum sensor, while applying the Ramsey sequence relying on temporal superposition states to the NV-centers matches the description a type II sensor (e.g. shown in [Pham, 2013]).

## 2.4 The Hall sensor and magnetic field setup

### 2.4.1 The principle of the Hall sensor

The classical sensor important for the first part of this thesis is based on the Hall effect, introduced by Edwin H. Hall in 1879 [Hall, 1879]. It describes the behaviour of a current through a wire or thin plate, when it is exposed to an external magnetic field.

Applying an external magnetic field  $B$  to a thin plate with a current, the Lorentz force drags the moving  $e^-$  in the manner of the right hand rule to one side of the wire, as seen in [Figure 1](#). Due to this charge anisotropy an electric field is building up, in directionality opposing the resulting Lorentz force, until both compensate each other. Resulting from the electric field, a constant measurable voltage  $U_H$  between the two sides of the wire remains, which is proportional to the external  $B$ -field and described by [Demtröder, 2013]

$$U_H = \frac{I \cdot B}{n \cdot e \cdot d} = S \cdot B, \quad (2.3)$$

where  $I$  is the applied current,  $n \cdot e$  the number of electron charges and the  $d$  the thickness of the plate in direction of the  $B$ -field. These are defined as a proportional factor  $S = U_H/B$ , the sensitivity of the sensor. Usually, one wants to maximise the sensitivity, here possible e.g. by reducing the thickness  $d$  or increasing  $I$ .

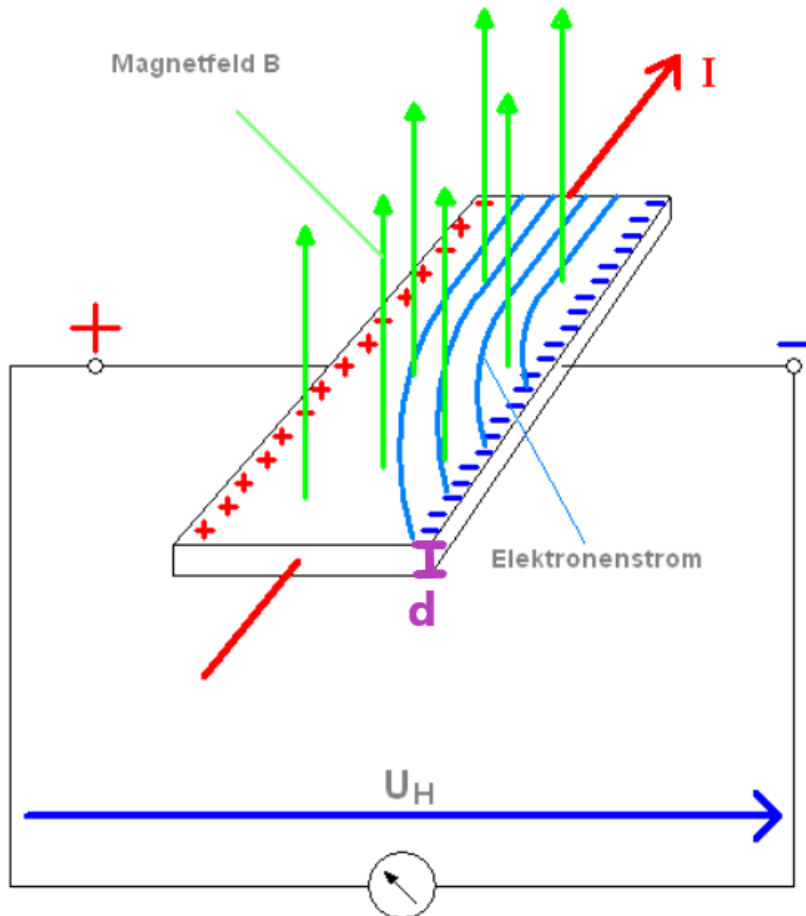


Figure 1: The Hall effect [Schmid-Gaiser, 2024]. The magnetic field  $B$  (green) penetrates the plate of thickness  $d$  (purple) with assigned current  $I$  (red). The Lorentz force drags the electrons to the side of the plate (blue curve), forming the opposing E-field (red plus/blue minus), from which the potential difference can be measured as  $U_H$ . Note that in this representation the current's direction is chosen in the technical current direction.

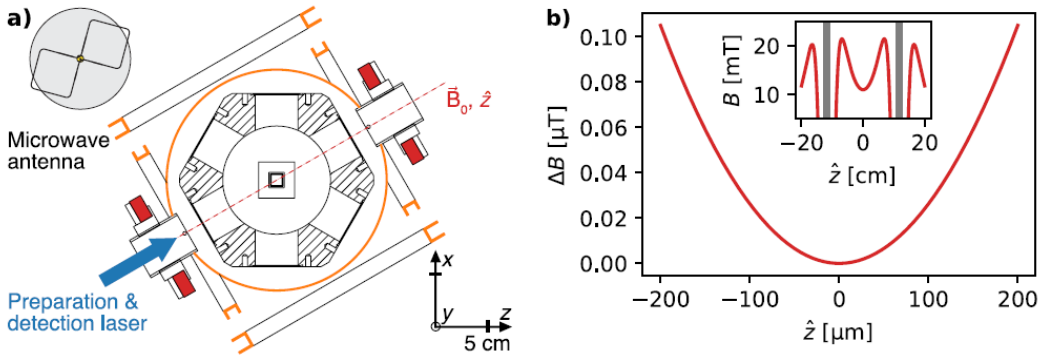


Figure 2: Establishment of a stable hybrid magnetic field setup [Hakelberg et al., 2018]. a) The permanent ring magnets (red) define the quantization axis of the  $B$ -field, while three coil pairs in near Helmholtz configuration (orange) allow fine tuning of the  $B$ -field. The need of strong coils with high currents and therefore lots of heat development becomes obsolete due to the permanent magnets. The ring-like geometry of the magnets allows laser guidance into the vacuum chamber parallel to the quantization axis of the field. b) Numerical calculations of the resulting axial  $B$ -field (inset shows larger region with the magnets as grey bars) show a spherical volume with diameter of  $d_{sv} = 150 \mu\text{m}$ , where  $\Delta B/B(0) \leq 1 \cdot 10^{-6}$ .

#### 2.4.2 The magnetic field for $^{25}\text{Mg}^+$ -ion-trapping

From the side of quantum simulation, one is interested in stable, long-living qubits, being able to perform multiple quantum operations or study long-term dynamics without being limited by short decoherence times of the system. Especially long-lived are the so called clock transitions, which are at a certain magnetic field strength barely influenced by magnetic field fluctuations. Hakelberg et al. showed for the clock transition of the trapped  $^{25}\text{Mg}^+$ -ion at a magnetic field strength of  $B = 109.64 \text{ G}$  a coherence time of almost 7 s [Hakelberg et al., 2018]. Further information regarding the choice of magnetic field and information about the  $^{25}\text{Mg}^+$ -ion can be found in subsection 2.6. Hakelberg et al. also introduced a magnetic field design consisting of permanent magnets for the main magnetic field instead of using high power coils. Latter produce lots of heat and therefore cause an instability of the magnetic field, which leads to shorter coherence times. The first part of this thesis focuses to building such a magnetic field setup for a similar ion trap vacuum chamber, the Octagon. The principle of the magnetic field is presented in Figure 2. The main magnetic field is provided by a pair of ring-shaped permanent magnets, while a Cartesian setup of three coil pairs allows for minor changes and stabilisation of the field.

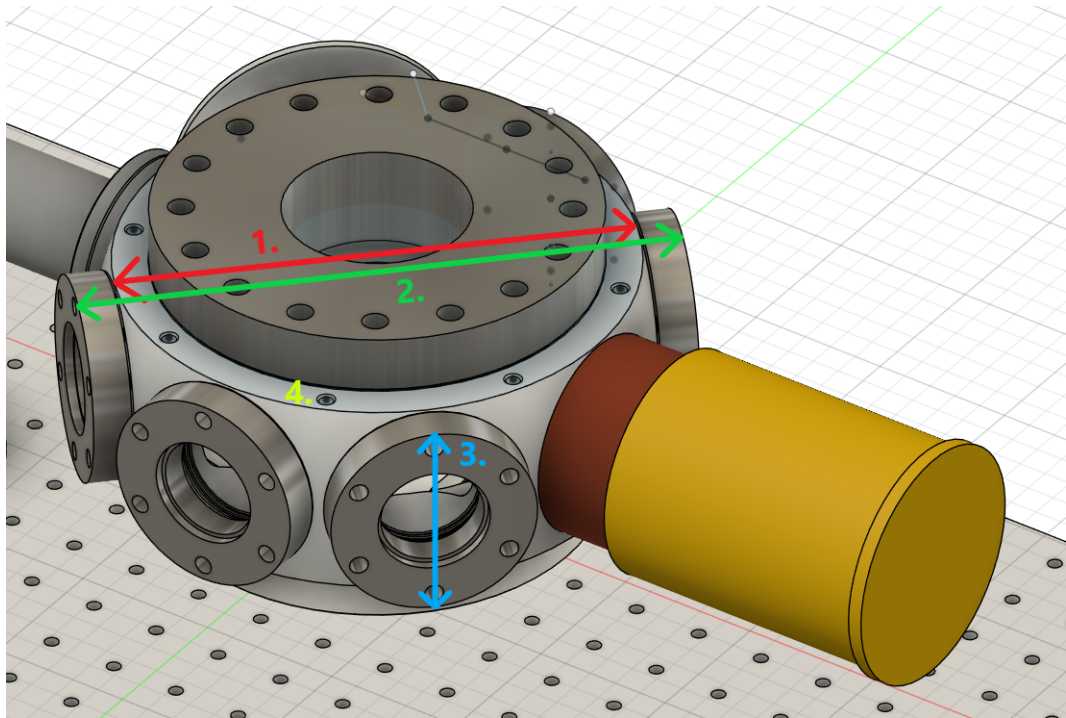


Figure 3: Model of the Octagon vacuum chamber from Fusion360. The most important dimensions for the  $B$ -field setup are the diameter of the chamber (1.) to be 176.8 mm, the distance from window to window (2.) is 216.8 mm. Onto the lateral windows (3.) the permanent magnets and two side coil pairs are mounted, therefore the diameter of these windows (70 mm) is of importance. The top-bottom coil pair can be mounted to the screw holes on top and bottom of the chamber (4.).

## 2.5 Implementation of the magnetic field setup at Octagon

The chamber this new setup was built for (called 'Octagon' due to its octagon shape) is slightly bigger and different mounting options are available, therefore different changes were made for the design. The most important lengths of the chamber are depicted in Figure 3. Based on these lengths, a fixer for the magnets and side coils was designed as depicted in Figure 4. Since there were already similar prototypes, and to ensure maximum movement capability of the magnet on this fixer, the design choice was made to put the coils at the inner part of the fixer, enlarging the minimum inner distance between the permanent ring magnets even further, namely 14 mm per side, 28 mm in total. The material of choice for these fixers is aluminium due to its shapeability and weak paramagnetic properties. The turnable magnet holder displayed in Figure 5 itself is made of brass, which has weak diamagnetic properties. It has a movement range of about 12 mm on the magnet-and-coil-fixer.

The assembly with the coils and magnets, fixed to the vacuum chamber, can be seen in Figure 6.

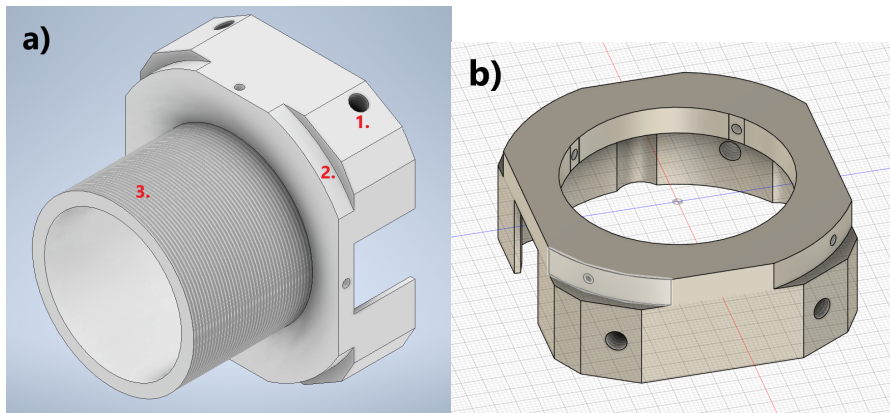


Figure 4: a) The magnet-and-coil-fixer. 1.) The screw holes allow to mount the fixer onto the side of the lateral windows with M6 screws. 2.) The interrupted round areas are matching the diameter of the coil holder, allowing to slide the coil onto it. The small M3 screw holes have inner threads and allow a firm fixing of the coil. 3.) A custom made M53x1 thread allows the magnet fixer (see [Figure 5](#)) with a matching counterpart to be displaceable along the axis of the thread. b) Coil fixer. Basically the same design as to the left without the need of the thread to hold the magnet, but only the coil.

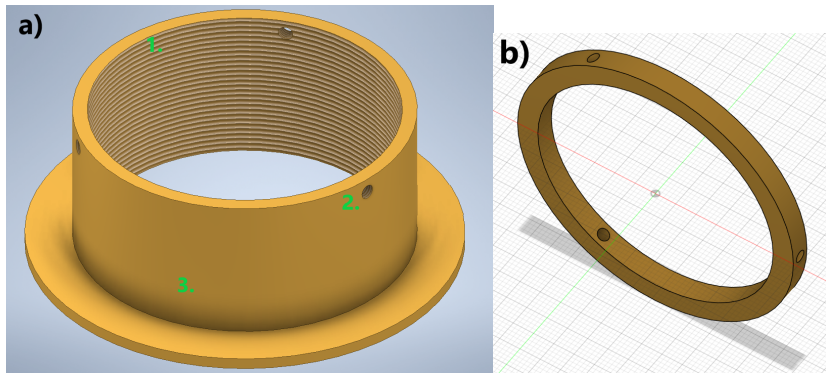


Figure 5: a) The magnet holder. 1.) The inner M53x1 thread allowing it be screwed onto the magnet-and-coil-fixer. 2.) Small M3 screw holes to fix the brass ring in b) to contain the magnet ring in between. The use of plastic screws is recommended, since the tip will otherwise destroy the M53x1 thread it is mounting the holder onto. 3.) The radial area the ring magnet is placed on. b) The brass ring to contain the ring magnet to the sides.

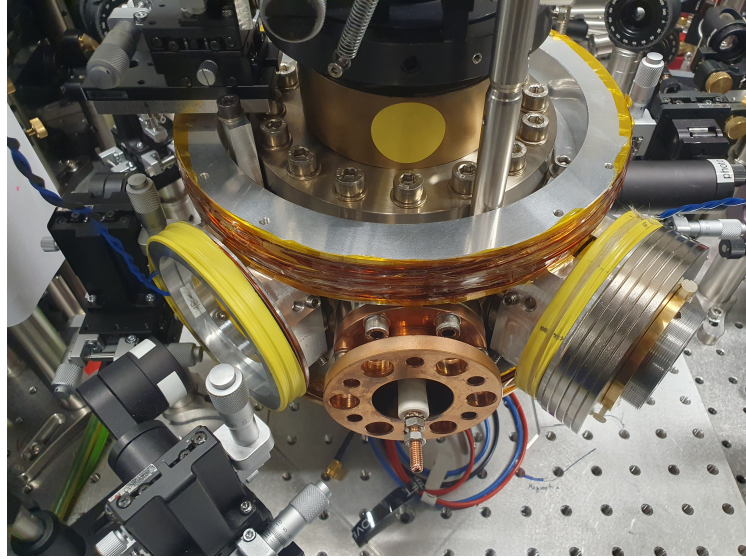


Figure 6: The magnet-and-coil-fixer mounted to the vacuum chamber. The coils (yellow) are on the inner side towards the chamber, while the magnet (on the right fixer) can be moved to the outside, allowing to alter the  $B$ -fields in the center of the chamber. Their respective counterparts are behind the chamber and therefore not seen in this picture.

The last part of the magnetic field setup to be discussed are the top and bottom coil. The top coil is already usable and pre-wound. The bottom coil however is not directly applicable to the setup, since three columns holding the Octagon vacuum chamber prevent a direct mounting to the bottom side. Therefore the bottom coil holder was made from two halves of the top coil holder design, allowing them to be placed individually beneath the chamber and then mount them together. Therefore the winding of the coil is only possible *in situ* beneath the chamber. To make this not removable coil resistant to future bakings of the chamber (degas procedure at temperatures above 100 °C) a copper wire with THEIC isolation layer from the company Jiricek (IEC 60317-13) was used, capable of temperatures up to 210 °C. This wire is by a factor of  $\approx 2$  thicker than the wire of the pre-wound top coil. The resulting different geometries despite same winding number ( $N = 100$ ) showed a shift of the magnetic field minimum from the center of roughly 10 mm (see appendix [Figure 53](#)), therefore the top coil was rewound with the same heat resistant wire. As can be seen in [Figure 7](#), after the rewinding the thick wire of top and bottom coil "outgrows" their coil holders, which was not a problem before. This lead to the additional necessity to add a small ring of 5 mm thickness between the magnet-and-coil-fixer and the side windows to ensure proper mounting on the chamber, again increasing the minimal distance between the permanent magnets by 10 mm.



Figure 7: The side of the top coil at the setup. 1.) shows the coil overgrowth of the vertical coil pair. 2.) To ensure proper mounting of the side coils and magnets, an additional ring (yellow) between the lateral window of the chamber and the magnet-and-coil-fixer is established

### 2.5.1 The magnetic field of ring magnets and coils

The ring magnets used for the Octagon are from the same company and are of the same dimensions and remanence  $B_r = 1.17 \text{ T}$  used in [Hakelberg et al., 2018], despite they are modular in magnet thickness  $D$ , since they consist of multiple layers of (4 mm tick). In the paper, the thickness of the magnets is 12 mm, while the recorded inner distance between the magnets' surfaces is  $d = 223 \text{ mm}$ .

The analytical expression for the magnetic field of one ring magnet along its symmetry axis is [Hakelberg et al., 2018]

$$B_{\text{ring}}(x) = \frac{B_{\text{textr}}}{2} \left[ \left( \frac{x}{\sqrt{R_{\text{texto}}^2 + x^2}} - \frac{x - D}{\sqrt{R_{\text{texto}}^2 + (x - D)^2}} \right) - \left( \frac{x}{\sqrt{R_{\text{texti}}^2 + x^2}} - \frac{x - D}{\sqrt{R_{\text{texti}}^2 + (x - D)^2}} \right) \right], \quad (2.4)$$

where  $R_{\text{texto}}$  and  $R_{\text{texti}}$  are the outer and inner radii of the ring, respectively. With the given distance  $d$  and  $B_{\text{textr}}$  of the paper, a magnetic field of  $\approx 109.64 \text{ G}$  is reached. For the Octagon, the minimal given distance between the inner surfaces of the magnet ring accumulates to

$$\begin{aligned} d_{\min} &= d_{\text{chamber}} + 2 \cdot d_{\text{windows}} + 2 \cdot d_{\text{coils}} + 2 \cdot d_{\text{overgrowth rings}} \\ &= (176.8 + 40 + 28 + 10) \text{ mm} = 254.8 \text{ mm}, \end{aligned} \quad (2.5)$$

which is more than 30 mm more than the given value in the paper. Therefore, a stronger magnet with increased thickness is needed. Measurements in section 3

show, that for that distance at least two 5 layers of ring magnets ( $D = 20$  mm) are needed.

The central field of a coil pair with coil radius  $R$  and distance  $d$  without matching the Helmholtz condition ( $d \neq R$ ) can be described by (adapted from [Demtröder, 2013])

$$B_{coils}(x = 0) = -\mu_0 R^2 N \cdot I \cdot \left( \frac{1}{\sqrt{\left(\frac{d}{2}\right)^2 + R^2}} \right), \quad (2.6)$$

where  $\mu_0$  is the vacuum magnetic permeability constant,  $N$  the number of coil windings and  $I$  the shared driving current of the coils

### 2.5.2 The test setup

To perform the measurements outside the chamber, a chamber dummy was 3D printed with the distance dimensions of the Octagon in one direction, with the additional imitation of the lateral windows to mount the magnet-and-coil-fixer on it, seen in Figure 8. The Hall sensor used in this setup is a HE244 from AST and was characterized in Lucas Eisenhart's bachelor thesis and has a sensitivity of [Eisenhart, 2022]

$$S_{Hall} = (0.0393 \pm 0.0007) \text{ mV/G} \quad (2.7)$$

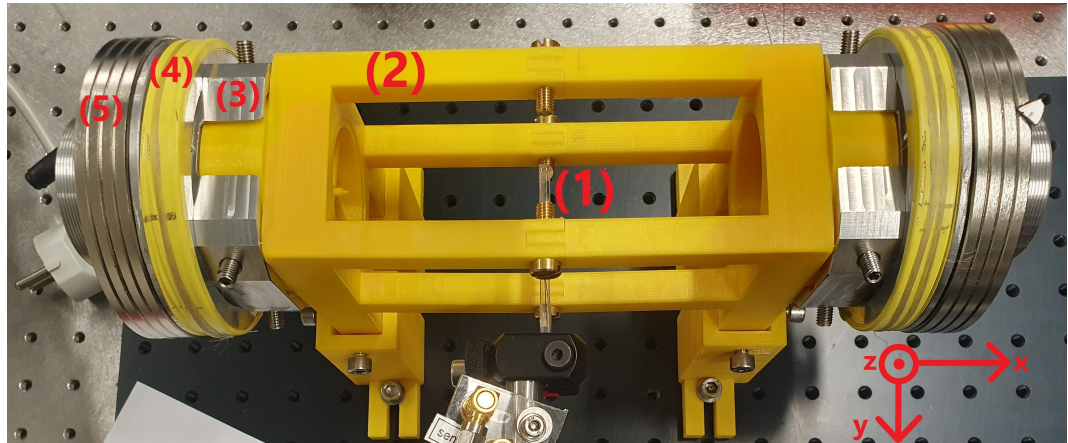


Figure 8: The test setup for the coils and magnets: The Hall sensor (1) in the center of the chamber dummy (2), which has the same length dimensions as the vacuum chamber. At the sides the magnet-and-coil-fixer (3) is mounted to the dummy, itself holding the coil (4) and the ring magnet (5). The choice of the coordinate system defines the x-axis as the quantization axis for this experiment.

## 2.6 Properties of the $^{25}\text{Mg}^+$ ion

The hyperfine energy level splitting of the  $^{25}\text{Mg}^+$  ground state  $^2S_{1/2}$  splits with  $J=1/2$  and  $I=5/2$  into the  $F=2, 3$  levels with their respective  $m_F = -F, -F+1, \dots, F$  sub-levels. As a qubit for quantum simulation or quantum sensing in principle any of the transitions  $|F=2, m_F\rangle \leftrightarrow |F=3, m_F\rangle$  could be picked. While for quantum simulation a mostly insensitive transition would usually be preferred, for quantum sensing it is usually the most sensitive. For magnetic fields the (in-)sensitivity for different strengths can be best estimated via the Breit-Rabi-formula, which describes the energy level development up to the intermittent region, before the Paschen-Back-effect for strong magnetic fields is dominating. It can be expressed as [Meschede, 2015]

$$\omega_{F=I\pm\frac{1}{2},m_F} = -\frac{A}{4} + g_I m_F \mu_N B \pm \sqrt{1 + \left( \frac{8m_F(g_J\mu_B - g_I\mu_N)}{(2I+1)^2 A} \cdot B \right) + \left( 2 \frac{g_J\mu_B - g_I\mu_N}{(2I+1)A} \cdot B \right)^2}, \quad (2.8)$$

where  $A$  is the ground-state hyperfine constant for  $^{25}\text{Mg}^+$ ,  $\mu_B$  Bohrs and  $\mu_N$  the nuclear magneton,  $g_J$  and  $g_I$  the Landé factors of the total angular momentum and the nuclear spin, respectively. The energy level development for all sub-levels up to 200 G is presented in Figure 9. The energy level development is dominated by linear terms, but impacted by slight nonlinearities. For certain energy level transitions at certain magnetic field strengths, these nonlinearities can induce a (local) minimum of the transition. For the  $^{25}\text{Mg}^+$  ground state  $S_{1/2}$  manifold this appears for the  $|3, 1\rangle \leftrightarrow |2, 0\rangle$  transition at  $B = 109.64$  G, as seen in Figure 10. This is a so called clock transition and the reason, the magnetic field of section 3 is tuned to this strength. For the sensing measurements of this thesis, the most sensitive transition at this magnetic field, the  $|3, 3\rangle \leftrightarrow |2, 2\rangle$  is chosen. A table of properties of the selected transitions were estimated by [Hakelberg et al., 2018] and can be found in Table 1.

Label	Transition	Trans. frequency	Field sensitivity	Cpl. Str.	Coherence
		$\omega$ (2π MHz)	$\partial\omega/\partial B$ (2π MHz mT <sup>-1</sup> )	$\Omega_{\text{Coup}}$ (2π kHz)	time $\tau$ (ms)
MW <sub>0</sub>	$ 3, 3\rangle \leftrightarrow  2, 2\rangle$	1541.066(4)		-21.764	161(3) 0.42(6)
MW <sub>1</sub>	$ 2, 2\rangle \leftrightarrow  3, 1\rangle$	1655.815(2)		-10.116	38.3(8) 0.9(1)
MW <sub>2</sub>	$ 3, 1\rangle \leftrightarrow  2, 0\rangle$	1762.973 811 60(1)	$\pm 0(1) \times 10^{-4} (+0.434 \text{ mT}^{-1})$	28.5(6)	6600(900)
RF <sub>0</sub>	$ 2, 2\rangle \leftrightarrow  2, 1\rangle$	55.260(1)		+5.381	0.28(6) 1.8(2)

Table 1: Transition properties at  $B = 109.64$  G from [Hakelberg et al., 2018]. Comparing the values, the absolute sensitivity values of the transitions correlate negatively with the coherence time and the number of estimable decimal places of the transition frequency, as explained in subsubsection 2.6.1.

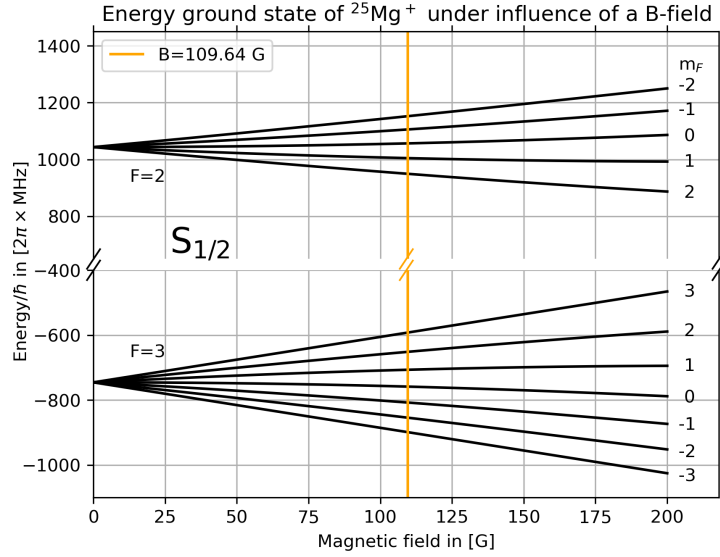


Figure 9: Breit-Rabi formula for the ground state manifold of  $^{25}\text{Mg}^+$ . The energy level development is dominated by linear terms, but impacted by slight nonlinearities. For certain energy level transitions at certain magnetic field strengths, these nonlinearities can induce a (local) constant slope of the transition frequency plotted against the B-field. For the  $S_{1/2}$  ground state manifold of  $^{25}\text{Mg}^+$  this appears for the  $|3, 1\rangle \leftrightarrow |2, 0\rangle$  transition at  $B = 109.64 \text{ G}$

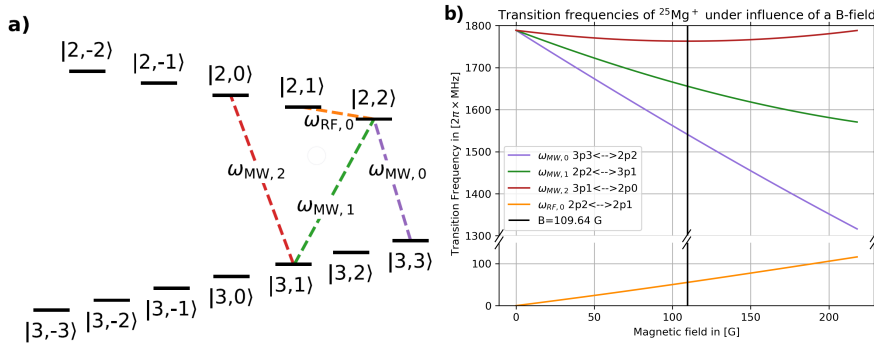


Figure 10: a) choice of transition frequencies, adapted from [Hakelberg et al., 2018] and their visualisation in b) as the difference of the Breit-Rabi formulas of the respective energy levels, yielding the transition frequency development. Most interesting is the minimum of the  $|3, 1\rangle \leftrightarrow |2, 0\rangle$  transition at  $B = 109.64 \text{ G}$  (dark red) indicating a clock transition, while the  $|3, 3\rangle \leftrightarrow |2, 2\rangle$  transition (purple) shows the highest sensitivity ( $\equiv$  local slope of the transition) and is therefore chosen as the sensing qubit in this thesis.

### 2.6.1 The Ramsey sequence

The Ramsey sequence first presented in [Ramsey, 1950] is a reliable way to investigate qubits. It can be used to estimate the coherence time and the frequency of the qubits transition without continuous exposure of external light or electric fields, minimising AC-Stark shifts as described by [Delone & Krainov, 1999]. The sequence is shown in [Figure 11](#) and starts with an preparation pulse to initialize the qubit in its ground state  $|0\rangle$  of the computational basis. After that, a  $\pi/2$ -pulse of a driving field near resonance is applied bringing the qubit into the superposition state  $1/\sqrt{2}(|0\rangle + |1\rangle)$ . On the Bloch sphere, this pulse rotates the state vector anticlockwise around the x-axis, hence defining the x-axis. With the computational basis states defining the z-axis and the position of the state vector after the  $\pi/2$ -pulse defining the y-axis, the coordinate system is set. After that the system evolves freely for the dedicated time  $t_{\text{Ramsey}}$ . Being exposed to an external  $B$ -field, the qubit state picks up a phase  $\varphi$  (relative to the y-axis) correlated to the Lamour precession frequency difference  $\Delta\omega = \omega_0 - \omega$  of the qubit transition frequency  $\omega_0$  and the driving field frequency  $\omega$ , yielding  $1/\sqrt{2}(|0\rangle + e^{i\varphi}|1\rangle)$  with  $\varphi = \Delta\omega t_{\text{Ramsey}}$ . For  $\Delta\omega > 0$  the state vector rotates anticlockwise on the xy-plane, clockwise for  $\Delta\omega < 0$ . After that another  $\pi/2$ -pulse with the relative phase  $\varphi'$  compared to the first pulse is applied. This means, that now the rotation direction driving the state vector is shifted by  $\varphi'$  on the xy-plane in comparison to the x-direction-defining first  $\pi/2$ -pulse. Three easy scenarios can be imagined:

1.  $\varphi' = \varphi \pm \pi/2$  due to their definition regarding perpendicular axes (x- and y-axis), in these phase configurations, the second  $\pi/2$  pulse rotational axis and the state vector are parallel or anti-parallel on the Bloch sphere. The state vector is therefore not affected by the rotation and stays until the detection in the equal superposition state.
2.  $\varphi' = \varphi$  with anticlockwise rotation of the  $\pi/2$ -pulse, the state vector is driven into the computational basis state  $|1\rangle$
3.  $\varphi' = \varphi \pm \pi$  with anticlockwise rotation of the  $\pi/2$ -pulse, the state vector is driven back into the computational basis state  $|0\rangle$

For all other cases, the state will end up in a superposition state like

$$\begin{aligned} |\Phi\rangle &= c_{|0\rangle} |0\rangle + c_{|1\rangle} e^{i\Theta} |1\rangle, \quad \text{where} \\ c_{|0\rangle}^2 &= \frac{1}{2} (1 - \cos(\varphi' - \varphi)) = \frac{1}{2} (1 - \cos(\varphi' - \Delta\omega t_{\text{Ramsey}})) \\ c_{|1\rangle}^2 &= 1 - c_{|0\rangle}^2 \end{aligned} \quad (2.9)$$

and  $\Theta$  is defining a global phase, which depends on relative conditions of the angles like  $\varphi' \gtrless \varphi$  or  $\varphi', \varphi \gtrless \pi/2$  (not further investigated).

This phase is of no further importance, since the following detection step projects

the state into the computational basis  $\{|0\rangle, |1\rangle\}$  independent of the global phase.

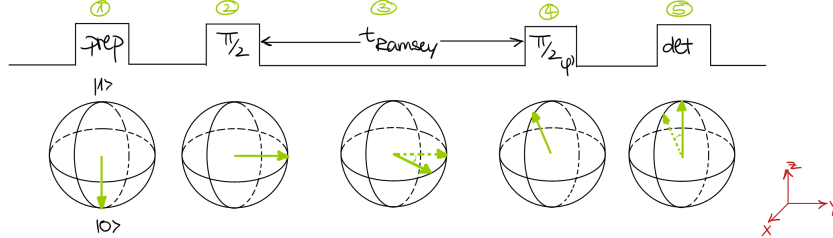


Figure 11: The Ramsey sequence. The top line shows the pulse sequence. Despite the labeled  $t_{\text{Ramsey}}$  time, no particular waiting times are used between the single pulses. Below that the effect of each action is depicted in the Bloch sphere. The first  $\pi/2$ -pulse defines the coordinate system (red). 1) Initialization of the qubit. This usually implies cooling of the system and preparation of the ground state  $|0\rangle$ . 2) The first  $\pi/2$ -pulse creates an equal superposition state  $1/\sqrt{2}(|0\rangle + e^{i\varphi}|1\rangle)$ . 3) During the free evolution of the qubit system for  $t_{\text{Ramsey}}$  duration, the  $|1\rangle$  state picks up a phase  $\varphi = (\omega_0 - \omega) \times t_{\text{Ramsey}}$  relative to the y-axis of the system in the xy-plane, depending on the Lamour frequency difference between the qubits transition frequency  $\omega_0$  and the frequency  $\omega$  of the external driving field. Positive values rotate counterclockwise on the Bloch sphere, indicating red detuned driving frequencies. In the depicted example, a clockwise rotation indicates a blue detuning. 4) The second  $\pi/2$ -pulse with a relative phase  $\varphi'$  to the first pulse (and therefore relative to the x-axis on the xy-plane) rotates the state vector around its axis. In the depicted example  $\varphi' = 0$ , so a second pulse around the x-axis is shown. 5) The detection step projects the final state into the computational basis. Repeating the sequence to get enough statistics gives rise to the probability amplitudes of the computational basis.

### 2.6.2 The frequency scan

A frequency scan is performed to find the resonance in the scanned region. This involves the sequence depicted in Figure 12. After the preparation pulse  $|\Phi\rangle = |0\rangle$ , a  $\pi$ -pulse is performed. If the frequency is on resonance, this pulse induced a population inversion of the state and would therefore be projected into the other basis ( $|1\rangle$ ). In the off-resonant case this transition is not driven and the state is projected into  $|0\rangle$ . For the same frequency, this sequence is repeated to gather enough statistics (few hundred times)

## 2.7 The Bermuda experiment

As the magnetic field configuration of the Bermuda experiment is already described in subsubsection 2.4.2, this part will focus on the laser systems and microwave used to perform the sequences used above. This subsection highly revolves around the

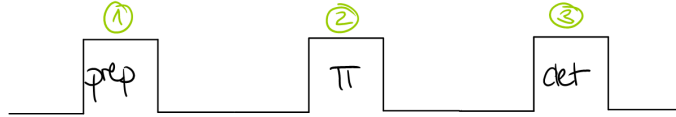


Figure 12: Frequency scan sequence. (1) After the preparation pulse ( $|\Phi\rangle = |0\rangle$ ) , a  $\pi$ -pulse is performed (2). If the frequency is on resonance, this pulse induced a population inversion of the state and would therefore be projected into the other basis ( $|1\rangle$ ) by the detection pulse (3). In the off-resonant case this transition is not driven and the state is projected into  $|0\rangle$

thesis of [Wittemer, 2019]. To understand the laser systems and microwave frequency tuning, the energy level of the  $^{25}\text{Mg}^+$  is displayed in Figure 13.

### 1. $\pi/2-$ , $\pi-$ pulses

The dedicated qubit transition is the orange marked  $S_{1/2}|3,3\rangle \leftrightarrow S_{1/2}|2,2\rangle$  transition. To drive this transition, a microwave with  $\omega \approx 1541.07 2\pi \times \text{MHz}$  is applied. To achieve special pulses like  $\pi/2-$  or  $\pi-$ pulses, the microwave power times the driving time have to be picked to induce the balanced superposition state or the state inversion, respectively.

### 2. Cooling and detection

For Doppler cooling, the Blue Doppler (BD) laser ( $\sigma^+$  for  $\Delta m_F = +1$  transitions) is employed, which couples the qubit ground state  $S_{1/2}|3,3\rangle$  to the  $P_{3/2}|4,4\rangle$  level. To address different stages of cooling, the laser is splitted into sublasers (BD, BDD BDx) of different red detunings from the transition. This cools the ion by coupling the motional to the electronic degree of freedom, where the motional energy will be released as fluorescence light. A barely red detuned BDx laser can achieve final cooling but is mainly used for detection purposes. For state detection the fluorescence light emitted from the  $P_{3/2}|4,4\rangle$  is gathered. If fluorescence is detected after the BDx pulse, the state was in the ground state, since the BDx is tuned to this transition, no fluorescence indicates the qubit is in the excited state.

### 3. Repump

As part of the preparation, the Red Doppler (RD) laser (also  $\sigma^+$ ) is employed to increase the internal state preparation in the ground state. This laser basically pumps population from the ions ground state (which are not part of the qubit) to the  $P_{1/2}$  state, from where it decays naturally to the qubit's ground state  $S_{1/2}|3,3\rangle$ , increasing its preparation fidelity. To address all sub-levels correctly, the laser is splitted into different sublasers of different detunings.

These are the driving fields for the pulse sequences described above. The whole experiment is controlled and executed by the ARTIQ software <https://m-labs.hk/>

[experiment-control/artiq/](#). Describing this software would exceed the purpose of this thesis, but it is mentioned at some points in the thesis and shold therefore be introduced here.

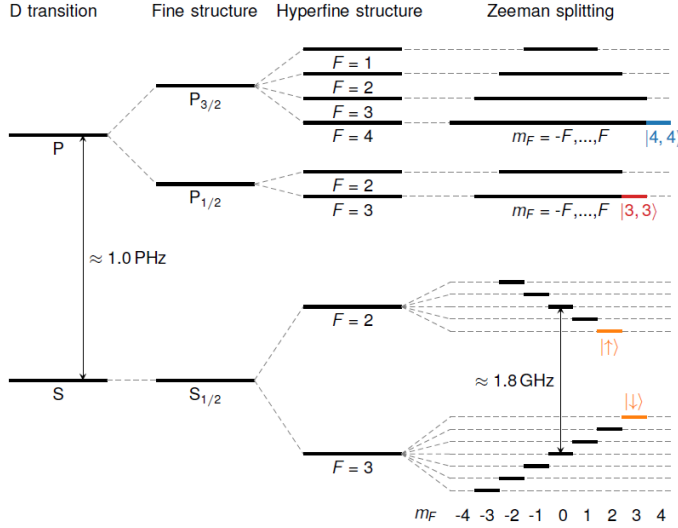


Figure 13: Energy level hyperfine structure and laser transitions of the  $^{25}\text{Mg}^+$  ion from [Wittemer, 2019]. The orange marked states represent the qubit, driven by a microwave frequency. To the red state the repump lasers (RD with all it's sub lasers of different detuning) are tuned. The blue state is addressed by the cool and detection lasers (BD with all it's sublasers of different detuning).

### 2.7.1 The uncertainties in trapped ion experiments

In [Itano et al., 1993] four different noises are addressed due to interactions of the laser and microwave systems with the ion. These are

$$\sigma_{\text{calc}}^2 = \sigma_{\text{proj}}^2 + \sigma_{\text{pump}}^2 + \sigma_{\text{shot}}^2 + \sigma_{\text{tech}}^2. \quad (2.10)$$

#### 1. Quantum projection noise $\sigma_{\text{proj}}^2$

Arises from the projection of the state into the computational basis in the detection pulse. It is large for superposition states of comparable population amplitudes and zero for the state being already in the computational basis.

#### 2. Pump noise $\sigma_{\text{pump}}^2$

This comes from ions failed to pump due to fluctuations in amplitude or frequency of the RD, which still contribute to the signal. It is maximal at the lowest counts and minimal at the highest counts (where basically the ion is successfully pumped).

#### 3. Shot noise $\sigma_{\text{shot}}^2$

Results simply from the Poisson statistics in photon detection and scales with  $\sqrt{\text{counts}}$ .

#### 4. Technical noise $\sigma_{\text{tech}}^2$

Basically all to this point not appointed forms of noise from the environment, e.g. stray fields, temperature influences etc.

## 2.8 Properties of the NV-centers in diamond

The diamond is in the widest common sense known as a valuable crystal. From a more scientific point of view, diamond is one of the hardest known materials due to its crystal lattice following the tetrahedral  $C_{3v}$  symmetry. Neither the value nor the hardness make diamond interesting for quantum sensing, the interesting part lies in the color defects in diamond. These are impurities in the crystal lattice, where some carbon atoms are replaced by atoms of other species or vacancies. Of particular interest and subject to many studies (as gathered in [Doherty et al., 2013]) is the NV-center (Nitrogen Vacancy center), where two neighboring carbon atoms are replaced by a nitrogen atom and a vacancy. Assuming mono-crystalline diamonds, 4 possible directions of the NV-center axis are possible, as shown in Figure 14.

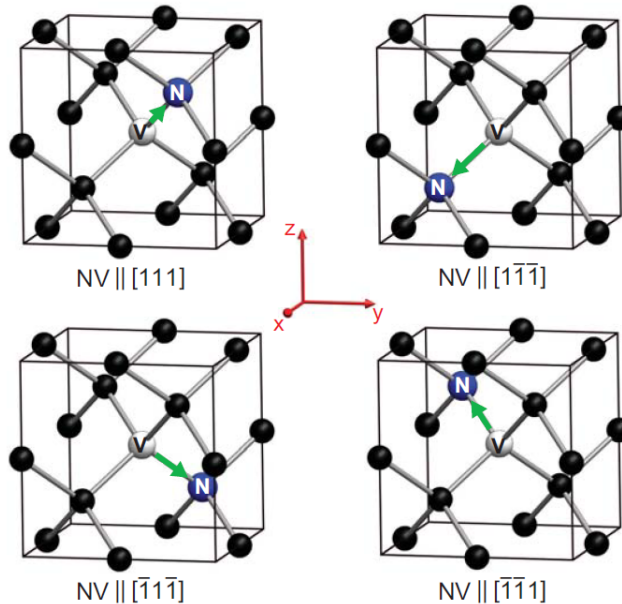


Figure 14: The diamond lattice structure with 4 possible NV-center orientations regarding the crystal lattice [Pham, 2013]. A NV-center is created when two neighbouring C-atoms are replaced by a nitrogen atom and a vacancy. The crystal lattice for diamond follows the tetrahedral  $C_{3v}$  symmetry, therefore 4 orientations of the NV-centers in diamond are possible. These are described by the Miller indices.

### 2.8.1 Energy level structure

The energy levels of NV-centers are based on spin properties of the electrons present in the center. With a neighboring nitrogen atom instead of one carbon atom, around the vacancy there are 5 electrons (instead of 4 from 4 surrounding carbon atoms) present. Four of these electrons are dangling bonds (with no center carbon to bind with, these stay close to their nuclei), only one of the electrons from the nitrogen is rather free and present in the vacancy. The vacancy also forms a potential well capable of attracting an additional electron from the surrounding lattice. With this additional electron, the NV-center is of negative charge and therefore named  $\text{NV}^-$  center. With two free electrons, this system builds a spin 1 system and is the most important kind of NV-center due to its magneto-optically active properties [Schirhagl et al., 2014], which the  $\text{NV}^0$ - (only free electron from nitrogen, spin 1/2 system) and  $\text{NV}^+$ - (only dangling bound electrons, spin 0) centers don't possess. Without these properties, there is no detectable magnetic resonance [Doherty et al., 2013], and regarding the above defined criteria for quantum sensors, the interaction part (4.) is not fulfilled. Therefore, for this thesis only the  $\text{NV}^-$  centers are of importance and further introduced.

The  $\text{NV}^-$ -center possesses an energy level structure which makes it interesting to quantum sensing. The clue about these energy levels is that they are lying between valence and conduction band of the pure diamond and are therefore well addressable. The resulting, distinct energy level diagram is shown in [Figure 15](#). Once the degeneracy of the  $m_s = \pm 1$  states of the ground state  ${}^3A_2$  is lifted by an applied magnetic field, a ground state qubit between e.g. the  $m_s = 0$  and the  $m_s = -1$  state can be employed, enabling criterion 1.) for the quantum sensor A further feature is the low-key effort to use  $\text{NV}^-$ -center, especially since their discrete energy levels are accessible at room temperature, and are themselves protected and sheltered inside the diamond lattice. Therefore, important optical properties arise like no evidence of photobleaching (irreversible destruction of the NV-center due to high energy (de-)excitation) could be found, which enables the use of high power lasers. Moreover, the  $\text{NV}^-$ -center possesses photo-stability under typical off-resonant excitation, large optical absorption cross-sections paired with high quantum yields and short excited state lifetimes together with no efficient shelving in dark states [Doherty et al., 2013], making it highly fluorescent and therefore enables good readout properties as demanded by the 2.) criterion of quantum sensors. Last to fulfill is the 3.) criterion, stating the coherent manipulation of the chosen qubit. With the zero field splitting (ZFS) of the ground state being  $D = 2.87\text{ GHz}$ , a microwave can be applied to coherently manipulate the qubit. Depending on the  $B$ -field used in this thesis, the Zeeman splitting introduces changes of this value around 1-3 orders of magnitudes lower than  $D$ .

To identify the  $\text{NV}^-$ -center correctly and distinct it from other color defects, the easiest way to do this is to look at the fluorescence spectrum of the diamond. The typical spectrum is the broad vibrational band of the lattice around  $600 - 830\text{ nm}$ , with a small side peak around  $\sim 637\text{ nm}$ , identifying the ZPL as seen in [Figure 16](#).

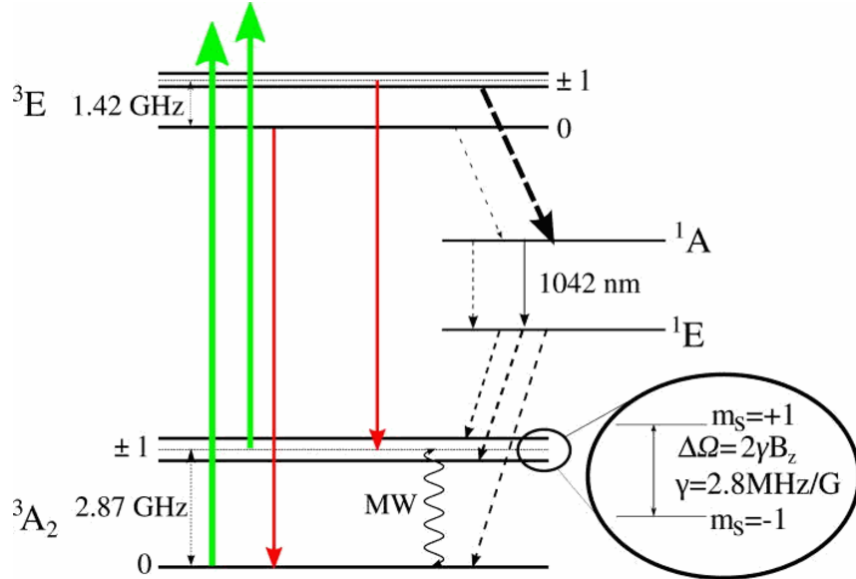


Figure 15: Display of the energy level structure of the NV-center in diamond by [Jarmola et al., 2015]. It is located between the valence and conduction band of the diamond lattice (not shown) allowing direct addressability of the discrete levels. The green arrows indicate the far off-resonant excitation of the ground state  $^3A_2$ , while the red arrows describe the spontaneous emission from the excited state  $^3E$  to the ground state, known as ZPL (Zero phonon line  $\equiv$  pure optical transition in a lattice with presence of non-radiative phonon deexcitation). The dotted black arrows indicate the non radiative decay paths of the excited state, where the thickness of the arrows indicate their relative strength. This strength difference enables the ODMR-technique described in subsubsection 2.8.3. Both ground and excited state have an energy difference between  $m_s=0$  and  $m_s=\pm 1$  of  $D_{\text{gs}} = 2.87 \text{ GHz}$  and  $D_{\text{es}} = 1.42 \text{ GHz}$ , respectively. The spin states  $m_s = \pm 1$  of the ground state experience the Zeeman splitting  $\Delta\Omega$  which is the key towards measuring  $B$ -fields with NV-centers in Diamond.

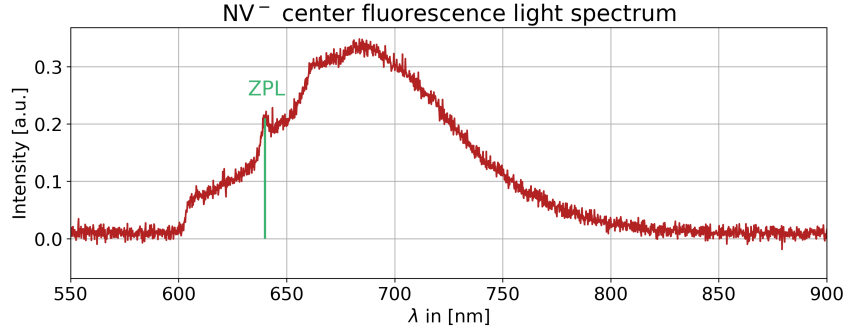


Figure 16: Fluorescence spectrum of the NV-centers in diamond in the visible and near infrared regime. This spectrum was taken at room temperature, where the vibrational modes of the diamond lattice dominate. The cut-off at  $\lambda \approx 600$  nm comes from an optical high pass filter blocking the excitation laser light, which's intensity is several orders of magnitude stronger than the observed fluorescence. At  $\lambda \approx 637$  nm the small side peak can be identified as the ZPL of the NV<sup>-</sup> centers.

Although this spectrum is recorded as part of this thesis, it will serve merely as a proof-of-principle plot and is not further investigated.

### 2.8.2 The spin 1 Hamiltonian of the NV-center ground state

Usually, one wants to employ a two-level energy system, but to understand the spin dynamics of the NV<sup>-</sup>-center a look at the spin 1 Hamiltonian is necessary. For simplicity, the nuclear spin interactions, to name Zeeman-nuclear spin, hyperfine spin-nuclear spin and dipol-dipol nuclear spin interaction focussing on the external influence of magnetic fields

$$H_{\text{gs}} = \underbrace{\frac{1}{\hbar^2} D_{\text{gs}} \left( S_z^2 - \frac{1}{3} S(S+1) \right)}_{H_{\text{ZFS}}} + \underbrace{\frac{1}{\hbar} \mu_B g \vec{S} \cdot \vec{B}}_{H_{\text{Zeeman}}} + H_{\text{E, strain}} \quad (2.11)$$

The ZFS (zero field splitting) term is the dominating term with the already introduced strength  $D_{\text{gs}} = 2.87$  GHz, while  $\mu_B$  is Bohr's magneton and  $g \sim 2.0028$  the approximately isotropic electron g-factor in NV<sup>-</sup>-centers. Since there exist many different approaches on defining the electric and strain field interaction [Segawa & Igarashi, 2023] [Doherty et al., 2012] [Schirhagl et al., 2014], and this thesis focuses on the magnetic field part, these other external influences are neglected. The z-direction is defined along the axis of the NV-center

The spin operators with S=1 in matrix representation are

$$S_x = \frac{\hbar}{\sqrt{2}} \begin{pmatrix} 0 & 1 & 0 \\ 1 & 0 & 1 \\ 0 & 1 & 0 \end{pmatrix} \quad S_y = \frac{\hbar}{\sqrt{2}} \begin{pmatrix} 0 & -i & 0 \\ i & 0 & -i \\ 0 & i & 0 \end{pmatrix} \quad S_z = \hbar \begin{pmatrix} 1 & 0 & 0 \\ 0 & 0 & 0 \\ 0 & 0 & -1 \end{pmatrix}$$

This, with  $B_z = B_{\parallel}$  and  $B_{\perp}$  as a combination of  $B_x$  and  $B_y$  yields the matrix representation of the Hamiltonian [Segawa & Igarashi, 2023][Doherty et al., 2012]

$$H_{\text{gs}} = \begin{pmatrix} \frac{D_{\text{gs}}}{3} + \mu_B g B_{\parallel} & \frac{1}{\sqrt{2}} \mu_B g B_{\perp} & 0 \\ \frac{1}{\sqrt{2}} \mu_B g B_{\perp} & -\frac{2D_{\text{gs}}}{3} & \frac{1}{\sqrt{2}} \mu_B g B_{\perp} \\ 0 & \frac{1}{\sqrt{2}} \mu_B g B_{\perp} & \frac{D_{\text{gs}}}{3} - \mu_B g B_{\parallel} \end{pmatrix} \quad (2.12)$$

with the eigenvectors  $|m_s\rangle$  like

$$|1\rangle = \begin{pmatrix} 1 \\ 0 \\ 0 \end{pmatrix} \quad |0\rangle = \begin{pmatrix} 0 \\ 1 \\ 0 \end{pmatrix} \quad |-1\rangle = \begin{pmatrix} 0 \\ 0 \\ 1 \end{pmatrix} \quad (2.13)$$

### 2.8.3 The ODMR technique

The optically detected magnetic resonance (ODMR) technique utilises different decay channel strengths from different energy levels to find the resonance frequency of the  $|0\rangle$  to the  $|\pm 1\rangle$  state vector, performing a frequency scan over the spectrum of interest (around  $D_{\text{gs}}$ ). With [Figure 15](#) in mind this is one full decay cycle, starting at  $|0\rangle$ :

1. While sweeping the spectrum, around the resonance of the triplet ground state ( ${}^3A_2$ ) splitting the microwave populates  $|\pm 1\rangle$  from  $|0\rangle$ . Since the microwave drives continuously, all three states are populated.
2. The  ${}^3A_2$  population is off-resonantly excited by a green laser (blue detuned from ZPL) into higher energy levels of the NV-center
3. Due to spin conserving selection rules the spin state relaxes into the respective  $|0\rangle_e, |\pm 1\rangle_e$  states of the excited triplet state  ${}^3E$ .
4. The  $|\pm 1\rangle_e$  levels have a strong non-radiative decay channel over the two intermediate singlett states ( ${}^1A$  and  ${}^1E$ ) back to the triplet ground state  ${}^3A_2$ , while the  $|0\rangle_e$  mainly decays optically via the ZPL.
5. Due to this strong lattice decay channel, the overall optical spontaneous emission (ZPL) channel, measured by the fluorescence signal of the setup, is weaker and therefore seen as a resonance dip of Lorentzian shape when scanning the full spectrum.

Without external magnetic field, all possible splittings are degenerate and are observed as one, high contrast (10-13%) dip (as seen in [Figure 17](#)), while lifting the degeneracy by applying an external magnetic field. Up to eight, low contrast dips can be observed in the spectrum. These dips belong pairwise as the  $|0\rangle \rightarrow |\pm 1\rangle$  transitions to the 4 possible orientations of the NV-center. With the relative splittings of the four orientations the strength of the external magnetic field can be recalculated as shown in [section 5](#).

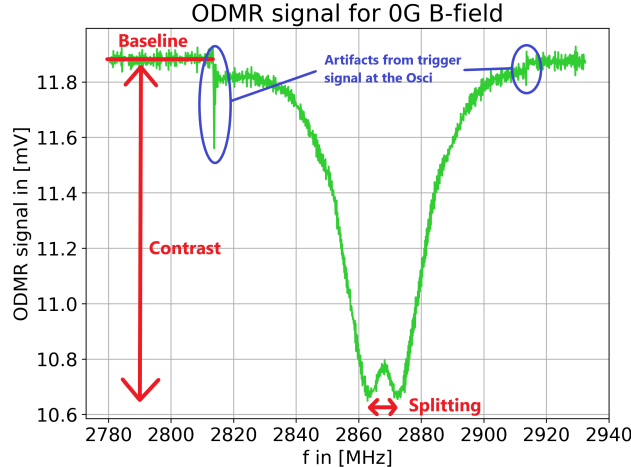


Figure 17: The ODMR signal without applied  $B$ -field. The degeneracy of the  $|\pm 1\rangle$  states is already lifted mainly due to strain influences [Doherty et al., 2013] not described in the above Hamiltonian. In red are some technical terms defined, which are used in the results part. The blue circled artifacts originate from the trigger signal at the oscilloscope.

## 2.9 The diamond experiment setup

To achieve the ODMR-signal and have the ability to apply variable magnetic fields to the diamond, the setup depicted in Figure 19a is employed. The diamonds used have roughly the size of  $20\text{--}30\,\mu\text{m}$  which makes them stick dust-like on the vertical surface of the microwaveguide. Since these diamonds are neither specially fabricated for high NV-center concentration nor have any dedicated cut, it is part of the experiment to find a fitting diamond with high NV-center concentration (high fluorescence) out of the ensemble poured onto the waveguide. To detect their fluorescence, an off-resonant laser of  $519\,\text{nm}$  is used to excite the NV-centers. With the aspherical lens of  $10\,\text{mm}$  focal length in front of the diamond it is possible to focus the laser into beam-waists of the size of the Diamonds, allowing to illuminate a single diamond or even sub-parts of it. Without this possibility, only blurred ODMR-spectra can be recorded as seen in Figure 52. Further, the laser beam, guided by two mirrors from the fiber output to the aspherical lens, is aligned in the main axis of the largest coil, to be defined as the z-axis of the experiments coordinate system. To find a matching diamond, the surface of the waveguide can be scanned by the laser employing a xyz-translation stage the waveguide is attached to. This way the laser stays on the z-axis of the system and the waveguide is moved relatively to the fixed beam position. The light from the laser beam is reflected and the fluorescence light emitted to reach the detection elements. First, an optical high-pass filter ( $< 600\,\text{nm}$ ) is employed to block the excitation laser light, since its intensity is several orders of magnitude higher than the fluorescence light, which would therefore be very hard to detect. The

remaining fluorescence light is then split by a 90:10 beamsplitter, and the main part is guided into a photo diode (PD) to detect the ODMR signal, while the remaining 10% are detected by a CMOS-camera. The camera comes in very handy in coarse-adjusting the xyz-stage to find suitable diamonds by directly imaging them on the experiment's PC. To acquire a high contrast ODMR-signal, the positioning of the diamond on the microwaveguide is of critical importance because the contrast of the signal correlates positively with the electric field strength. Figure 18 shows the electric field distribution of the waveguide showing that the E-field is strongest in the gap between the small conduction strip and the grounds. With this gap being roughly 250  $\mu\text{m}$  wide, the diamonds can be placed in there without a problem, limiting the scanning range of the xyz-stage to a well known area.

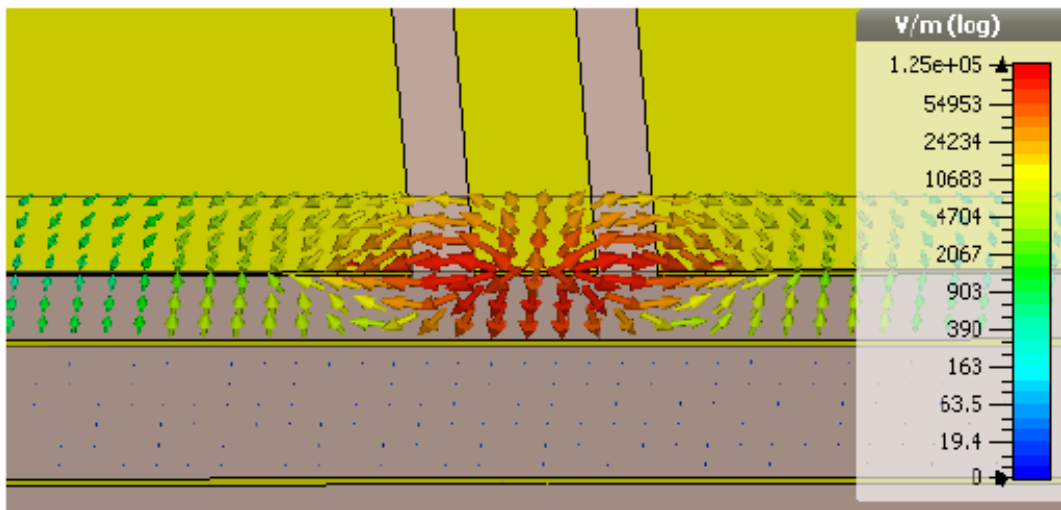
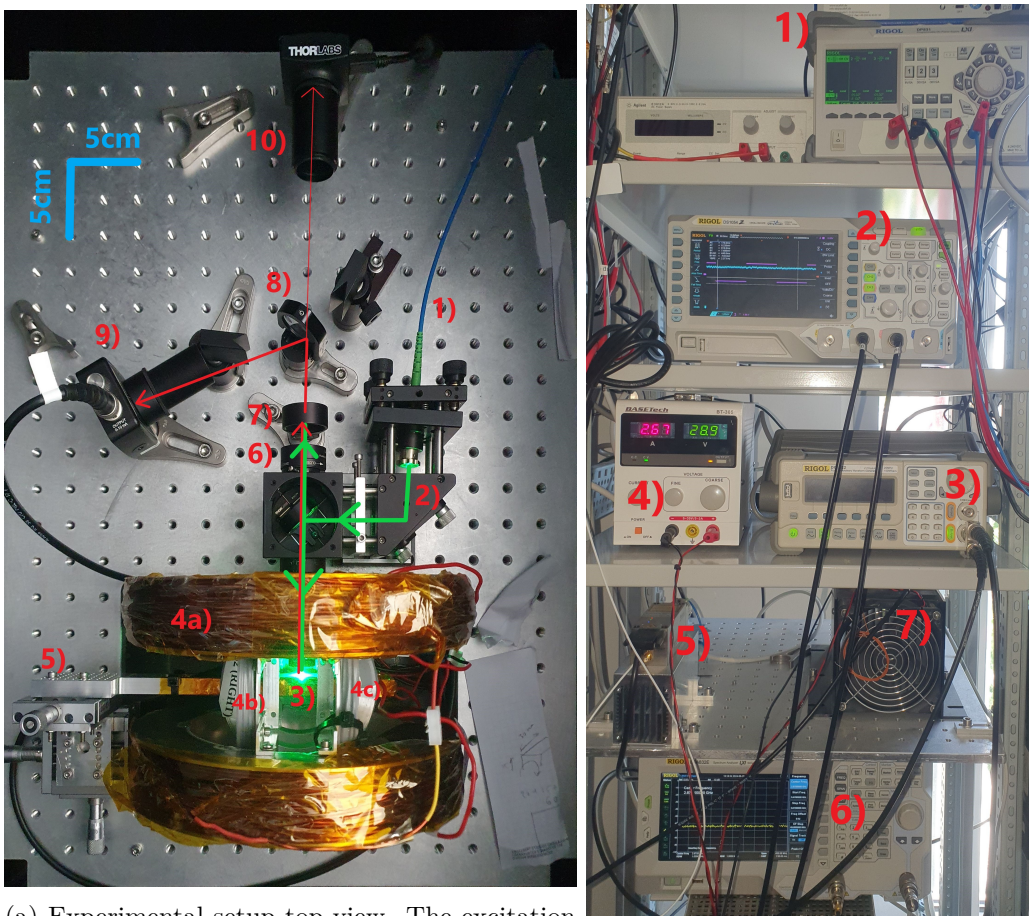


Figure 18: Simulation of the electric field in the coplanar waveguide, adapted from [Bunea et al., 2014]. The electric field is the strongest in the gap between the conduction strip (center) and the ground (left and right). The scale is not applicable for this experiment but indicates the strong exponential dependence of the electric field regarding the position.



(a) Experimental setup top view. The excitation laser beam (indicated by the green arrows) enters the setup via a fibre (1), where it is coupled out and sent through an arranged setup of two mirrors (2) to the micro-diamond, which is positioned on a microwaveguide (3). It is focused onto the diamond via an aspheric 10mm focal length lens (hidden beneath the large coil pair (4a)). The diamond (3) positioned in the center of the Cartesian setup of coil pairs in near Helmholtz configuration (4a-c) and can be moved in space by a xyz-translation stage (5). The waveguide and the diamond reflect parts of the excitation laser, where the diamond also sends out fluorescence light (red arrow) around the ZPL 637 nm up to the infrared regime (see Figure 16) of much lower intensity compared to the excitation laser. Both reflection and fluorescence are focused then by a 125 mm focal length lens (6) to the detection components. To get rid of the high intensity excitation laser light, an optical high-pass filter (7) is employed, blocking light below  $\lambda = \approx 600$  nm. The remaining fluorescence light is then parted by a 90:10 beamsplitter (8), where the main part goes to the Photodiode (PD) (9) detecting the signal strength and the 10% is detected by the CMOS camera (10) to visualize the diamond on the PC monitor.

(b) Experimental setup of the electronic rack. Appearing in the order following the setup description to the left: The Toptica IBEAM-SMART-515-S (5) provides the green 519 nm excitation laser of the experiment. The microwaveguide is driven by the RIGOL DSA1030 spectrum analyser (6), which's output signal is amplified by the Mini Circuits ZHL-16W-43-S+ (42 dB) amplifier (7). On the picture only the cooling fan (black) is visible, on which it is mounted. The amplifier is powered by the BASETech BT-305 power supply (4). The coil pairs of the setup can be individually driven by the threefold current supply RIGOL DP831 (1). The oscilloscope RIGOL DS1054 (2) is displaying the signal from the PD of the setup (blue on the monitor). To properly display the ODMR signal at the oscilloscope, both the spectrum analyser and the oscilloscope are triggered by a square function (magenta line on oscilloscope display) of the function generator RIGOL DG1022 (3).

### 3 Establishing a stable magnetic field setup for the Octagon ion trap vacuum chamber

#### 3.1 Calibration and systematics

##### 3.1.1 Systematic influence of the Hall sensors current supply

From equation [Equation 2.3](#) one can see that the current  $I$  driving the Hall sensor also has an impact on the output Hall voltage and therefore its fluctuation. The current supply driving the Hall sensor is a Agilent E3612A. To take this systematic into account, for every measurement with the Hall sensor, the current is measured, too. Assuming the linear correlation as from [Equation 2.3](#), a linear fit of  $U_{Hall}$  vs  $I$  is made as exemplary shown in [Figure 20](#). Subtracting the fit from the data effectively reduces the uncertainties.

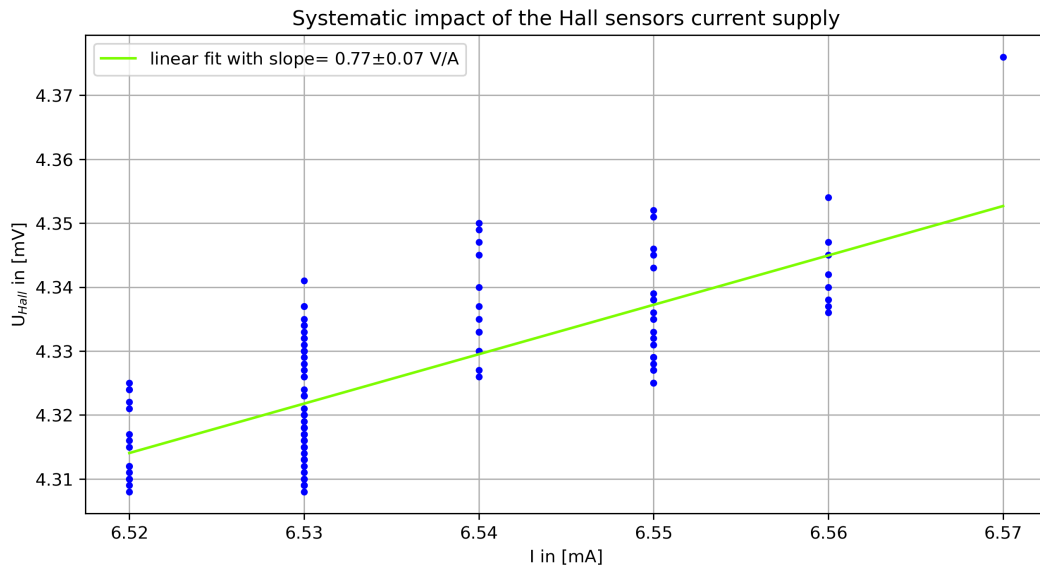


Figure 20: Systematic influence of the Hall sensors current supply. Subtracting the linear fit from the data reduces the uncertainties effectively.

##### 3.1.2 Positioning of the Hall sensor

To place the Hall sensor into the center of the test setup introduced in [Figure 8](#), it is mounted to an xyz-table. First it was placed there as good as possible by eye and geometry calculations, then two position calibration measurements were performed:

1. An axial measurement of the  $B$ -field along the quantization axis of the two magnets screwed on the test setup to find the minimum position in x-direction
2. An radial measurement of the  $B$ -field at the center position, to adjust the position in the yz-plane.

The first measurement is displayed in [Figure 21](#). It was performed with each single magnet and both magnets at once to see the field minimum and the individual magnet strengths. As a result, the magnetically measured minimum and the first positioning deviated by 0.5 mm, which is also the resolution in vicinity of the center. On the other hand, one magnet was damaged (as seen on the left side of [Figure 8](#)) and the single magnet measurement of the damaged one shows a general weaker field than the other, therefore the combined field is prone to shifts of the minimum in the same direction the magnetically measured minimum is shifted compared to the first positioning. This led to the decision to keep the initial position of the x-direction. Note that the damaged magnet is not part of the final setup.

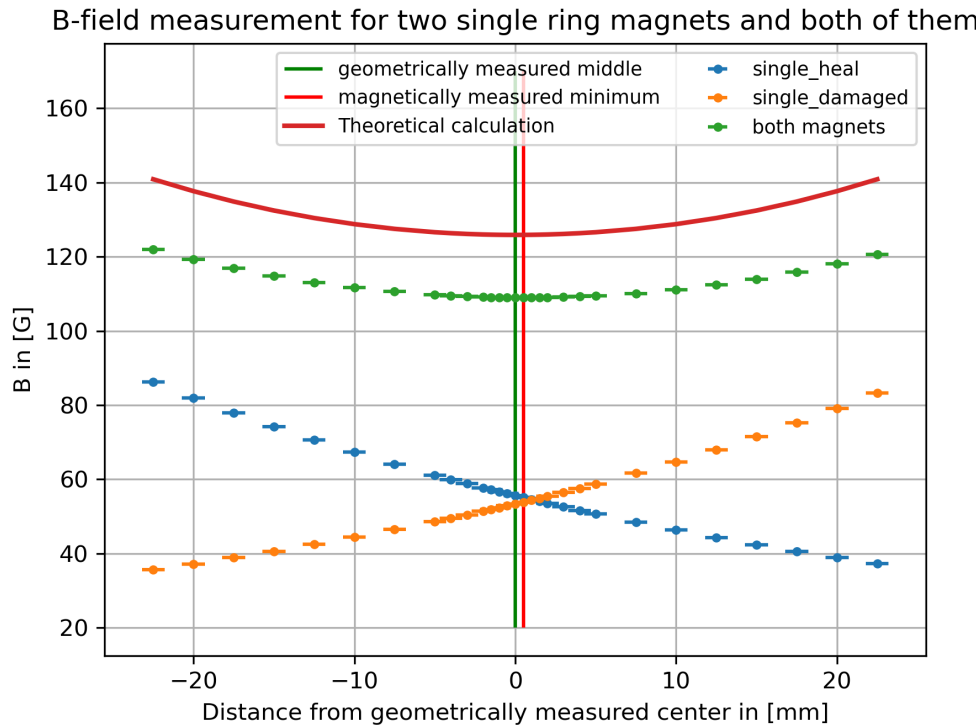


Figure 21: Axial measurement of the  $B$ –field strength with a hall probe. Three measurements were made, two with the different single magnets (blue+orange) and one with both together (green), showing a discrepancy of 0.5 mm between hand-prepared center position ('geometrically measured middle') and the measured  $B$ –field minimum. As one can see from the legend, the orange magnet is damaged and therefore lightly weaker (also seen when comparing the single curves), thus no change in the axial direction was made because the measured  $B$ –field minimum might be affected by that. It is notable, that the measured value of both magnets (green) is about 15 – 20 G smaller than the theoretical value from [Equation 2.4](#).

The second measurement is depicted as a 2D- plot in Figure 22. A  $12\text{ mm} \times 12\text{ mm}$  part of the  $yz$ -plane around the first positioned center with the resolution of 1 mm is mapped. Colored dots indicate the strongest field in each row and column, leading to the conclusion, that the set  $z$ -position was initially good adjusted, while the  $y$ -position was changed by  $-1.5\text{ mm}$ . This final setting is the new position, all following measurements were performed on.

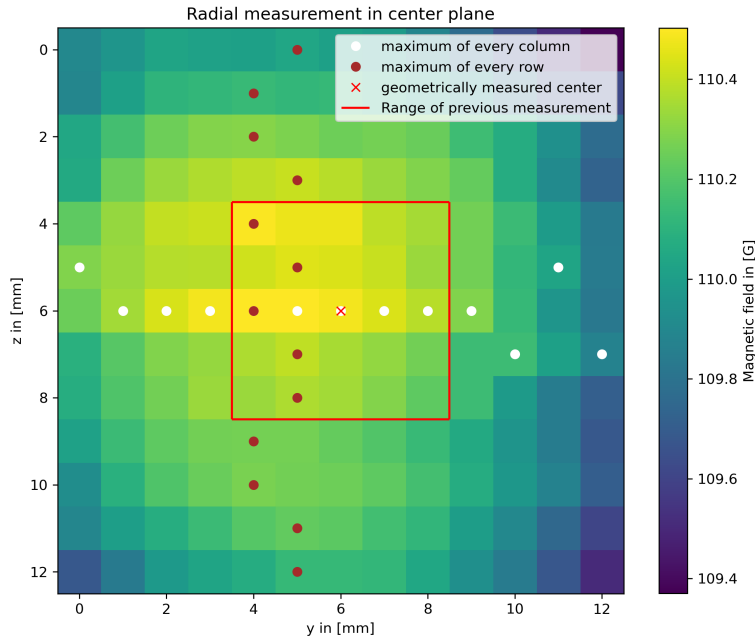


Figure 22: Radial plane measurement with  $\pm 6\text{ mm}$  variation in the radial  $y$ - and  $z$ -directions in 1 mm steps from the hand-prepared center (red x). The color indicate the magnetic field strength according to the colorbar. The red box indicates a previous measurement, which covered not enough space. Dark red and white dots show the maximum value of every row and column, respectively. This yields, that the  $z$ -position is good adjusted, while in the  $y$ -direction with alternating maxima ( $-2\text{ mm}$  and  $-1\text{ mm}$ ) there has to be a  $-1.5\text{ mm}$  change towards the negative direction.

### 3.2 Choosing a suitable ring magnet thickness

To choose the right magnet thickness to acquire a center magnetic field of  $109.64\text{ G}$  with a minimal distance  $d_{min} = 254.8\text{ mm}$  from Equation 2.5, the  $12\text{ mm}$  thick magnet from [Hakelberg et al., 2018] is to weak. For this distance,  $16\text{ mm}$  and  $20\text{ mm}$  thick magnets were tested. Since the rings regarding the overgrowth (see Equation 2.5) needed to be added later, only measurements for  $d'_{min} = 244.4\text{ mm}$ , so  $10\text{ mm}$  less than  $d_{min}$ , were performed. In general, a magnetic field a few Gauss

stronger than 109.64 G at  $d_{\min}$  is favourable, because the distance can always be increased and therefore the field weakened.

The results of the 16 mm magnets are shown in [Figure 23](#). The minimum almost matches the desired  $B$ -field, but with 10 mm in addition the field would be too weak.

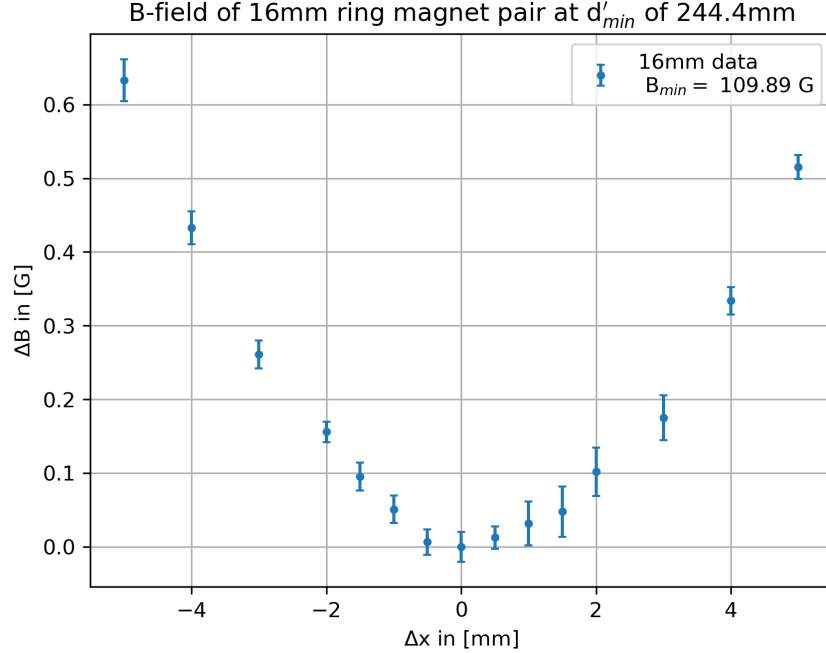


[Figure 23](#): The magnetic field around the center of the 16 mm magnets. Each data point is the average of 8 single values. The values are recorded with a resolution of 0.5 mm around the center. The asymmetry for this plot could be explained by the damaged magnet discussed before.

The measurement for the 20 mm thick magnet is displayed in [Figure 24](#). With a minimum of 121.08 G the  $B$ -field strength is above the desired field strength. Considering the additional 10 mm and the tuning parameters from [subsection 3.3](#), the minimum value of the field is still  $> 109.64$  G. For this measurement the current supply was stable and within one datapoint there was barely fluctuation, as seen in the not visible error bars of the plot. Still there is this unexpected local maximum in vicinity of the dip and also the overall asymmetry of the plot, comparing the outer values of it. This time, different magnetic field strengths of the individual permanent magnets should not be the reason, since these are both not damaged. Therefore either long-term drifts due to non-ideal measurement procedure (left to right, not random in position) or an actual minimum shift of  $\approx +0.5$  mm (comparing the value pairs [-4, 5] mm and [-3, 4] mm). The latter option can not be confirmed at the center due to the local maximum distorting the field. This maximum can

be identified as a mid-term drift of the magnetic field (on the orders of minutes), since all values of one averaged data point are taken within 1 min, depicting only short-term fluctuations. This measurement(-procedure) was not ideal, but it shows a value well above 109.64 G. This led to the decision that the 20 mm thick magnets should be employed. With this, the coarse and fine tune parameters of the setup are extracted in the next subsection.

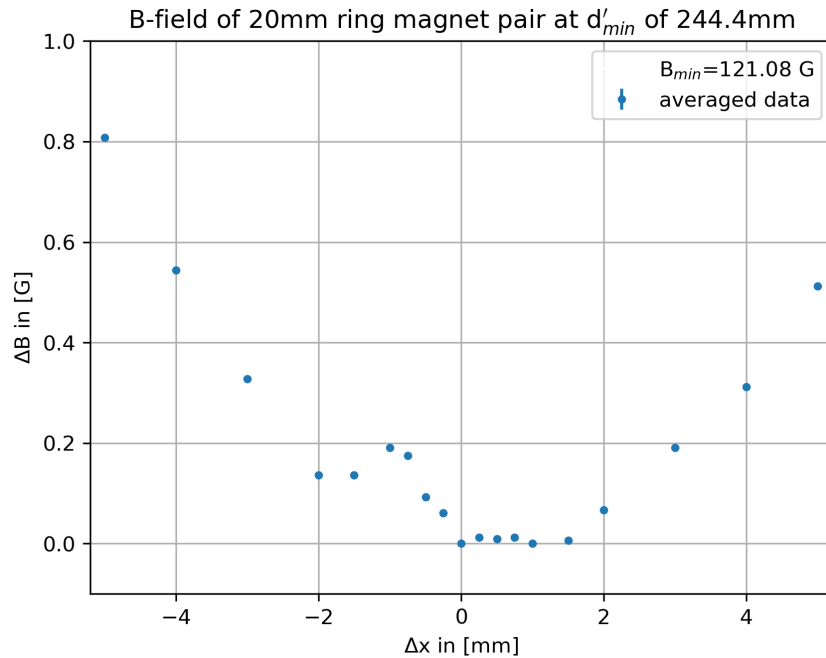


Figure 24: The relative magnetic field around the center of the 20 mm magnets. Each data point is the average of 8 single values. For this measurement the current supply was stable and no mentionable short-term fluctuations led to the non-visible error bars. The values are recorded with a resolution of 0.25 mm around the center. The local maxima induces the presence of mid-term fluctuations of magnetic stray fields and the asymmetry of the plot could be explained by either long-term drifts or a shift of the minimum of  $\approx +0.5$  mm.

### 3.3 Tuning parameters towards $B = 109.64$ G

To tune the  $B$ -field at the center of the chamber, two parameters at the setup can be changed:

1. Coarse tuning of the magnetic field by changing the distance  $d$  between the permanent magnets
2. Fine tuning of the magnetic field by adjusting the current of the coil pair parallel to the quantization axis

The coarse tuning can be achieved by moving the magnet holder on the M53x1 thread of the magnet-and-coil-fixer. The 'x1' means a thread pitch of 1 mm, so a full turn displaces the magnet by 1 mm. Doing this in symmetry for both directions to keep the  $B$ -field minimum in the center, one turn in [Figure 25](#) equals 2 mm. Fitting a linear function to the data, it yields a slope of  $\approx -2 \text{ G/turn}$ . Looking at the residuals, the more complex behaviour based on [Equation 2.4](#) can be seen, but for the practical use of this *coarse* tuning in this small region of  $d$  a linear description is more fitting.

The fine tuning of the  $B$ -field can be achieved by the coil pairs of the setup, especially by the coil in quantization direction. The coil pairs magnetic field depends linear on the driving current following [Equation 2.6](#). Varying the current is shown in [Figure 26](#). The dependency of the magnetic field regarding the current was found to be  $(0.744 \pm 0.016) \text{ G/A}$ . With the desired use of currents below 100 mA to keep heating of the coil negligible, corrections of to  $\pm 0.07 \text{ G}$  could be achieved with this.

These two parameters are the most important 'knobs to turn' reaching the desired  $B$ -field.

## 4 The $^{25}\text{Mg}^+$ ion as quantum sensor

The trapped  $^{25}\text{Mg}^+$  ion is first employed as a quantum sensor to create a reference for a later comparison with the diamond. The whole experiment undergoes daily calibration of laser and microwave frequencies and many other parameters, which to describe would exceed the scope of this thesis. At the time the following experiments were conducted, the setup was calibrated, especially the microwave driving frequency was adjusted to the  $|3, 3\rangle \leftrightarrow |2, 2\rangle$  transition frequency.

### 4.1 Coherence time extraction

To use the trapped ion as a quantum sensor of type II (relying on coherent states) it is crucial to know the coherence time of the system. Not only the knowledge of the maximum operation time itself is of importance, but sensing qualities improve with long coherence times, too. In [subsubsection 2.6.1](#) one repetition of the Ramsey sequence is described. To gather sufficient amount of statistics to extract the coherence time  $T_{2*}$ , few hundreds of repetitions for the same  $t_{\text{Ramsey}}$ , same  $\varphi'$  and same driving frequency  $\omega$  need to be taken to estimate the population amplitudes of the detected state,  $c_{|0\rangle}^2$  and  $c_{|1\rangle}^2$  (this equals to one data point in [Figure 27](#)). To calculate the coherence time of the qubit, this needs to be repeated for different values of  $\varphi' \in [0, 2\pi[$  (performing the phase scan,  $t_{\text{Ramsey}}, \omega$  constant) as depicted in [Figure 27](#). On top,  $t_{\text{Ramsey}}$  will be varied from values between 0 and  $\approx 2 \times T_{2,\text{expected}*}$ , which is in this experiment  $600 \mu\text{s}$ .

Fitting now a cosine function based on the  $c_{|0\rangle}$  from [Equation 2.9](#) to all phase scans

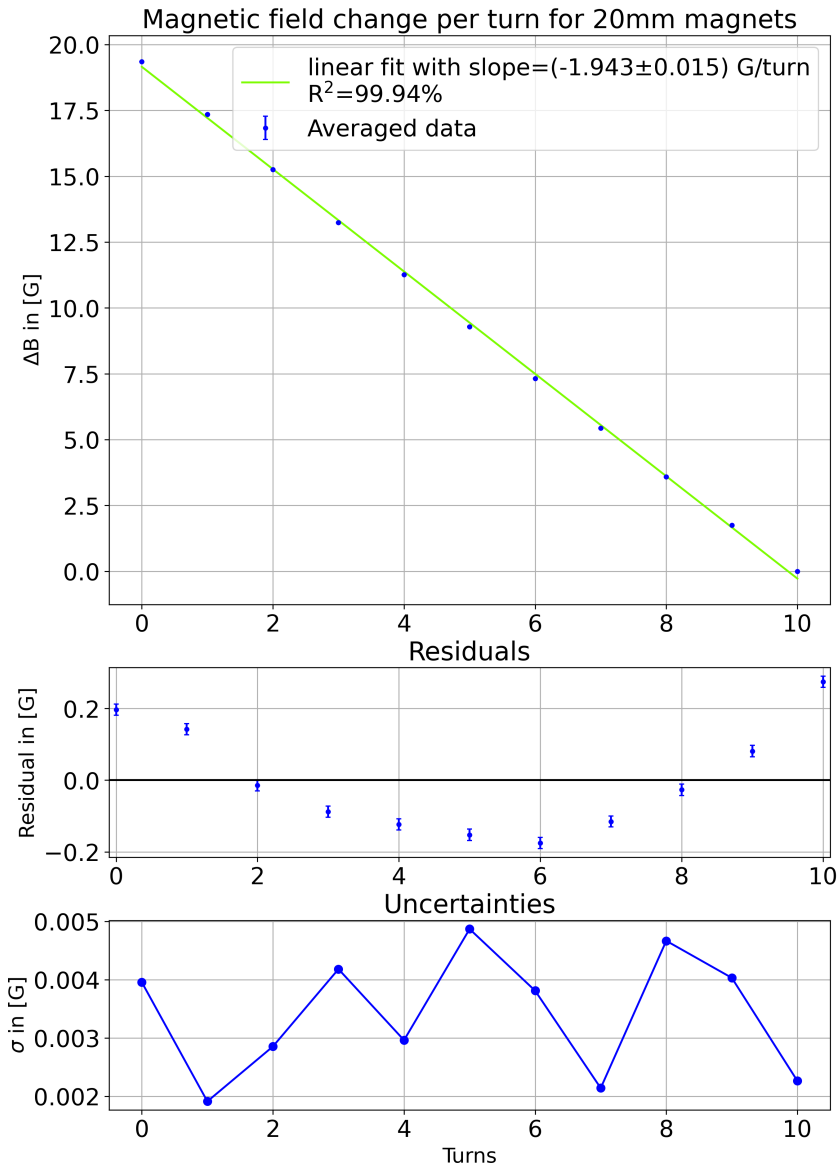


Figure 25: Linear fit of the  $B$ -field change per turn. One  $360^\circ$  turn on the underlying M53x1 thread means 1 mm increase in distance between the ring magnets. To keep the  $B$ -field symmetric at the center, both magnets are turned equally towards the outside. Therefore one turn equals 2 mm increase in distance between the magnets, yielding a change of  $(-1.943 \pm 0.015)$  G/turn. The residuals indicate the more complex than linear nature of the  $B$ -field's distance dependence, which is shown in Equation 2.4, but for this range of application the linear approach is practical, since this parameter optimization towards  $B = 109.64$  G is the first, coarse tuning. The uncertainties are rather small and not visible in the main plot and therefore depicted at the bottom in their own plot. These uncertainties only depict short term fluctuations ( $> 1$  min).

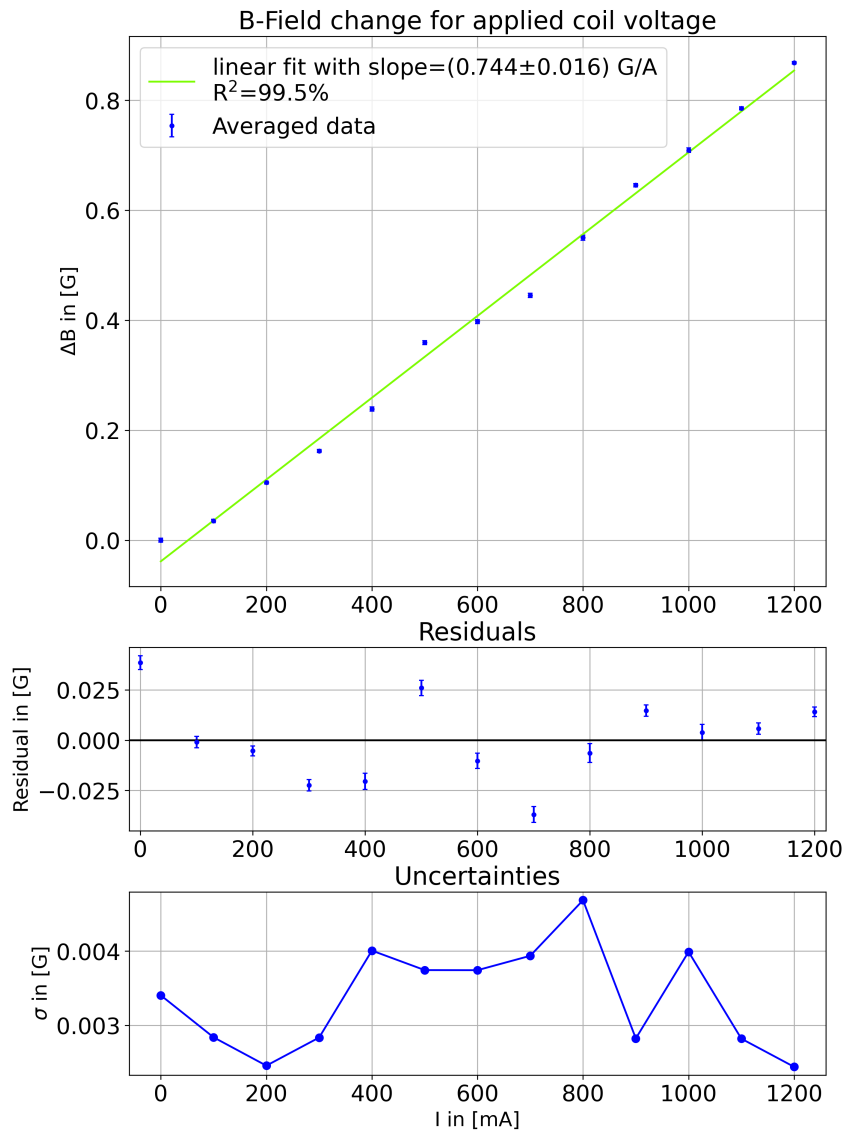


Figure 26: Linear fit of the coil's  $B$ -field change per current yields  $(0.744 \pm 0.016)$  G/A. Since only small currents ( $> 100$  mA) will be used to keep the coils' heating redundant, these coils can tune the field up to  $\pm 0.07$  G. Therefore this parameter optimization is suited to be the second, fine tuning one. The residual shows no particular behaviour like in Figure 25 strengthening the hypothesis of a linear behaviour from Equation 2.6. The uncertainties are rather small and not visible in the main plot and therefore depicted at the bottom in their own plot. These uncertainties only depict short term fluctuations ( $> 1$  min).

like

$$\frac{|A|}{2} \cdot (h - \cos(2(\cdot\varphi' + \Delta\theta))), \quad (4.1)$$

where  $A$ ,  $h$  and  $\Delta\theta$  are the fitting parameters. The factor 2 in the cosine comes from the fact, that a variation of the experimental phase in the ARTIQ sequence from 0 to  $2\pi$  equals two full cycles ( $4\pi$ ) of  $\varphi'$ .  $A$  gives the contrast of the fitted function used later for the coherence time plot. The absolute value of  $A$  is used to prevent unwanted phase shifts during fitting for  $\Delta\theta$  from equalities like  $+A/2 \cdot (+h - \cos(x)) = -A/2 \cdot (-h - \cos(x \pm \pi))$  or similar.  $A$  itself represents the contrast between the computational basis as a absolute value difference of minimal (corresponding to  $|1\rangle$ ) and maximal ( $|0\rangle$ ) counts giving rise to the estimation of the coherence time  $T_{2*}$ . From the evolution of  $\Delta\theta$  for different Ramsey times, later the  $\Delta\omega$  frequency difference of the can be extracted to derive the magnetic field. The offset parameter  $h$  is not needed for further analysis but can be used to double check for mentioned phase jumps (if the value stays positive for different  $t_{\text{Ramsey}}$ , it is fine). When looking at the uncertainties of the counts and comparing them with the possible uncertainties from [Equation 2.10](#), almost non of these can be identified here. The only difference in the uncertainties can be seen in correlation with the square root of the signal strength and therefore is dominated by the shot noise from poisson statistics, which is about one order of magnitude weaker than the signal. No influence of the pump noise is recognised, being the dominating noise at the dips and  $\approx 0$  at the peaks. Also no impact of the quantum projection noise, usually dominating at the steep slopes between peaks and dips, can be seen. Subtracting the shot noise from the uncertainties, only leaves residuals nine orders of magnitude lower than the signal, which can be neglected. The measurement is therefore limited by shot noise.

For the estimation of  $T_{2*}$ , the contrast values  $|A|$  are plotted against  $t_{\text{Ramsey}}$  as shown in [Figure 28](#). An exponential decay of the contrast can be seen, caused by the decoherence effects blurring and eventually destroying the well defined phase relation  $\varphi$  between the  $|0\rangle, |1\rangle$ -states picked up during the free evolution during  $t_{\text{Ramsey}}$  (see [subsubsection 2.6.1](#)). The  $T_{2*}$  time is defined as the time, the  $e$ -function decays to the  $1/e$  value and can be extracted by the fit

$$\text{Contrast}(t_{\text{Ramsey}}) = A_{\text{con}} \cdot e^{-\left(\frac{t_{\text{Ramsey}}}{T_{2*}}\right)^2} + h, \quad (4.2)$$

where  $A_{\text{con}} \approx A(t_{\text{Ramsey}}) = 0$  and  $h$  are fitting factors to enable a good fit, but are of no further importance. The coherence time as third parameter of this function is

$$T_{2*} = (378.18 \pm 55.71) \mu\text{s}, \quad (4.3)$$

Showing a large errorbar of almost 15% relative strength, because the contrast data shows relatively large fluctuations. There are other ways to calculate the contrast, which might be more exact. For the matter of this thesis, the rough  $T_{2*}$  value given by the direct extraction from the count difference contrast is giving an idea of the principle.

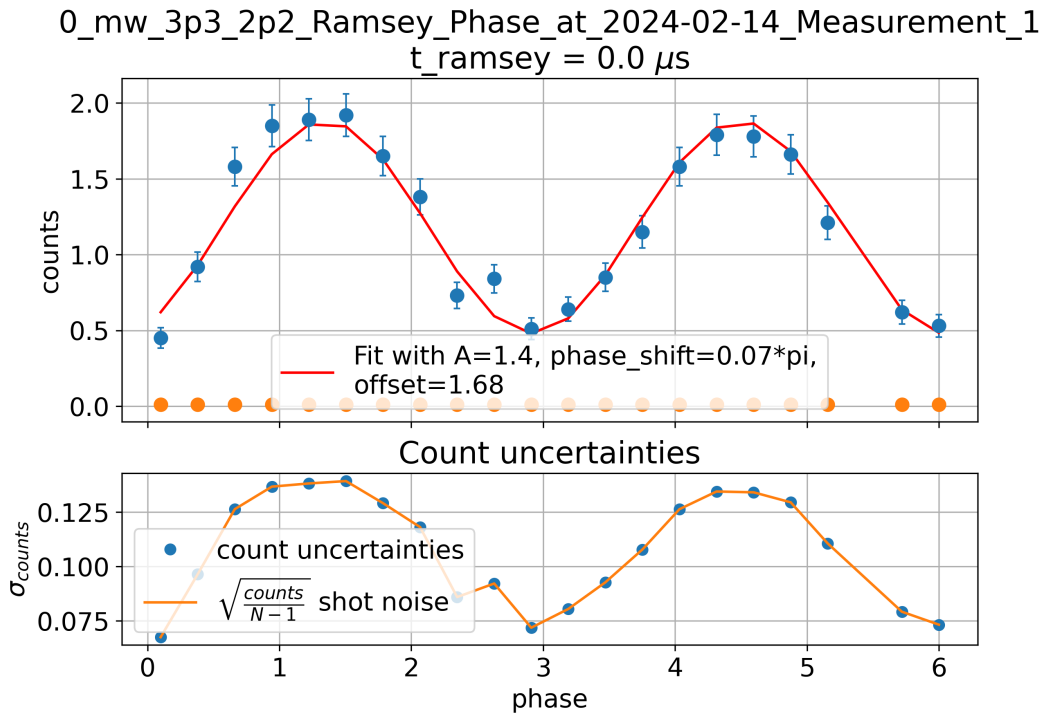


Figure 27: Exemplary phase scan for fixed  $t_{\text{Ramsey}} = 0 \mu\text{s}$ . The sinusoidal behaviour of the detected counts is correlated to the population amplitude  $c_{|0\rangle}$ , since the detection method used employs the ground state  $|0\rangle$  as the bright state. For the  $T_{2^*}$  time extraction the amplitude  $A$  displaying the contrast of the phase scan is of importance, while the phase shift  $\Delta\theta$  will be utilized for  $B$ -field sensing. The uncertainties show strong correlation with the square root of the signal strength divided by  $N - 1$ , where  $N = 100$  and is the number of repetitions for one data point of the experiment. The shot noise is therefore the dominant source of uncertainty.

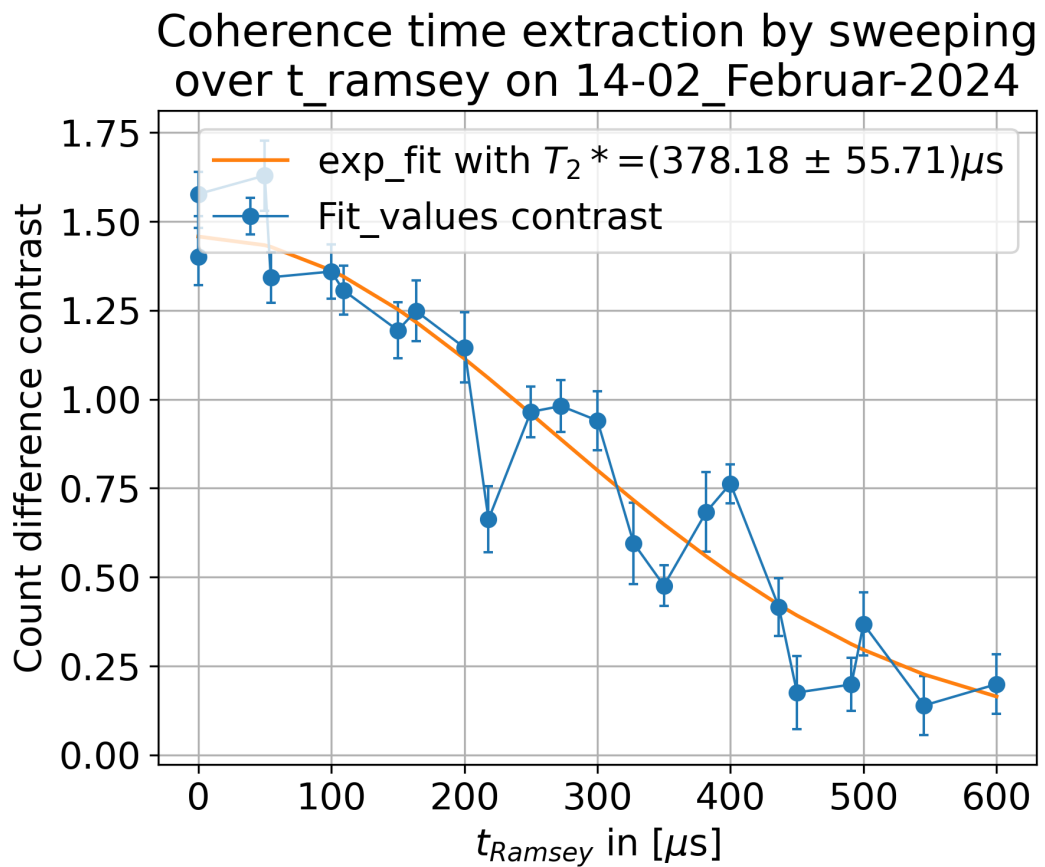


Figure 28: Coherence time extraction from the count difference contrast vs.  $t_{\text{Ramsey}}$ . Value fluctuations of the contrast lead to a large error of the  $T_2^*$  time.

## 4.2 $B$ -field estimation

To recalculate the  $B$ -field from the Breit-Rabi formula, first the transition frequency  $\omega_0$  needs to be estimated, which is composed of

$$\omega_0 = \omega + \Delta\omega, \quad (4.4)$$

where  $\omega$  is the known driving frequency of the external field (microwave) and  $\Delta\omega$  the frequency difference between driving field and the qubit transition, which can be extracted from the  $\Delta\theta$  of the phase scan fits. From the coefficient comparison of [Equation 2.9](#) and [Equation 4.1](#) (neglecting the factor 2 of the latter) this yields

$$\Delta\theta = \Delta\omega \cdot t_{\text{Ramsey}} \quad (4.5)$$

looking at the development of  $\Delta\theta$  vs.  $t_{\text{Ramsey}}$ , depicted in [Figure 29](#), shows a linear behavior and therefore the slope of a linear fit yields

$$\text{slope} = \frac{\Delta\theta}{t_{\text{Ramsey}}} = \frac{\Delta\omega \cdot t_{\text{Ramsey}}}{t_{\text{Ramsey}}} = \Delta\omega = (4.56 \pm 0.49) 2\pi \times \text{kHz}. \quad (4.6)$$

with the driving frequency  $\omega = 1541.07 2\pi \times \text{MHz}$  this yields

$$\begin{aligned} \omega_0 &= 1541.07 2\pi \times \text{MHz} + (0.00456 \pm 0.00049) 2\pi \times \text{MHz} \\ &= (1541.07456 \pm 0.00049) 2\pi \times \text{MHz} \end{aligned} \quad (4.7)$$

The uncertainty of the microwave driving field is not known here, but should be partially contained in the uncertainty of  $\Delta\omega$ , since  $\sigma_{\Delta\omega} = \sqrt{\sigma_\omega^2 + \sigma_{\omega_0}^2}$  and should therefore be of the same order of magnitude. but since this is 7 orders of magnitudes weaker compared to the transition frequency in the low GHz regime, it will not further be investigated. Recalculating the  $B$ -field from the frequency with the Breit-Rabi formula in [Equation 2.8](#) yields

$$B = (109.59870 \pm 0.00023) \text{ G} \quad (4.8)$$

with a relative uncertainty of  $\approx 2.1 \times 10^{-6}$ . The principle of sensing a magnetic field to a high precision with a trapped ion is therefore shown. This measurement example was performed after calibration of the microwave driving field to the transition frequency, therefore only few kHz deviation were detected. There are some boundaries for this method, because you more or less should know in advance, which magnetic field strength or at least which order of magnitude is applied to the ion, since highly off-resonant driving frequencies on the one hand make it harder to perform the  $\pi/2$ -pulses of the Ramsey sequence successfully and on the other hand the resulting high  $\Delta\omega$  induces many  $2\pi$  jumps for even low  $t_{\text{Ramsey}}$  difference times, therefore a much finer resolution for the  $t_{\text{Ramsey}}$  time has to be accounted for to register all phase jumps of the phase scan fitting parameter  $\Delta\theta$  properly, otherwise this would lead to a miscalculation of the frequency and therefore the magnetic field. A previous

frequency scan with the driving field to roughly identify the transition frequency  $\omega_0$  needs to be an integral part of measuring protocols dealing with unknown magnetic field strengths.

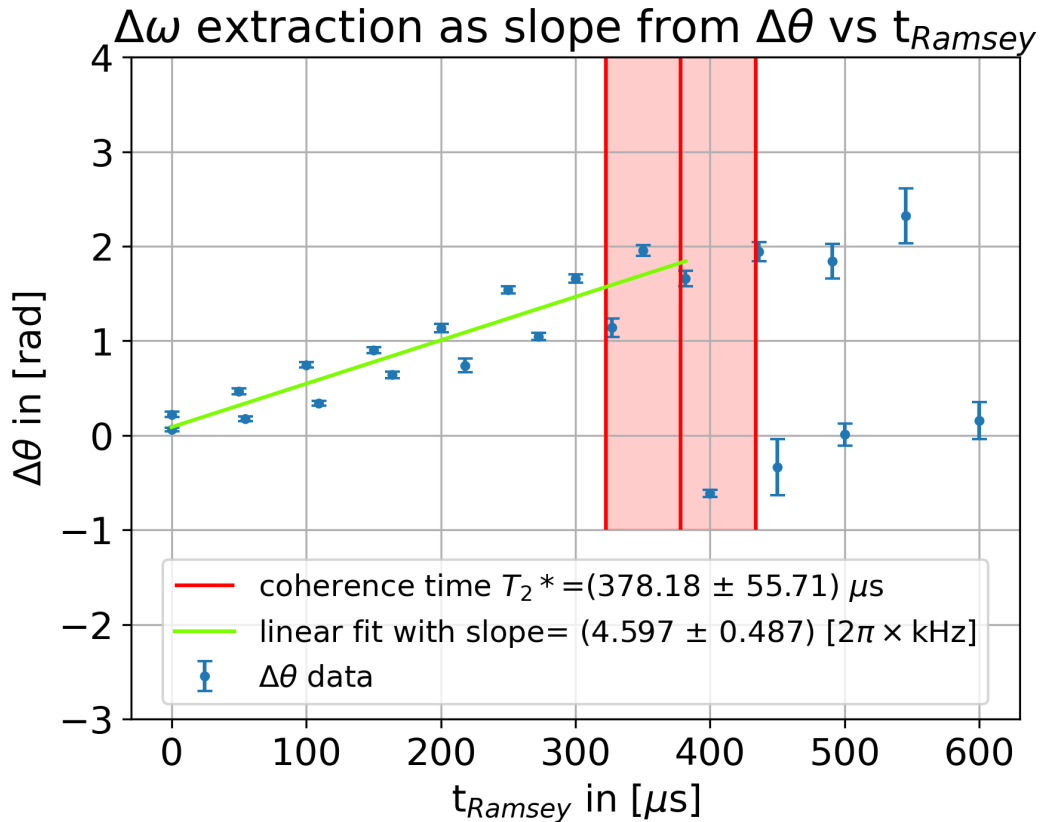


Figure 29:  $\Delta\omega$  extraction

#### 4.3 Sensitivity of the $|3, 3\rangle \leftrightarrow |2, 2\rangle$ transition

To estimate the sensitivity of the chosen transition at a certain magnetic field, The  $B$ -field strength is slightly altered with the coil pair along the quantization axis ( $z$ -direction). For every alteration (in random order, multiple times for each alteration), a frequency scan is performed. At every frequency step of that scan, 300 repetitions of a microwave  $\pi$ -pulse are performed and then the state is detected as described in Figure 12. Resonant with the transition frequency, a dip in the fluorescence counts is detected which corresponds to a complete state inversion of the bright state ( $|3, 3\rangle \equiv |0\rangle$ ) into the dark state ( $|2, 2\rangle \equiv |1\rangle$ ) regarding detection. The microwave pulse of strength  $b$  and frequency  $\omega$  inducing the  $\pi$ -pulse within a certain time  $t_{\text{pulse}}$

is a square function in time like

$$f(t) = \begin{cases} b, & \text{if } -t_{\text{pulse}}/2 < t < t_{\text{pulse}}/2, \\ 0, & \text{otherwise.} \end{cases} \quad (4.9)$$

Therefore in the frequency space the dip has the form of the Fourier-transform of the pulse, which is the sinc-function [Karpfinger, 2022]. To fit the observed dip the fit function

$$\text{sinc}(\omega) = A \cdot \left( \frac{\sin(k(\omega - \omega_0))}{k(\omega - \omega_0)} \right) + h \quad (4.10)$$

is employed, where  $A$  and  $h$  are the standard scale and offset parameters,  $k$  induces a quenching/stretching of the dip width and  $\omega_0$  is the important quantity to extract. The coil current  $I_z$  was varied by  $\approx 10\text{ mA}$  by the control voltage of the current driver according to [Table 2](#)

control voltage [V]	z-coil pair current $I_z$ [mA]
1.8	24.87
2.0	26.88
2.2	28.88
2.4	30.88
2.6	32.89
2.8	34.90

Table 2: Current control voltage conversion of the z-coil pair.

One exemplary fit for the sinc-function is displayed in [Figure 30](#). From all extracted frequencies of the same current the weighted average and uncertainty is calculated since all the extracted values already have uncertainties on their own and are comparable within these. Again converting the frequencies with the Breit-Rabi-formula yields the linear impact of the coils regarding the  $B$ -field as

$$\frac{\partial B}{\partial I_z} = (-2.653 \pm 0.011) \text{ G/A} \quad (4.11)$$

as fitted in [Figure 31](#). The final estimation of the sensitivity in the B-field region is to plot the fitted frequency against the calculated  $B$ -field and approximate the local slope by a linear fit. With a region of only  $\approx 0.02\text{ G}$  change within the  $10\text{ mA}$  current variation, this is applicable. The sensitivity, estimated in [Figure 32](#), yields

$$S_{\text{ion}} = (-2175.61 \pm 0.53) 2\pi \times \text{kHz/G}. \quad (4.12)$$

Comparing this with the calculated sensitivity  $S_{\text{ion,calc}} = -21.764 2\pi \times \text{MHz/mT} = -2176.4 2\pi \times \text{kHz/G}$  from [Table 1](#), the measured value is within  $1.5\sigma$  comparable.

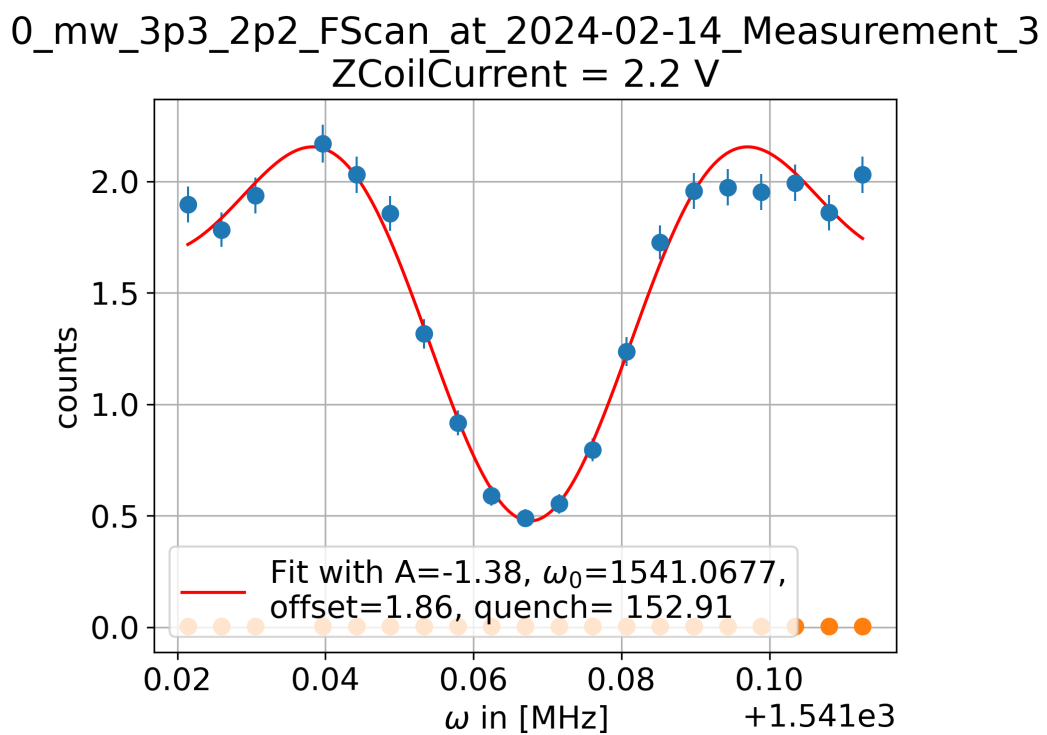


Figure 30: Exemplary sinc function fit for the set control voltage of 2.2 V. From the fit parameters displayed in the legend, the  $\omega_0$  is of importance and will be used for the sensitivity estimation.

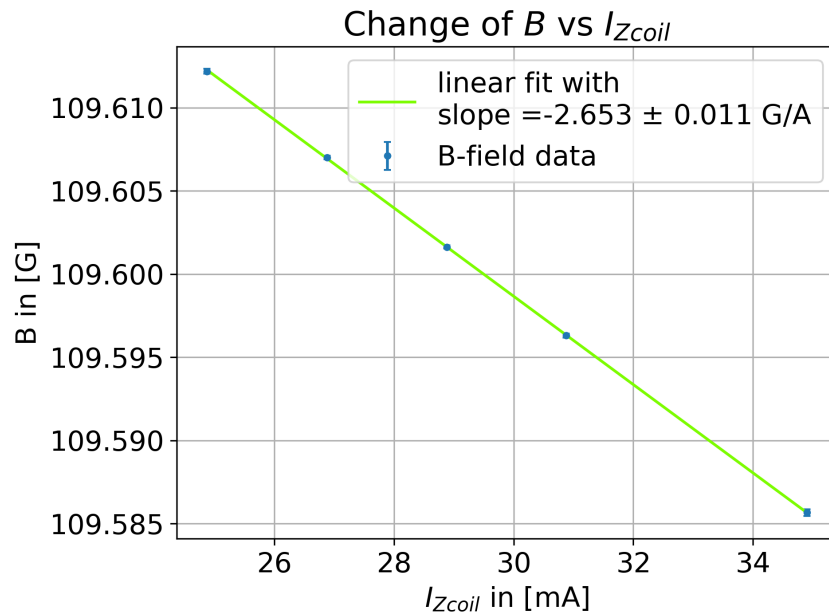


Figure 31: Linear impact of the coil current  $I_{Zcoil}$  on the  $B$ –field. The negative slope implies, that the  $B$ –field direction of the coils is anti-parallel to the field direction of the permanent magnets.

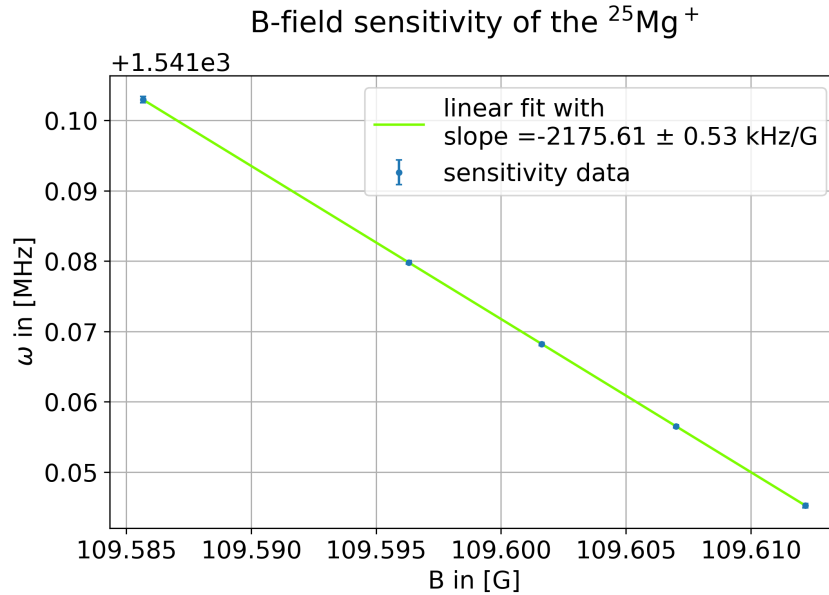


Figure 32: Measured  $B$ –field sensitivity of the ion. The  $|3, 3\rangle \leftrightarrow |2, 2\rangle$  transition is changing towards smaller values for stronger magnetic fields.

## 5 The diamond NV-center as quantum sensor

With the ion setting standards, next the NV-centers in diamond are employed as quantum sensors. First the experimental setup is characterized, finding optimal parameters and identifying systematics and in the second part the presents the sensing results and employs a new way to reconstruct the magnetic field strength from the results.

### 5.1 System characterization

#### 5.1.1 Laser calibration

The off-resonant excitation laser of the experiment needs to be calibrated to get an idea, which laser power reaches the diamond. It is a diode laser from Toptica (IBEAM-SMART-515-S) with green light around 519 nm and a power below 100 mW. To access the laser, a Toptica interface on the Lab-PC is used, which has only the option to set the power in this interface, no direct regulation by changing the diode current. Therefore in following chapters the referred to parameter of the laser is 'set (laser) power'. As seen in [Figure 33](#), the laser power is measured with a Thorlabs PM160T powermeter at two positions, namely at the output of the fibre and the rough position of the diamond. The linear range of the laser is 0.5 – 60 mW, for higher set power, the measured power saturates.

#### 5.1.2 Contrast and SNR vs. power

After finding the laser range, the optimal (set) laser power is estimated by looking at the SNR and the contrast of the ODMR signal without applied B-field. With [Figure 17](#) in mind, the contrast is defined as

$$\text{contrast} = \frac{\text{baseline- minimum}}{\text{baseline}} \quad (5.1)$$

while the *SNR* is calculated by

$$SNR = \frac{\text{contrast}}{\text{noise}} \quad (5.2)$$

Three slightly different estimation methods were applied, since every single one has its own disadvantages but show strong correlation as seen in [Figure 34](#). The green line employs the difference between the minimal point and the averaged baseline (apart the ODMR dip region). This represents the most easy way to get an idea of the contrast with the problem that this highly depends on the choice of the 'resonance free region' of the frequency scan. The next two employ a Lorentzian fit of the ODMR signal like

$$f(x) = -A \cdot \left( \frac{1}{\pi} \cdot \frac{\gamma}{(x - x_0)^2 + \gamma^2} \right) + h \quad (5.3)$$

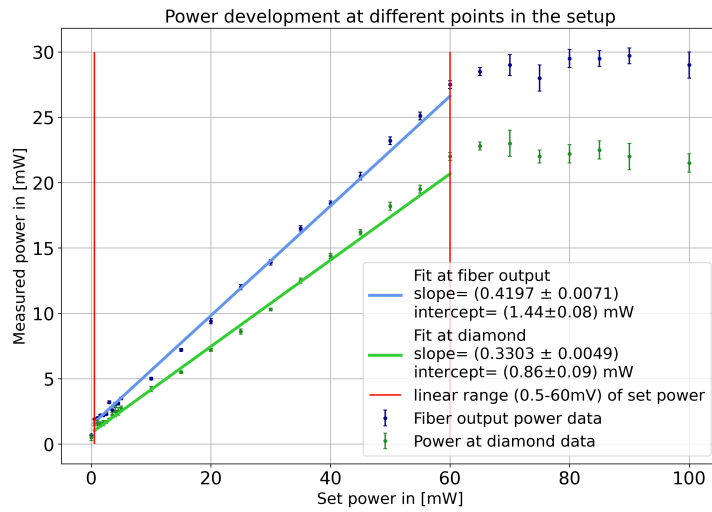


Figure 33: Calibration of the 519 nm excitation laser at different positions. The x-axis shows the laser power set in the Thorlabs interface of the laser, which might not represent the actual output power of the laser head, while the y-axis shows the measured power. Fits in the linear range of the laser were made at the position of the fiber output (blue) and at the position of the diamond (green). Since the actual output power of the laser head is unknown, the slopes can hardly be interpreted as efficiencies of the fibre coupling (like  $0.4197 \rightarrow \approx 42\%$  coupling efficiency of the fiber) but should be strongly correlated.

and calculate from these the minimal ( $f(x_0)$ ) and maximal values (side values of the spectrum) of the signal.  $A$  and  $h$  are the usual scaling and offset factors. The minus in front of the  $A$  indicates, that the observed ODMR signals are negative dips in the spectrum.  $\gamma$  depicts the FWHM of this distribution and  $x_0$  to position of the minimum value. The blue data corresponds to a single Lorentzian fit, but since the ODMR signal consists of two dips very close to each other, the fit systematically overestimates the contrast. The orange line addresses the presence of two dips by fitting a sum of two Lorentzians, but this fit fails sometimes, so the estimated contrast is relatively fluctuating in comparison to the single Lorentzian fit. All three methods together allow a qualitative estimation of the optimal laser power to use. The noise of the SNR is for all methods the average of the uncertainties of every value in the frequency scan. For the contrast, for two of three methods a maximum at 25 mW set laser power can be observed, for the third maximum at least a local maximum is identified. For the  $SNR$ , there is a steep rise from 20 mW to 25 mW set laser power, so from both plots (favouring the contrast) the optimal set laser power is 25 mW.

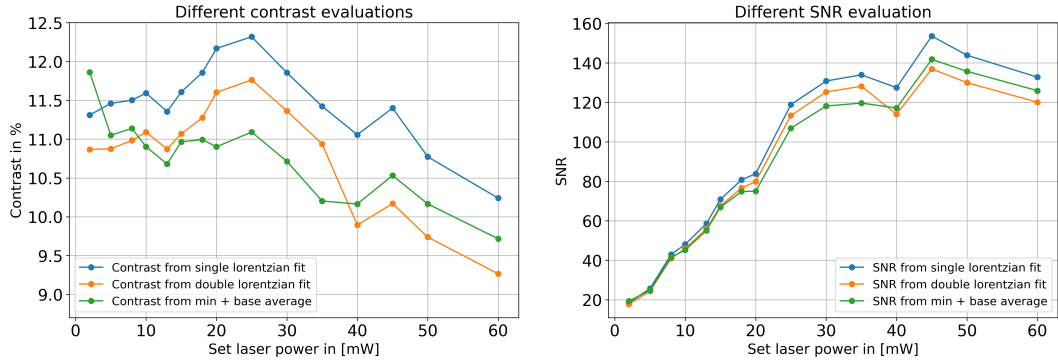


Figure 34: Contrast in relative values and signal to noise ratio (SNR) in absolute values vs. the set output power of the laser, without applied  $B$ -field. Different evaluation methods were used to calculate both quantities, where every single one has its disadvantages, but are mostly correlated helping to interpret the results. For the contrast the sweet-spot is at 25 mW set laser power, where two methods show their maximum and the third one has a local maximum. The absolute maximum of the third method is at the lowest laser power, but since the cause of main noise floor comes from the oscilloscope itself (see Figure 35), the SNR is bad at low powers. In addition, the oscilloscope's resolution is limited, therefore lower contrast signals (e.g. when a  $B$ -field is applied, see Figure 42) will be very hard to resolve. With a steep rise of the  $SNR$  after 20 mW set laser power the best spot to set the laser power is 25 mW. Considering the laser calibration in Figure 33,  $\approx 9.1$  mW reach the diamond.

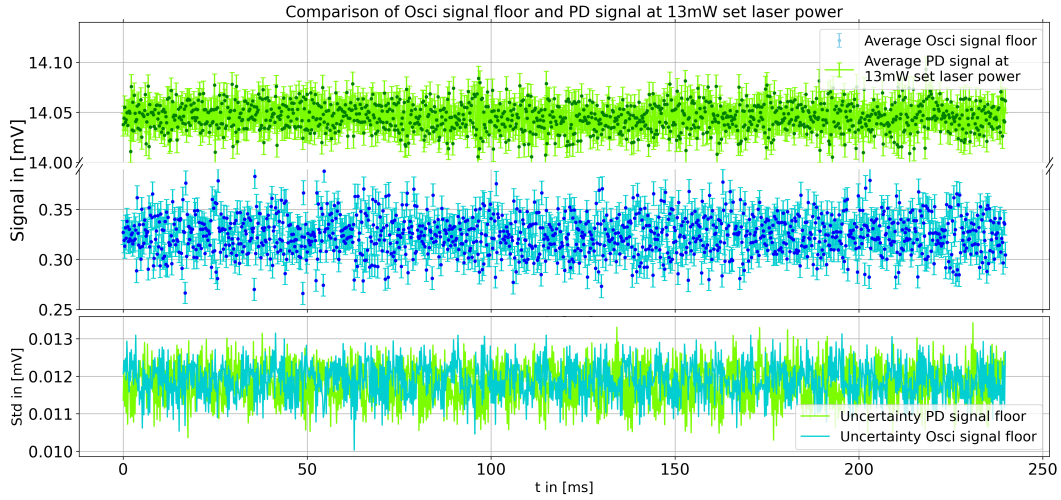


Figure 35: Comparison of the oscilloscope signal noise floor of the photo diode channel (channel 1, see Figure 19b). The green signal shows the fluorescence signal from the photo diode while 13 mW set laser power is applied. The blue signal shows the signal at channel 1 when nothing is connected. Since the uncertainties are comparable, although the signals have different strength, one can conclude that the technical noise is coming from the oscilloscope and any contribution from the PD is negligible. One can denote the average std  $\sigma_{tech} = 0.0118 \text{ mV}$ .

### 5.1.3 Noise floor

When talking about  $SNR$ , the basic noise floor and it's origin is of importance. In Figure 35 the PD signal without applied microwave (and therefore constant fluorescence, no ODMR signal) is plugged into the oscilloscope via a T-connector, while the other end is capped with a  $50\Omega$  resistor. A second measurement shows the noise floor of the same Oscilloscope channel only capped with a  $50\Omega$  resistor. Both signals show similar uncertainties, therefore the noise displayed at the oscilloscope mainly comes from itself and not the recorded fluorescence from the PD. This noise floor is therefore technical noise and can be quantified as

$$\sigma_{tech} = 0.0118 \text{ mV} \quad (5.4)$$

### 5.1.4 The microwave and the spectrum analyser

The Microwave guide is the next part of the setup to characterize. It is important to know how stable the signal is over the coarse of the frequency span, which is used in the experiment. The span fits 400 MHz from 2.6634 GHz to 3.0634 GHz. The main interest is the section to find out the power(-stability) reaching the microwave guide. First, the output power of the microwave circuit, consisting of the spectrum

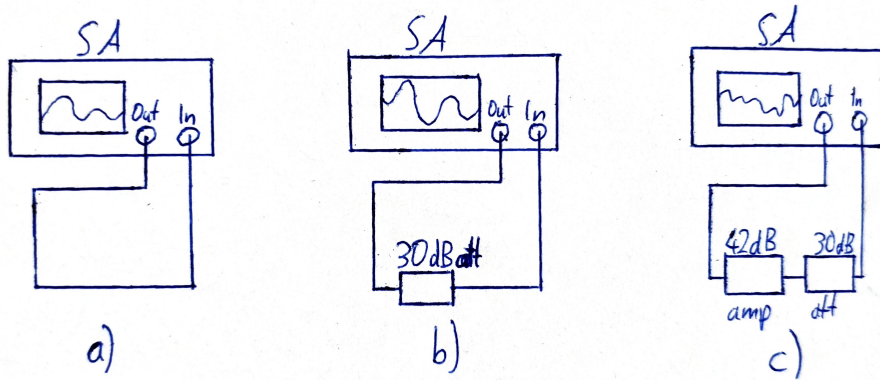


Figure 36: Circuits for MW signal strength estimation. a) This basic circuit measures the signal coming out of the SA. b) Adding the 30 dB attenuator measures the damped signal. The difference of a) and b) gives rise to the signal attenuation of the attenuator. c) In the final step the 42 dB amplifier is added, where the measured signal is amplified and attenuated by the two circuit parts. The signal difference of b) and c) gives rise to the amplification power of the amplifier.

analyser and the 42dB amplifier, needs to be estimated. The starting output of the SA is set to 0 dBm, but the input of it can only handle up to 20 dBm, therefore the 42 dB amplified signal is too strong to display in the SA, therefore a 30 dB attenuator is employed to make the signal detectable. To measure the impact of all three components, three measurements are performed, the circuits are depicted in Figure 36. Each measurement consists of 200 repetitions, which are averaged in each of the 600 points the scale of the SA offers. The resulting curves are depicted in Figure 37. When working with the logarithmic scale of dB/dBm, a good orientation is the  $-3\text{ dB}$  attenuation. At this loss, half of the peak power is lost. The biggest difference in signal strength comes from the 30 dB-attenuated signal of the magnitude of 1.53 dB and is therefore not highly impacting the signal stability. The final plot showing the pure 0 dBm output plus the 42 dB signal (the one reaching the waveguide) has a signal variation  $< 0.6\text{ dB}$ , which is very low. In general, no impact of the dip contrast due to power fluctuations of the microwave signal could be estimated.

For a full characterization, the back-reflected signal from the waveguide needs to be measured to see how much power is lost from the reflection. To accomplish that, a bidirectional coupler from Mini Circuits (ZABDC20-322H-S+) with the specified range of 1.7 – 3.2 GHz is employed. For the consistent measurement of the back reflected signal a reference measurement with a  $50\Omega$ -cap at the output of the bidirectional coupler is performed to have a reference measurement. After that the  $50\Omega$ -cap is removed and the waveguide for the actual measurement is attached to the circuit, as shown in Figure 38.

The measurements depicted in Figure 39 show both very low amplitudes of <

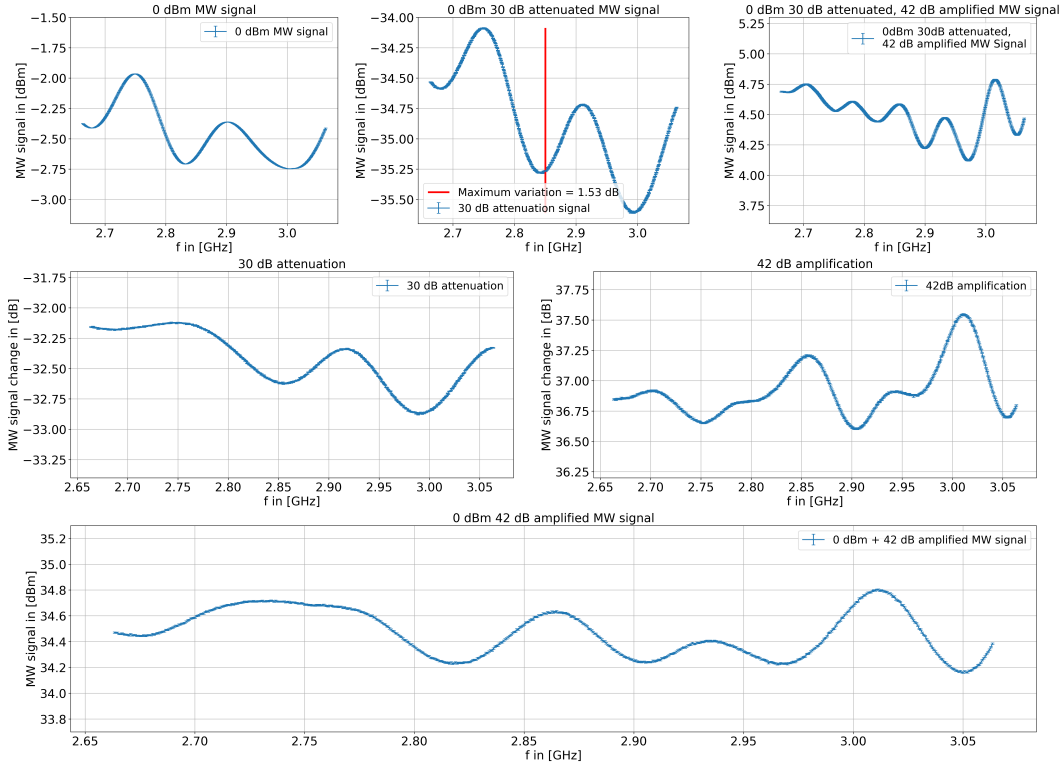


Figure 37: Microwave signal of the setup. For amplitude variation comparison, the range of all y-axes of the plots are 1.7 dBm/dB. The first line represents the three measurements made. From left to right: First, the 0 dBm output signal of the SA (which is around  $-2.5$  dBm). Second, the 0 dBm output of the SA, attenuated by a 30 dB attenuator. The red line here shows the maximal signal variation in dB of all plots. And third, the 0 dBm output signal, attenuated by 30 dB and amplified by 42 dB.

From the differences of these signals, the effective 30 dB attenuation (Second line left) and effective 42 dB amplification (Second line right) were extracted. One can see, that the effective attenuation from the attenuator in this microwave regime is about 2.5 dB stronger than 30 dB, while the amplification of the amplifier is measured about 5 dB weaker than from the specifications. Since the 30 dB attenuator is not present in the measurement setup, the bottom plot represents the microwave signal output before the waveguide, with 0 dBm SA output plus the 42 dB amplification. It is important to note, that the signal variation is not visibly correlating with the different dip strengths of the ODMR signals.

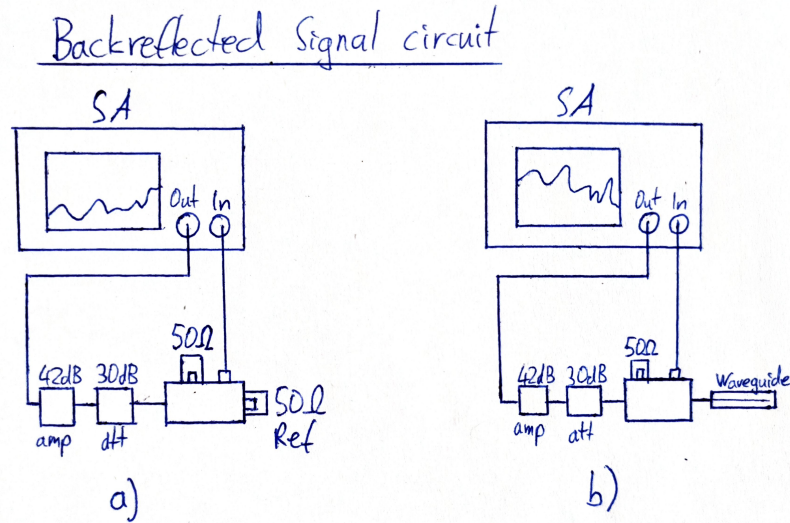


Figure 38: Circuits for MW back-reflected signal strength estimation. The measurements are performed with both amplifier/attenuator from the power measurement. a) For the reference measurement, the output of the bidirectional coupler (bottom right) is capped with a  $50\Omega$ -cap, which is then exchanged for the waveguide in b).

$-34\text{ dB}$ . These are  $\approx 70\text{ dB}$  lower than the signal reaching the waveguide and can therefore be neglected as a potential source of power loss. Overall, the signal reaching the waveguide is stable  $< 0.6\text{ dB}$  and not considerable reflected.

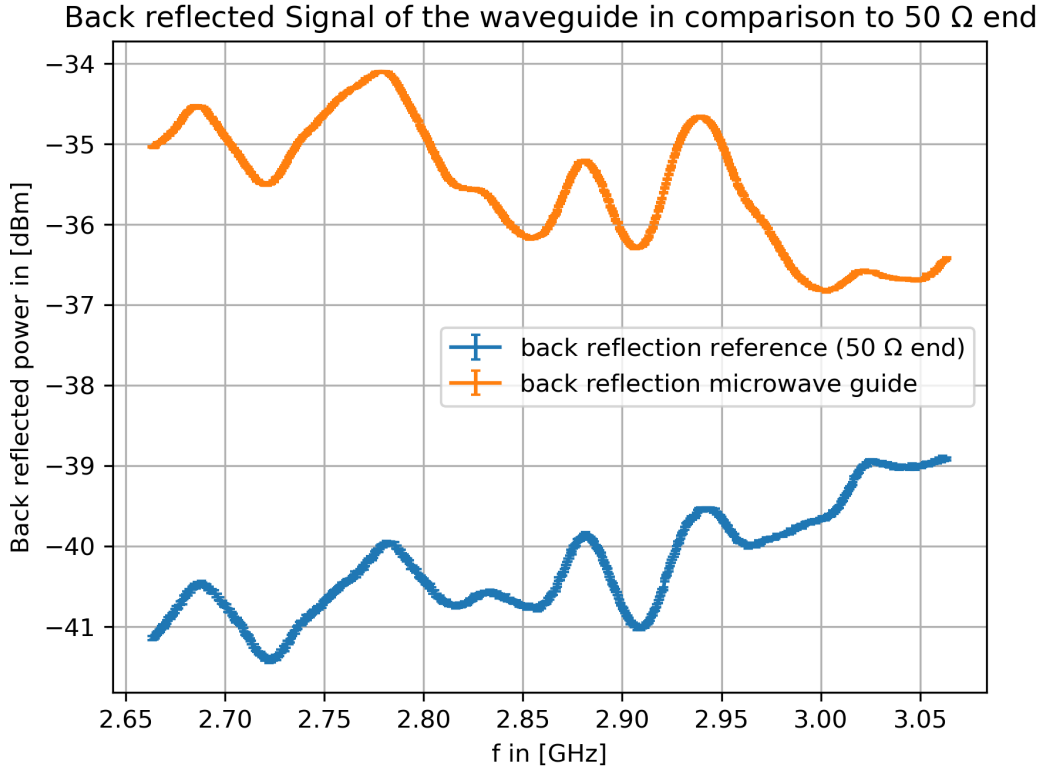


Figure 39: Back-reflected microwave signal of the waveguide, measured with a Bi-directional coupler. The reference measurement (blue) was done with a  $50\ \Omega$  end at the output of the bi-directional coupler. The back-reflected signal of the waveguide in the experiment (orange) shows an higher-than-reference back-reflected signal, which was expected, but this signal is still  $\approx 70$  dB weaker than the input signal reaching the waveguide (last plot in Figure 37) and can therefore be neglected as a source of power loss.

### 5.1.5 Time to frequency conversion

The oscilloscope used to gather the ODMR signals only has a time display, while the ODMR signal in the end should be displayed at a frequency scale. To convert the time to a frequency scale, one needs to extract the start and stop point of the frequency sweep in time. The times and delays that play a role are depicted in Figure 40. The square signal from the function generator triggers both the SA, sweeping over the frequency range for a given duration, and the oscilloscope, resulting in the stable display of both signals on the oscilloscope. For this particular measurement the MW-sweep range was made very small around the 0 G ODMR dip to get steep slopes when the MW-sweep starts and ends to find these points more easily. From there one can identify the delay the SA has between being triggered and sending out the microwave and identify the sweep-duration. One can observe a difference in

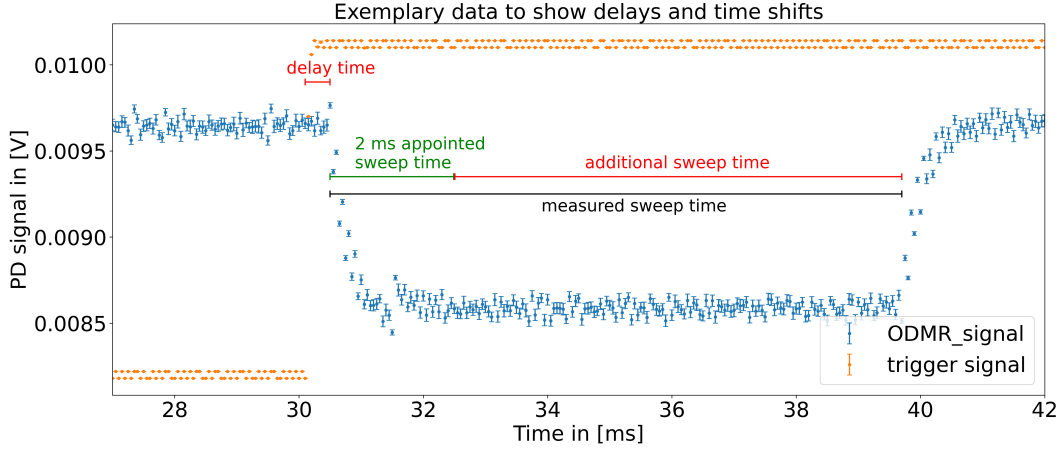


Figure 40: Start, stop and additional sweep time estimation. The square signal (orange) of the function generator externally triggers both the SA, which sweeps then over the frequency range for a given sweep time, and the oscilloscope, resulting in the stable display of both signals on the oscilloscope. For this particular measurement the MW-sweep range was made very small around the 0 G ODMR dip to get steep slopes when the MW-sweep starts and ends to find these points more easily. From there one can identify the delay the SA has between being triggered and sending out the microwave (short red) and identify the sweep-duration, recognizing a difference in measured (black) and set sweep-time (green, here 2 ms). Especially this additional sweep-time is important to quantify when converting the displayed timescale to a frequency range.

measured (black) and set sweep-time (green). Especially this additional sweep-time is important to quantify when converting the displayed timescale to a frequency range.

To collect the ODMR data a sweep-time of 150 ms was used. Performing the experiment described above with a sweep-time of 150 ms 50 times yields the delay time and additional sweep-time of

$$\begin{aligned} t_{\text{delay},150} &= 0.33 \text{ ms} \\ t_{\text{add},150} &= 7.84 \text{ ms} \end{aligned} \quad (5.5)$$

with both uncertainties smaller than 0.2 ms, which is the time-step size of the oscilloscope and therefore can be neglected.

The conversion now works as following:

1. The time of the trigger signal rise is estimated.
2. The delay time is added, giving access to the starting time of the sweep.
3. The sweep time 150 ms and  $t_{\text{add},150}$  are added to the starting time, giving rise to the stop time.

4. With knowledge of both frequencies and times at the start and stop point, a linear fit can be performed and afterwards the whole time scale can be converted to a frequency scale which can be seen in the results part.

This fit is conducted individually for each measurement.

### 5.1.6 Temperature influence

The heating from the coil and the laser causes changes to the system. Especially the signal strength anti-correlates with temperature changes as seen in [Figure 41](#). This mainly is based on thermal expansion of the waveguide, which causes the diamond to move out of the laser beam, hence weakening the fluorescence signal in the PD. When the system reaches equilibrium (no further change of the PD signal), the diamond position can be readjusted to maximum signal and usually stays stable. At later stages of the experiment, especially after enhancing the focus of the excitation laser, the time to reach equilibrium was much shorter, only 10 – 20 min instead of the displayed 80 – 90 min.

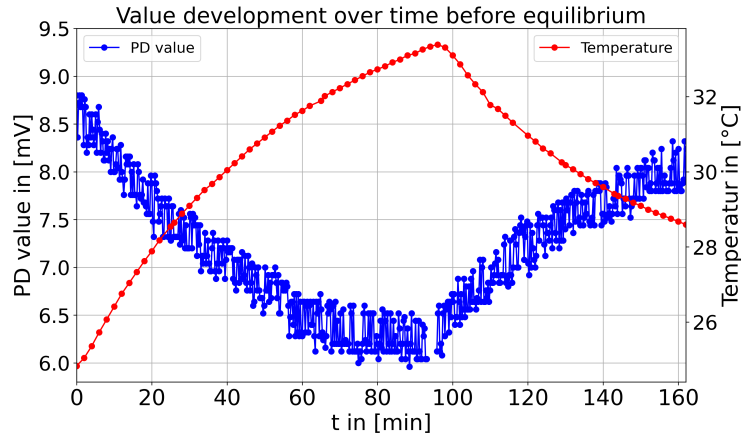


[Figure 41](#): Temperature change during the experiment. The signal strength anti-correlates with temperature changes. This mainly is based on thermal expansion of the waveguide, which causes the diamond to move out of the laser beam, hence weakening the fluorescence signal in the PD. When the system reaches equilibrium (no further change of the PD signal), the diamond position can be readjusted to maximum signal and usually stays stable. At later stages of the experiment, especially after enhancing the focus of the excitation laser, the time to reach equilibrium was much shorter, only 10 – 20 min instead of the displayed 80 – 90 min

The temperature also has reported influence on the  $D_{gs}$  splitting of the ground state manifold [Cambria et al., 2023], but the effect for this temperature difference  $\approx 10^\circ\text{C}$  is much weaker than the measured impact as seen in [subsubsection 5.2.4](#).

## 5.2 Results

The results of this magnetic field sensing are all derived from the ODMR measurements performed for different applied B-fields in the range of  $\approx 0 - 60$  G, which are displayed in Figure 42. For the magnetic field the large coil pair of the setup was employed with a B-field strength per current of  $B/I \approx 30$  G/A at the center [Palani et al., 2022].

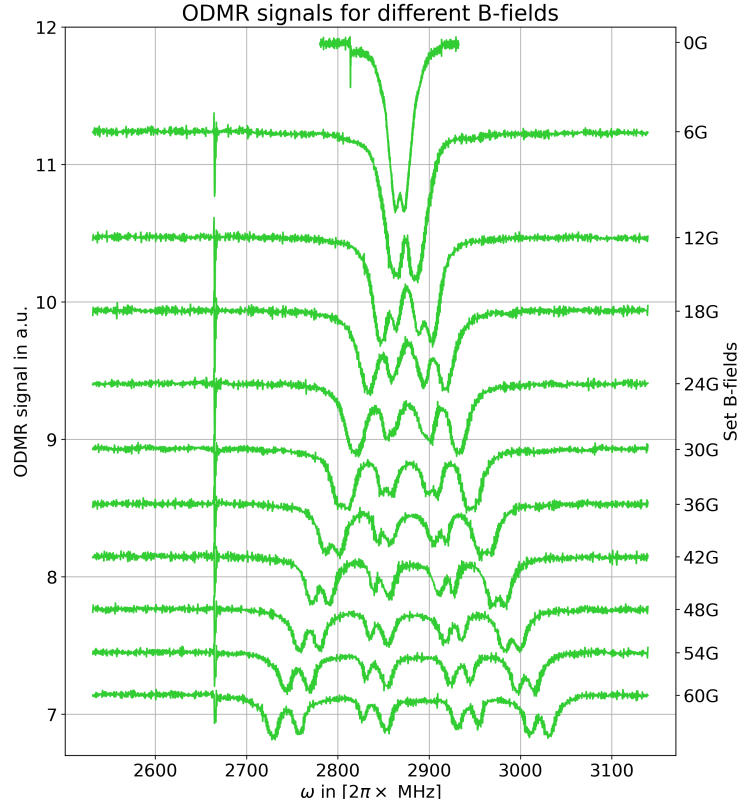


Figure 42: All recorded ODMR signals displayed regarding the frequency. The left y-axis indicates the set B-field for the respective ODMR signal, while the right y-axis shows ODMR signal strength. On the right axis these signals all would have roughly the same baseline but are individually shifted downwards to present them in a contour plot. The relative dip strength is preserved, so with increasing B-field (downwards), the larger splitting and lowered contrast can be seen. The nonlinear arrangement of the B-field ticks may wrongly indicate a quadratic Zeeman effect, which will be negated in the following. The very narrow dips on the left side are artifacts from the trigger function on the oscilloscope.

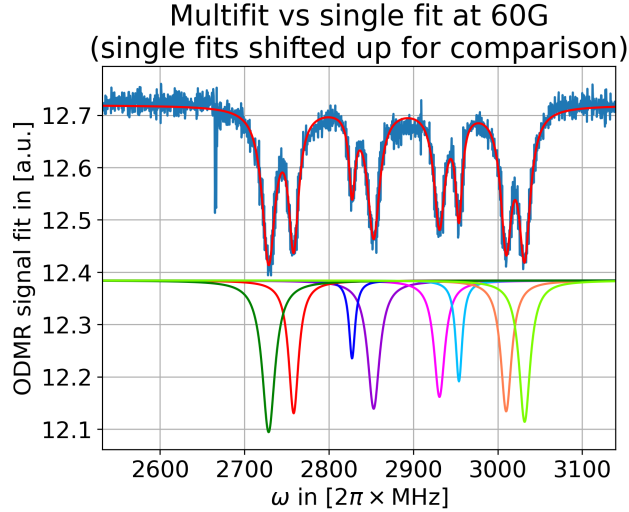


Figure 43: 8-Lorentzian fit for  $B_{\text{set}} = 60$  G signal. Since there are four possible NV-center orientations, the 8 dips belong symmetrically pairwise to one orientation. This is color coded in light and dark green, red, blue and purple. The pair furthest apart from each other belongs to the NV-center orientation mostly aligned with the  $B$ -field direction, while the inner pair is most perpendicular to the  $B$ -field direction. The color coded single Lorentzians plotted are artificially lifted to show the direct comparison of the 8-Lorentzian fit.

### 5.2.1 Lorentzian fits for the data

To extract information, first a sum of Lorentzian functions needs to be fitted to the data. Depending on the dip number, a sum of 2, 4 or 8 Lorentzians have to be fitted like

$$f(\omega) = \left( \sum_{i=1}^{\text{dip number}} -A_i \cdot \left( \frac{1}{\pi} \cdot \frac{\gamma_i}{(\omega - \omega_{0,i})^2 + \gamma_i^2} \right) \right) + h, \quad (5.6)$$

where  $A_i$ ,  $\gamma_i$  and  $\omega_{0,i}$  are the individual fit parameters of scale, FWHM and dip position, respectively and  $h$  is the common offset parameter. In the following there is a focus on the ODMR-signals of  $B_{\text{set}} \geq 30$  G, since for these all 8 dips can be resolved ( $i \in \{1, 2, \dots, 8\}$ ). Further, the fit parameters are checked for explicit dependence of the  $B$ -field. An exemplary fit of the  $B_{\text{set}} = 60$  G signal is shown in Figure 43. Since there are four possible NV-center orientations, the 8 dips belong symmetrically pairwise to one orientation. The pair furthest apart from each other belongs to the NV-center orientation mostly aligned with the  $B$ -field direction, while the inner pair is most perpendicular to the  $B$ -field direction, since the Zeeman-splitting comes from the field projection of the  $B$ -field onto the center axis ( $B_{\parallel}$  in the Hamiltonian Equation 2.12).

The only parameter influenced by the  $B$ -field is the dip position as depicted in Figure 44. One can see the splitting getting larger for larger  $B$ -field, as expected from the Zeeman-effect. The uncertainties are adapted from the Lorentzian fit uncertainties and therefore small, since the noise  $\sigma_{\text{tech}}$  affects only the ODMR signal strength and not the frequency position, at least not in direct manner. The other three fit parameters show no explicit dependency on the magnetic field, as shown in Figure 54.

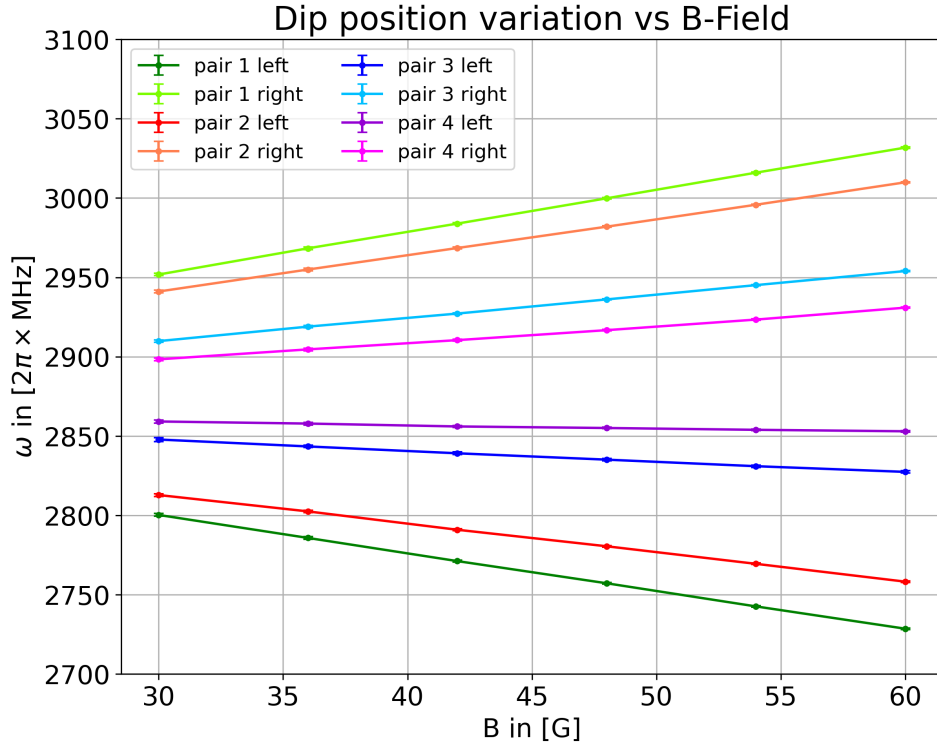


Figure 44: Dip position change under  $B$ -field. One can see the splitting getting larger for larger  $B$ -field, as expected from the Zeeman-effect. The uncertainties are adapted from the Lorentzian fit uncertainties and therefore small, since the noise  $\sigma_{\text{tech}}$  affects only the ODMR signal strength and not the frequency position, at least not in direct manner.

As a next step, the pairwise frequency difference

$$\Delta\omega_j = \omega_{0,\text{pair } j, \text{ left}} - \omega_{0,\text{pair } j, \text{ right}} \quad j \in \{1, 2, 3, 4\} \quad (5.7)$$

to investigate the Zeeman shift and the pairwise center position

$$\omega_{0,\text{mid},j} = \frac{\omega_{\text{pair } j, \text{ left}} + \omega_{0,\text{pair } j, \text{ right}}}{2} \quad j \in \{1, 2, 3, 4\} \quad (5.8)$$

to investigate other B-field related influences are employed.

### 5.2.2 The linear Zeeman effect

From the Hamiltonian in [Equation 2.12](#) the term for the linear Zeeman splitting arises as

$$\mu_B g B_{\parallel,j} = \frac{\Delta\omega_j}{2} \quad (5.9)$$

Which depends on the relative positions of the NV-center direction regarding the B-field direction, expressed by the angle

$$\zeta_j = \arccos\left(\frac{B_{\parallel,j}}{B_0}\right) = \arccos\left(\frac{\Delta\omega_j}{2\mu_B g B_0}\right). \quad (5.10)$$

From [Equation 5.9](#) we can directly extract the sensitivity as

$$S_{\text{ODMR}} = \frac{\Delta\omega_j}{B_{\parallel,j}} = 2 \cdot \mu_B g = 5.606 \text{ MHz/G} \quad (5.11)$$

which only consists of constants in the linear range and is therefore known. Plotting the splitting against  $B_{\text{set}}$  as seen in [Figure 45](#) yields effective sensitivities  $S_{\text{eff},j}(\zeta_j)$  depending on the projection angle  $\zeta_j$  from the slopes of the linear fits. These are smaller than  $S_{\text{ODMR}}$ . The linear fits shows high  $R^2$  values and low residuals in the order of magnitude of the uncertainties and therefore affirm the linear Zeeman effect.

### 5.2.3 $B_0$ reconstruction

With the presented formalism in [Equation 5.9](#) and [Equation 5.10](#) there is a possibility to reconstruct the magnetic field strength  $B_0$  of the external field, since the  $B_{\text{set}}$  values are only based on the  $B/I \approx 30 \text{ G/A}$  field strength per current value from [Palani et al., 2022]. The idea is to variate the  $B_0$  for all  $\zeta_j$  simultaneously in

$$\zeta_j = \arccos\left(\frac{B_{\parallel,j}}{B_0}\right), \quad (5.12)$$

Depending on the value of  $B_0$ , the angles variate.

As presented in [Figure 46](#) the coordinate system of the crystal lattice is introduced, in which the directions of the NV-centers are defined by the lattice structure with the unit vectors  $\hat{e}_{NVj}$ . Further, the direction of a virtual magnetic field  $\vec{B}$  is defined over spherical angles  $\theta_B \in \{0, \pi\}$ ,  $\varphi_B \in \{0, 2\pi\}$  regarding the crystal coordinate system with the unit vector  $\hat{e}_B(\theta_B, \varphi_B)$ . One can now introduce the angles  $\zeta'_j$  between the virtual  $\vec{B}$  and the NV-center directions as

$$\zeta'_j(\theta_B, \varphi_B) = \arccos(\hat{e}_B(\theta_B, \varphi_B) \cdot \hat{e}_{NVj}). \quad (5.13)$$

These angles can be varied by scanning over the full range of  $\theta_B, \varphi_B$ , i.e. rotating the virtual  $\vec{B}$  over the full  $4\pi$  steradians.

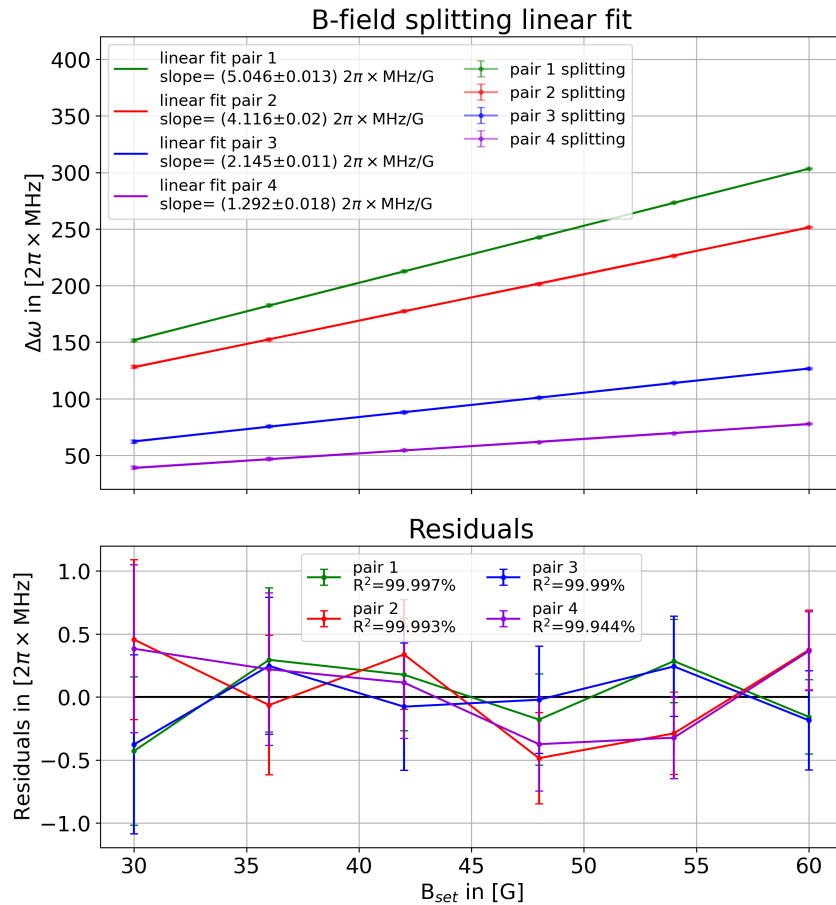


Figure 45:  $\Delta\omega$  vs.  $B_{\text{set}}$  for all pairs. The linear fits to the data are matching with high  $R^2$  values and low residuals in the order of magnitude of the uncertainties, affirming the linear Zeeman effect. The fitted slopes are lower than the sensitivity  $S_{\text{ODMR}}$  which is expected since  $\Delta\omega_j$  is divided by  $B_{\text{set}}$  and not the projected field strength  $B_{\parallel,j}$ .

To compare the  $\zeta_j$  and  $\zeta'_j$  angles, a threshold value  $\epsilon$  of the difference between them is defined as

$$\epsilon > |\zeta_j - \zeta'_j| \quad \forall j. \quad (5.14)$$

Depending on the choice of  $\epsilon$ , for some combinations of  $B_0$  (variation parameter of  $\zeta_j$ ),  $\theta_B$  and  $\varphi_B$  (variation parameters of  $\zeta'_j$ ) the condition stated above is true for all  $j$  (i.e. all four NV-center directions). The more often this condition for a chosen  $B_0$  in a two-dimensional parameter scan of  $\theta_B$  and  $\varphi_B$  is true, the better  $B_0$  is to describe the applied magnetic field. A fulfilled condition is called 'angle pair match'.

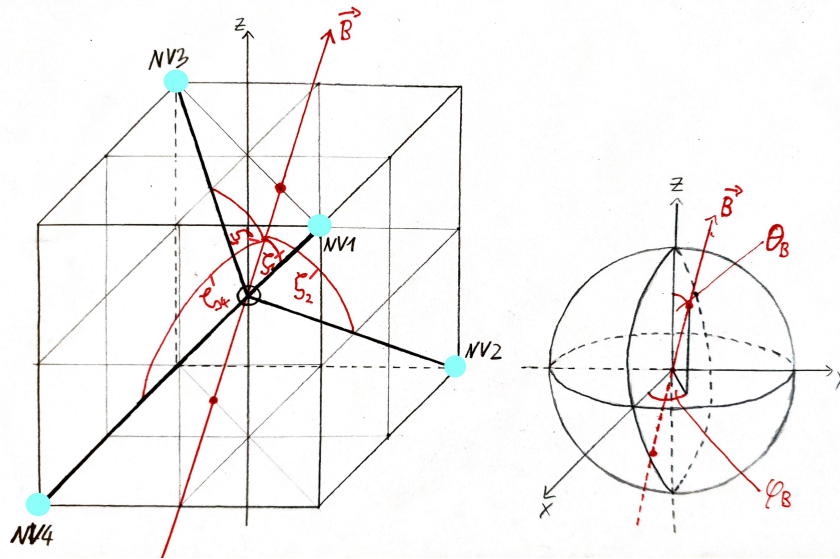


Figure 46: The diamond lattice coordinate system

This algorithm of finding  $B_0$  is split into a coarse and fine scan of the three variation parameters.

The coarse scan goes as follows:

1. Calculate the four  $B_{\parallel,j}$  values from [Equation 5.9](#)
2. Choose for  $\epsilon$  a relatively large value of a few degrees, to ensure the condition is satisfied enough times.
3. For one  $B_{\text{set}}$  value, variate  $B_0$  for  $\approx 15$  values in steps of 1 G around  $B_{\text{set}}$ . For each  $B_0$ , scan the full  $180^\circ, 360^\circ$  range of  $\theta_B$  and  $\varphi_B$ , respectively. As resolution,  $1^\circ$  for both is enough.
4. For each  $B_0$ , sum the number of times, the condition holds true
5. Plot the number of angle pair matches against the  $B_0$  values and identify the  $B_{0,\text{peak}}$  value where the maximum appears. If no maximum is visible, repeat the coarse scan with another range of  $B_0$  values.

This procedure is exemplary displayed in [Figure 47](#). For convenience of this example,  $B_0 = B_{\text{set}} = 60 \text{ G}$  is chosen and the acceptance angle  $\epsilon$  is set to  $8^\circ$ . The right side of the figure shows the angle scan of  $\theta_B$  (y-axis) and  $\varphi_B$  (x-axis). If the condition is true, the position of the angle pair  $\theta_{B,l}, \varphi_{B,l}$  is colored yellow, if it's false, it's colored dark green. The red lines represent the projected quarter areas of the cubic crystal lattice sides, while the cyan dots show the position of the four possible NV-center directions in the lattice. Summing the number of all true events, gives rise to the value in the plot at the right side (as the red arrows indicate). This coarse scan of  $B_0$  indicates the maximum  $B_{0,\text{peak}} \approx 65 \text{ G}$ . The curve indicates a Gaussian shape.

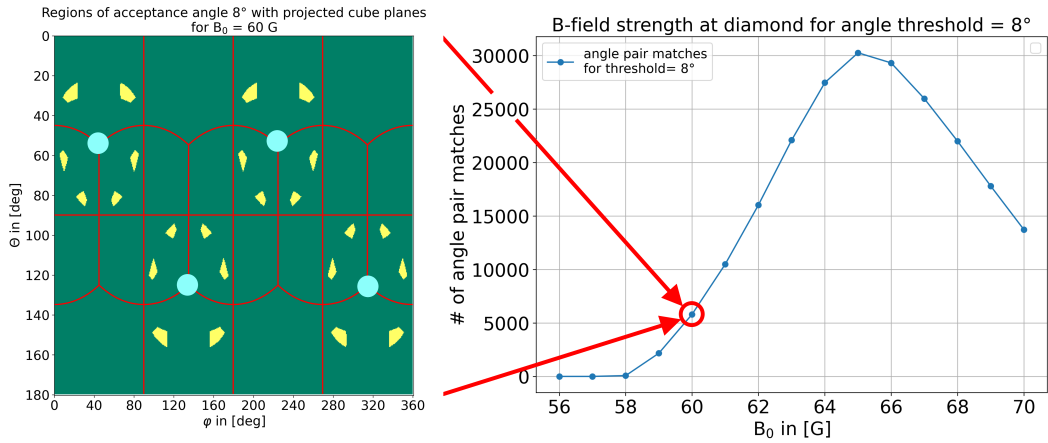


[Figure 47](#): Exemplary coarse  $B_0$  calculation. For convenience of this example,  $B_0 = B_{\text{set}} = 60 \text{ G}$  is chosen and the acceptance angle  $\epsilon$  is set to  $8^\circ$ . The right side of the figure shows the angle scan of  $\theta_B$  (y-axis) and  $\varphi_B$  (x-axis). If the condition is true, the position of the angle pair  $\theta_{B,l}, \varphi_{B,l}$  is colored yellow, if it's false, it's colored dark green. The red lines represent the projected quarter areas of the cubic crystal lattice sides, while the cyan dots show the position of the four possible nitrogen positions in the lattice (compare with [Figure 46](#)). Summing the number of all true events, gives rise to the value in the plot at the right side (as the red arrows indicate). This coarse scan of  $B_0$  indicates the maximum  $B_{0,\text{peak}} \approx 65 \text{ G}$

With the coarse  $B_{0,\text{peak}}$  extracted, the fine tuning goes as follows:

1. Choose a range for  $B_0$  of  $B_{0,\text{peak}} \pm 1 \text{ G}$  with a resolution of 200 steps.
2. Since the  $\Delta\omega_j$  have uncertainties, the calculated  $\zeta_j$  also have propagated uncertainties. From the four uncertainties, the maximum uncertainty is picked as a natural choice for the threshold value  $\epsilon = \sigma_{\zeta,\text{max}}$
3. For the full scan of  $\theta_B$  and  $\varphi_B$ , the resolution is decreased to  $> 1^\circ$ .
4. A Gaussian is fitted to the number of angle pair matches vs.  $B_0$  plot. The position fit parameter indicates the best  $B_0$  to describe the applied magnetic

field, while the fitted  $\sigma$  serves as a good uncertainty of this value.

The example for the  $B_{\text{set}} = 60 \text{ G}$  is continued for the fine tuning and displayed in [Figure 48](#). The Gaussian fit yields a value of

$$B_0 = (65.08 \pm 0.07) \text{ G} \quad (5.15)$$

which is about 5 G stronger than  $B_{\text{set}}$ . To employ the fitted  $\sigma$  from the Gaussian as uncertainty, the ratio of the chosen thresholds  $\epsilon_{c,f}$  and the fitted  $\sigma_{c,f}$  are compared:

$$\begin{aligned} r_c &= \frac{\epsilon_c}{\sigma_c} = \frac{8^\circ}{3.35 \text{ G}} = 2.39^\circ/\text{G} \\ r_f &= \frac{\epsilon_f}{\sigma_f} = \frac{0.234^\circ}{0.067 \text{ G}} = 3.49^\circ/\text{G} \end{aligned} \quad (5.16)$$

The ratios are not the same so there is not a linear relation between the threshold (with that also the angle uncertainties for the fine calculation) and the fitted  $\sigma$  value. But the ratios are still in the same order of magnitude, so employing the fitted  $\sigma$  values from the fit is a educated guess of the uncertainty of the reconstructed  $B_0$  field strength.

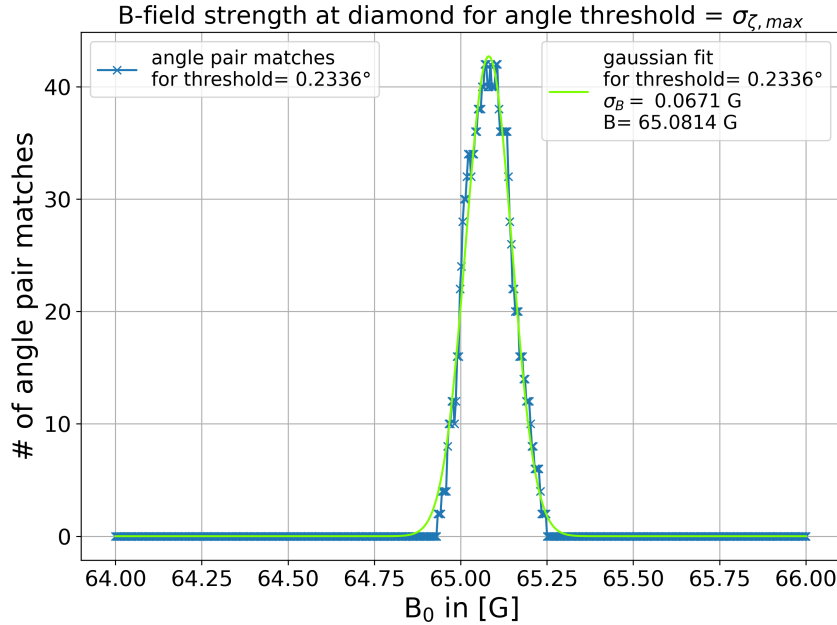


[Figure 48](#): The fine  $B_0$  calculation from a Gaussian fit. The data shows a slight skewness, but the use of a Gaussian is still appropriate. The found magnetic field is  $B_0 = (65.08 \pm 0.07) \text{ G}$ . In comparison to the coarse calculation, the lower threshold yields smaller peaks, strengthening the choice to take the fit parameter  $\sigma$  of the fit as uncertainty for the  $B_0$ .

In [Figure 17](#) the ODMR signal without any applied magnetic field from the coils is seen, which already possesses a splitting, which is mostly due to strain [Doherty et al., 2013]. Since it is also present when a  $B$ -field is applied, this should be taken into account by subtracting it as a offset. The splitting is

$$\Delta\omega_{0G} = (12.76 \pm 0.25) \text{ MHz} \quad (5.17)$$

and with the sensitivity  $S_{\text{ODMR}}$  this is converted to

$$\tilde{B}_{\text{offset}} = \frac{\Delta\omega_{0G}}{S_{\text{ODMR}}} = (2.28 \pm 0.06) \text{ G}. \quad (5.18)$$

Note, that  $\tilde{B}_{\text{offset}}$  is not directly a magnetic field but a offset from other sources which needs to be taken into account. The final  $B$ -field is

$$B_{\text{final}} = B_0 - \tilde{B}_{\text{offset}} = (62.80 \pm 0.09) \text{ G} \quad (5.19)$$

This gives rise to a relative uncertainty of the  $\approx 10^{-3}$  and is therefore 3 orders of magnitude worse than achieved with the ion. All recalculations of the magnetic field for  $B_{\text{set}} \geq 30 \text{ G}$  are gathered in [Table 3](#). The recalculation method was only used for splittings with all 8 dips visible. For lower magnetic fields, the indistinguishably of neighboring dips results in a lower number of fitted dips. the reconstruction method relies on the relative direction of all 4 possible NV-centers, to loosing one or more possible directions make the reconstruction in it's current form not applicable. In general this might be possible, but will come along with higher uncertainties.

$B_{\text{set}}$ in [G]	$B_{\text{final}}$ in [G]
30	$30.43 \pm 0.21$
36	$36.95 \pm 0.21$
42	$43.43 \pm 0.16$
48	$49.77 \pm 0.13$
54	$56.33 \pm 0.11$
60	$62.80 \pm 0.09$

[Table 3](#): Recalculated B-field values from ODMR signal. At first glance surprising is the descending uncertainty for rising B-fields. The major uncertainties from these values originates in the fit uncertainty of the dip positions  $\omega_0$ . Since the for higher  $B$ -fields the dips are more separated, the uncertainties from the fit are also lower, resulting in the descending of  $\sigma_{B_{\text{final}}}$ .

With these values, a redefinition of the B-field strength per current of  $B/I \approx 30 \text{ G/A}$  can be made resulting in

$$(32.35 \pm 0.06) \text{ G/A}, \quad (5.20)$$

as shown in [Figure 49](#)

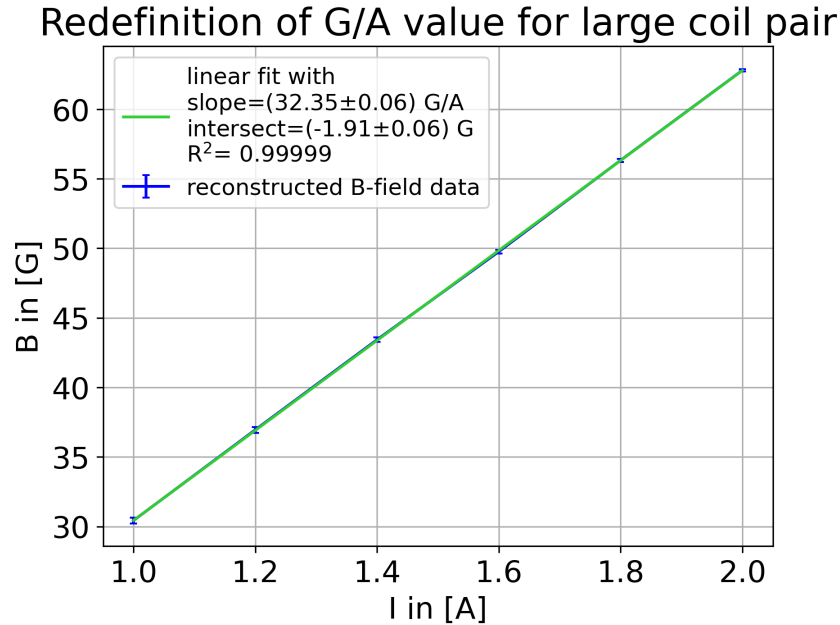


Figure 49: Redefinition of the G/A value for the large coil. The fit features a high  $R^2$  value and residuals on the order of the uncertainties.

#### 5.2.4 Other B-field related influences

Next to the Zeeman shift, a shift of the center frequency as defined in [Equation 5.8](#) is visible as shown in [Figure 50](#). Each individual NV-center-direction experiences a shift of the center frequency, which all seem to be linear with the  $B$ -field but of different slope. The NV-center orientations with the least Zeeman split (pair 3+4) experience the highest slope of the center frequency shift.

Two possibilities are possible to cause this shift as showed in [Figure 51](#):

1. The ZFS parameter  $D_{\text{gs}}$  is rising with the  $B$ -field, causing the center frequency to shift, assuming a symmetrical splitting of the  $|\pm 1\rangle$  states.
2. The B-field changes the splitting of the  $|\pm 1\rangle$  asymmetrically around the ZFS depending on its strength. A then calculated center frequency with the false assumption of a symmetrical splitting sees an effective rise with stronger  $B$ -fields.

For both possibilities, the observed Zeeman splitting is unaffected.

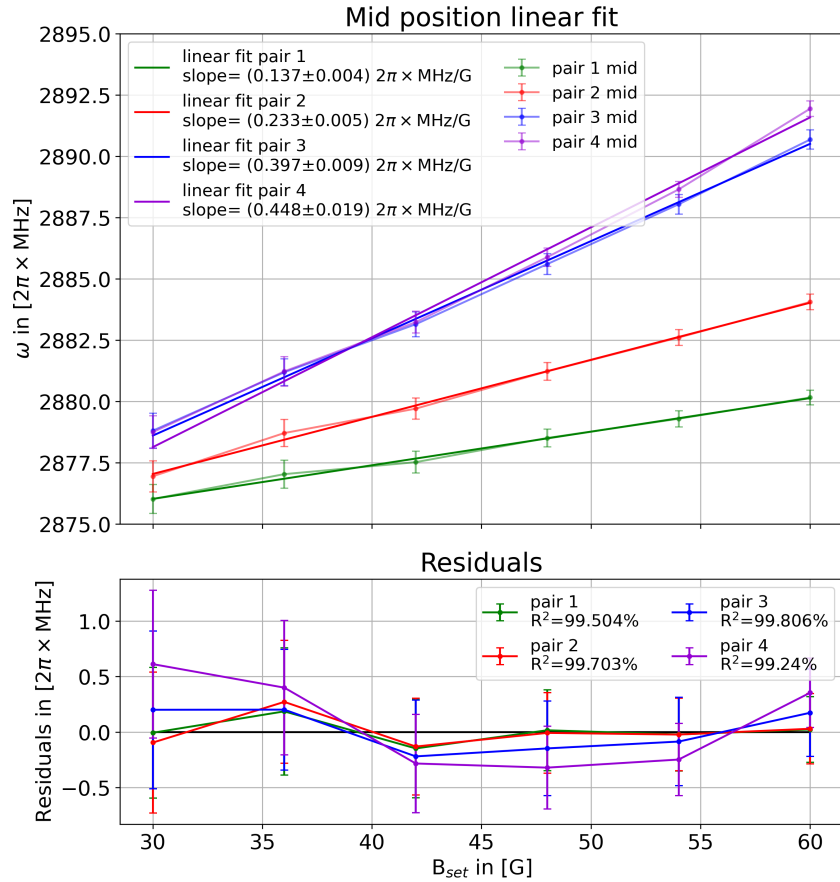


Figure 50: Shift of the center frequency dependent on  $B$ -field. Each individual NV-center-direction experiences a shift of the center frequency, which all seem to be linear with the  $B$ -field but of different slope.

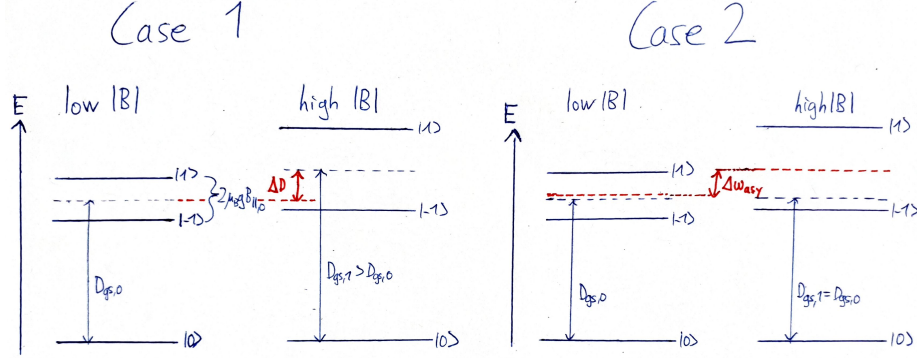


Figure 51: Center frequency shift possibilities displayed in an energy level diagram. Case 1 visualizes the shift of the center frequency due to shifts of the ZFS parameter  $D_{gs}$ . Case 2 shows an asymmetric shift of the  $|\pm 1\rangle$  levels around the ZFS. A calculated center frequency is rising for stronger  $B$ -fields due to this.

For case 1, the influence of the temperature on  $D_{gs}$  is reported [Doherty et al., 2013]. This is relevant, because for higher applied B-fields, a stronger current is going through the coils, causing more heating of the environment, as measured in Figure 41. This still does not explain the orientation-dependent differences. Furthermore, an analytical expression for the temperature dependence of  $D_{gs}$  was introduced by [Cambria et al., 2023]. For the measured temperature changes of  $\approx 10 - 15$  °C at room temperature, the change is  $> 1$  MHz and has a negative sign, which is too weak and in the wrong direction as measured.

For case 2 the Hamiltonian from Equation 2.12 is employed. Applying all influences of the main and off diagonal entries to the states  $|0\rangle$ ,  $|\pm 1\rangle$  yields

$$\begin{aligned} \text{I: } & \left( \frac{D_{gs}}{3} + \mu_B g B_{||} + \frac{1}{\sqrt{2}} \mu_B g B_{\perp} \right) |1\rangle \\ \text{II: } & \left( -\frac{2D_{gs}}{3} + \frac{2}{\sqrt{2}} \mu_B g B_{\perp} \right) |0\rangle \\ \text{III: } & \left( \frac{D_{gs}}{3} - \mu_B g B_{||} + \frac{1}{\sqrt{2}} \mu_B g B_{\perp} \right) |-1\rangle. \end{aligned} \quad (5.21)$$

Calculating the energy differences between  $|0\rangle$  and  $|\pm 1\rangle$  yields

$$\begin{aligned} \text{I-II: } & D_{gs} + \mu_B g B_{||} - \frac{1}{\sqrt{2}} \mu_B g B_{\perp} \\ \text{III-II: } & D_{gs} - \mu_B g B_{||} - \frac{1}{\sqrt{2}} \mu_B g B_{\perp}, \end{aligned} \quad (5.22)$$

introducing the asymmetric term

$$\omega_{asy} = -\frac{1}{\sqrt{2}} \mu_B g B_{\perp}. \quad (5.23)$$

The fact, that the shift is stronger depending on the perpendicular magnetic field explains the steeper slope for the pairs with low Zeeman splitting. Qualitatively, the observed effect is described by the off-diagonal Hamiltonian entries. To find a quantitative description for the measured values, a prefactor, one could say a coupling strength, needs to be introduced like

$$\omega_{\text{asy, eff}} = \kappa \cdot \omega_{\text{asy}} \quad (5.24)$$

No in depth analysis was made to find this prefactor, but as a *preliminary result*

$$\kappa = -\frac{1}{2 \cdot \left( \frac{B_{\parallel}}{B_{\perp}} + 2 \right)} \quad (5.25)$$

worked surprisingly well. The minus comes from the fact, that the base definition of the off-diagonal elements introduce a lowering of the center frequency for increased  $B$ -fields, which needs to be inverted. The factor was found when comparing the ratio of the perpendicular fields and the actual shifts with the ratio of  $B_{\parallel}$  and  $B_{\perp}$ . This part opens up room for further investigations beyond the scope of this thesis. If one could find an analytical expression for the  $\kappa$  this gives rise to  $B_{\perp}$  and the magnetic field strength could be calculated with much less effort than presented above as  $B_0 = \sqrt{B_{\parallel}^2 + B_{\perp}^2}$ .

## 6 Summary and Outlook

To summarize the results of this thesis, first the magnetic field setup for the Octagon was conceptualized and built. The magnets were chosen to have a B-field  $< 109.64$  G at the minimum distance  $d_{\min} = 254.8$  mm of the chamber. The tuning parameters for the setup, namely the distance between magnets and the current of the coils are summarized and compared to the Bermuda setup in [Table 4](#).

	Octagon	Bermuda
distance tuning of the magnets	$-(1.943 \pm 0.015)$ G/turn	$\approx -2.2$ G/turn
current tuning of the coils	$(0.744 \pm 0.016)$ G/A	$\approx 2.6$ G/A

Table 4: Magnetic field setup summary. The values for Bermuda are from [Hakelberg et al., 2018]. The current tuning for the coils was also measured as part of the frequency scan at the Bermuda setup to yield  $\frac{2.653(11)}{G/A}$ , which is comparable with the paper value.

Although these values apply for different setups, it was the initial aim to built a comparable magnetic field setup. The distance tuning of the magnets is quite comparable, while the current tuning is weaker for the Octagon than the Bermuda

setup. With the aim to stay below currents of 100 mA due to heating, a maximum variation of  $\pm 0.074$  G could be achieved. This means the coarse tuning of the magnets needs to be more precise or this current limit is lifted up. As a next step, this magnetic field setup should be tested with an ion, as soon as the Octagon chamber has a trap chip inside and reached ultra high vacuum to trap ions.

Next, the different quantum sensors are compared for their sensitivities and their precision to measure a  $B$ -field, which are listed in [Table 5](#).

	$S$ [ $2\pi \times \text{MHz}/\text{G}$ ]	$\sigma_{\text{rel}}$ of $B_{\text{measured}}$	B-field regime
$^{25}\text{Mg}^+$	$(-2.175\,61 \pm 0.000\,53)$	$2.1 \times 10^{-6}$	$\approx 109$ G (intermediate regime)
$\text{NV}^-$	5.606	$\geq 1 \times 10^{-3}$	0 – 60 G (Linear Zeeman effect)

Table 5: Summary of the quantum sensor properties.

The higher sensitivity of the NV-centers is surprising, but also shows that not sensitivity alone gives rise to a precise measurement of a quantity, but also the noise reduction or hindering circumstances (like peak overlap of the ODMR signal dips) play their role. Therefore, the ion's relative uncertainty is three orders of magnitude lower than the one of the NV-centers. Regarding precision, the ion is still the better sensor. There are other terms like flexibility in sensing, which can be discussed, i.e. the adjustment of sensitivity to different sensing requirements. For the ion, this task is relatively straight forward, since every transition in the ground state manifold can be picked as a qubit. These transitions come along with different sensitivities depending on the Breit-Rabi formula, offering discrete choices of sensitivity. For the NV-centers, the sensitivity depends on the orientation of the NV-center axis regarding the magnetic field. Especially when thinking towards single  $\text{NV}^-$  sensing, the change of the relative direction gives rise to a continuous sensitivity range like

$$S_{\text{ODMR, eff}}(\zeta) = \frac{\Delta\omega(\zeta)}{B_0} = \frac{\Delta\omega}{B_0} \cos(\zeta) \in [0, 2\mu_B g] \quad (6.1)$$

A last point is the practicability of the platform for sensing applications. The ion needs more or less a whole laboratory including the vacuum chamber and all the optics to cool and address the energy levels. Unless this is built explicitly to test e.g. coil pairs or other magnetic equipment which is easily (de-)mountable to the chamber, it has less practical use. The NV-centers on the other hand are working on room temperature without problems and are down scalable towards single NV-centers in diamonds. This has the possibility to even have senior gadgets carried by hand or being used system-integrated on smallest space.

The extracted coherence time of the  $|3, 3\rangle \leftrightarrow |2, 2\rangle$  transition is  $T_{2*} = (378.18 \pm 55.71)$   $\mu\text{s}$ . At the same trap in [Hakelberg et al., 2018] the coherence time is reported as  $T_{2,\text{comp}*} = (420 \pm 60)$   $\mu\text{s}$ . The value is slightly higher, but agrees within

$1\sigma$ . The uncertainty is comparable large with about  $\approx 15\%$ .

The self created reconstruction of the B-field is also mentionable. It is a nice way to get an idea of the magnetic field, but is far from real time application. For the fine step, up to billions of scalar products and thresholds have to be calculated and checked, resulting in few-hour-long calculations of the code.

At last it was possible to identify off-diagonal influences of the NV<sup>-</sup>-center Hamiltonian from the data. These asymmetric  $|\pm 1\rangle$  splittings around the ZFS value  $D_{\text{gs}}$  have the possibility to give rise to the perpendicular  $B$ -field strength  $B_{\perp}$ , if an analytical expression for the coupling strength  $\kappa$  could be found. This enables the calculation of the magnetic field strength  $B_0$  from the Pythagoras equation and  $B_{\parallel}$  and  $B_{\perp}$  and would make the time-intense calculation mentioned before obsolete. This is an interesting project to investigate further.

## References

- Bunea, A.-C., Neculoiu, D., Lahti, M., & Vaha-Heikkila, T. (2014). Low temperature co-fired ceramic antenna for 35 ghz applications with a wideband gcpw to stripline transition. *Romanian Journal of Information Science and Technology*, 17, 305–319.
- Cambria, M. C., Thiering, G., Norambuena, A., Dinani, H. T., Gardill, A., Kemeny, I., Lordi, V., Gali, Maze, J. R., & Kolkowitz, S. (2023). Physically motivated analytical expression for the temperature dependence of the zero-field splitting of the nitrogen-vacancy center in diamond. *Physical Review B*, 108, L180102. <https://doi.org/10.1103/PHYSREVB.108.L180102/FIGURES/4/MEDIUM>
- Degen, C. L., Reinhard, F., & Cappellaro, P. (2017). Quantum sensing. *Reviews of Modern Physics*, 89, 035002. <https://doi.org/10.1103/RevModPhys.89.035002>
- Delone, N. B., & Krainov, V. P. (1999). Ac stark shift of atomic energy levels. *Physics-Uspekhi*, 42, 669–687. <https://doi.org/10.1070/PU1999V04N07ABEH000557/XML>
- Demtröder, W. (2013). *Experimentalphysik 2*. Springer Berlin Heidelberg. <https://doi.org/10.1007/978-3-642-29944-5>
- DiVincenzo, D. P. (2000). The physical implementation of quantum computation. *Fortschritte der Physik*, 48, 771–783. [https://doi.org/10.1002/1521-3978\(200009\)48:9/11<771::AID-PROP771>3.0.CO;2-E](https://doi.org/10.1002/1521-3978(200009)48:9/11<771::AID-PROP771>3.0.CO;2-E)
- Doherty, M. W., Dolde, F., Fedder, H., Jelezko, F., Wrachtrup, J., Manson, N. B., & Hollenberg, L. C. (2012). Theory of the ground-state spin of the nv - center in diamond. *Physical Review B - Condensed Matter and Materials Physics*, 85, 205203. <https://doi.org/10.1103/PHYSREVB.85.205203/FIGURES/9/MEDIUM>
- Doherty, M. W., Manson, N. B., Delaney, P., Jelezko, F., Wrachtrup, J., & Hollenberg, L. C. (2013). The nitrogen-vacancy colour centre in diamond - sciencedirect. *Elsevier Physics Reports* 528, 1–45. <https://doi.org/https://doi.org/10.1016/j.physrep.2013.02.001>
- Eisenhart, L. (2022, December). *Probing magnetic fields near atom traps via commercially available sensor modules*.
- Hakelberg, F., Kiefer, P., Wittemer, M., Schaetz, T., & Warring, U. (2018). Hybrid setup for stable magnetic fields enabling robust quantum control. *Scientific Reports* 2018 8:1, 8, 1–8. <https://doi.org/10.1038/s41598-018-22671-5>
- Hall, E. H. (1879). On a new action of the magnet on electric currents. *American Journal of Mathematics*, 2, 287. <https://doi.org/10.2307/2369245>
- Itano, W. M., Bergquist, J. C., Bollinger, J. J., Gilligan, J. M., Heinzen, D. J., Moore, F. L., Raizen, M. G., & Wineland, D. J. (1993). Quantum projection noise: Population fluctuations in two-level systems. *Physical Review A*, 47, 3554. <https://doi.org/10.1103/PhysRevA.47.3554>

- Jarmola, A., Berzins, A., Smits, J., Smits, K., Prikulis, J., Gahbauer, F., Ferber, R., Erts, D., Auzinsh, M., & Budker, D. (2015). Longitudinal spin-relaxation in nitrogen-vacancy centers in electron irradiated diamond. *Applied Physics Letters*, 107. <https://doi.org/10.1063/1.4937489>
- Karpfinger, C. (2022). Fouriertransformation i. *Höhere Mathematik in Rezepten*, 853–862. [https://doi.org/10.1007/978-3-662-63305-2\\_76](https://doi.org/10.1007/978-3-662-63305-2_76)
- Meschede, D. (2015). *Gerthsen physik*. Springer Berlin Heidelberg. <https://doi.org/10.1007/978-3-662-45977-5>
- Palani, D., Das, A., Schroeder, J.-P., Orlov, O., & Warring, U. (2022, March). *Master lab: Diamonds for sensing applications*.
- Pham, L. M. (2013). Magnetic field sensing with nitrogen-vacancy color centers in diamond. <https://dash.harvard.edu/handle/1/11051173>
- Rabi, I. I., Zacharias, J. R., Millman, S., & Kusch, P. (1938). A new method of measuring nuclear magnetic moment. *Physical Review*, 53, 318. <https://doi.org/10.1103/PhysRev.53.318>
- Ramsey, N. F. (1950). A molecular beam resonance method with separated oscillating fields. *Physical Review*, 78, 695. <https://doi.org/10.1103/PhysRev.78.695>
- Schirhagl, R., Chang, K., Loretz, M., & Degen, C. L. (2014). Nitrogen-vacancy centers in diamond: Nanoscale sensors for physics and biology. *Annual Review of Physical Chemistry*, 65, 83–105. <https://doi.org/10.1146/annurev-physchem-040513-103659>
- Schmid-Gaiser, S. (2024). *Elektrowissen haloeffekt*. <https://elektro-wissen.de/Elekrotechnik/Hall-Effekt.php>
- Segawa, T. F., & Igarashi, R. (2023). Nanoscale quantum sensing with nitrogen-vacancy centers in nanodiamonds – a magnetic resonance perspective. *Progress in Nuclear Magnetic Resonance Spectroscopy*, 134-135, 20–38. <https://doi.org/10.1016/J.PNMRS.2022.12.001>
- Wittemer, M. (2019). *Particle creation and memory effects in a trapped ion quantum simulator*.

## Appendix

### The unfocused excitation laser

With an unfocused excitation laser beam out of the fiber coupler, the beam waist can not be focused thin enough to hit only a single diamond. The resulting ODMR spectra are blurred due to many diamonds contributing the signal, which all posses different intrinsic NV-center directions and therefore have their own ODMR peak position due to their respective direction to the applied  $B$ -field.

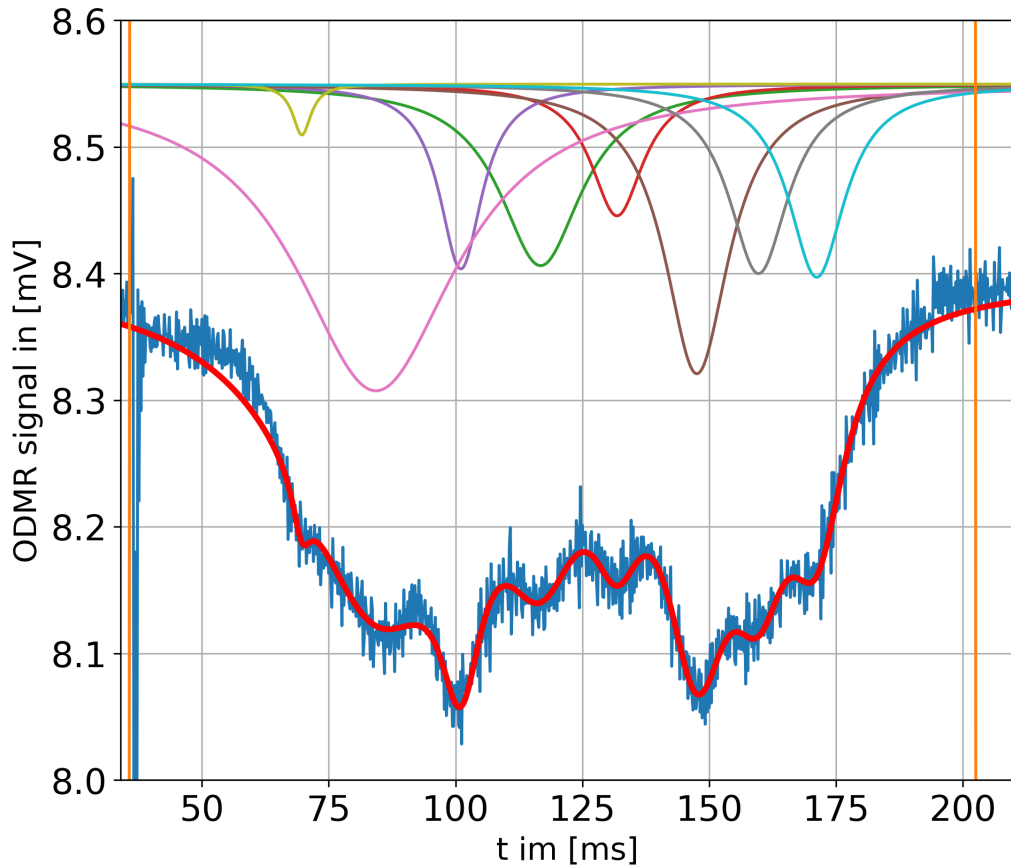


Figure 52: Blurred ODMR signal due to an unfocused laser beam. Fluorescence light from multiple diamonds is gathered, each with different orientations and therefore shifted ODMR dips blur the signal

**center shift due to unequal coils**

Two coils with the same winding number, but different geometries resulting from different cable thicknesses have a resulting shift of the B-field minimum, as the simulation with matching values from the occurred situation shows below. A shift of about 1 cm occurred, which is not bearable and led to the decision to rewind the top coil with the same thick wire.

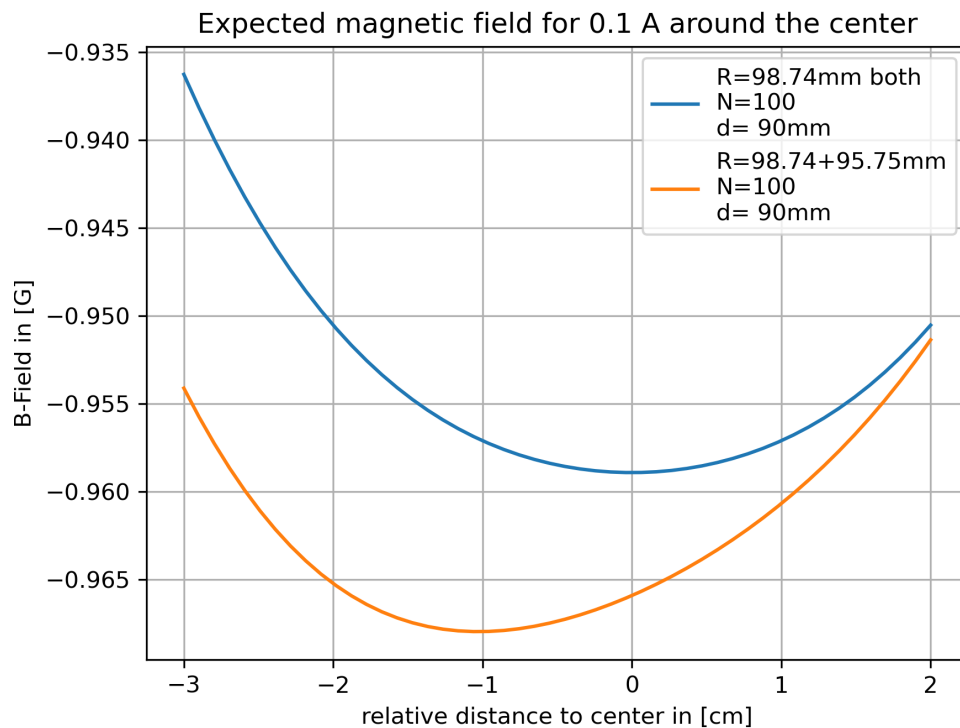


Figure 53: center shift due to different coils

### Other fit parameters of the lorentzian fits

As a dependence on the peakposition  $\omega_j$  regarding the  $B$ -field was recorded, the other fitparameters are not influcened as seen below. The  $\gamma$  and  $A$ - values show some kind of correlation seen for their anti-correlative behaviour in pair 3.

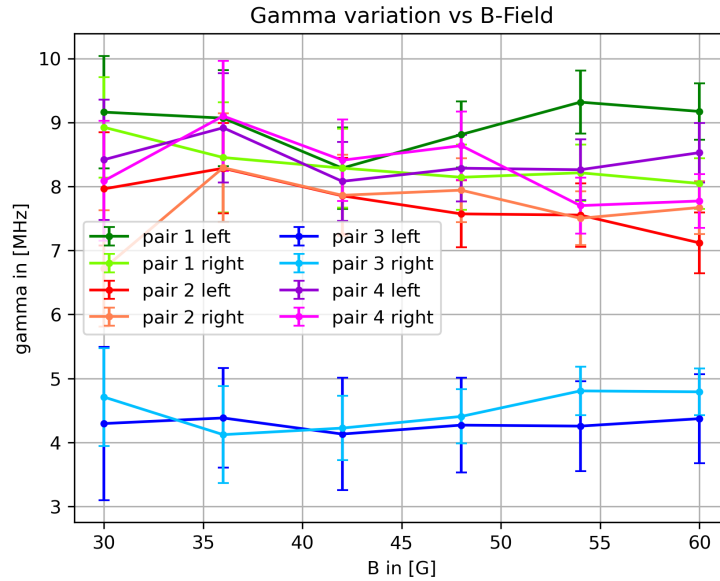


Figure 54: Gamma variation vs B-Field.

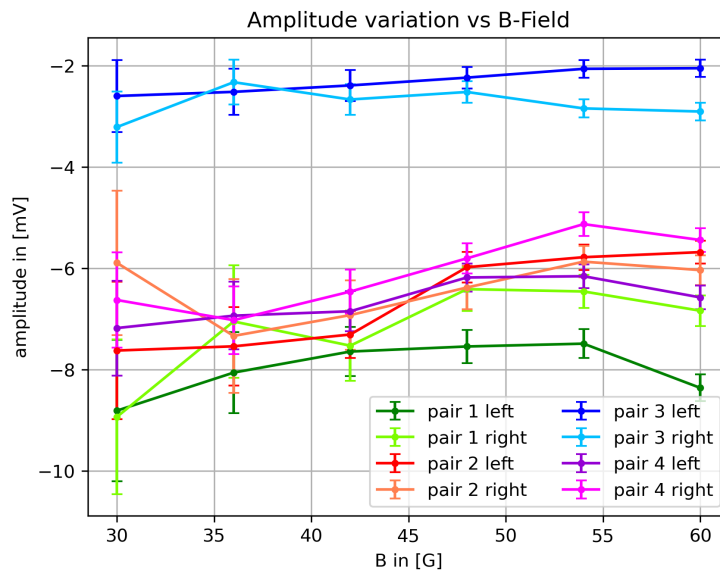


Figure 55: Amplitude variation vs B-Field

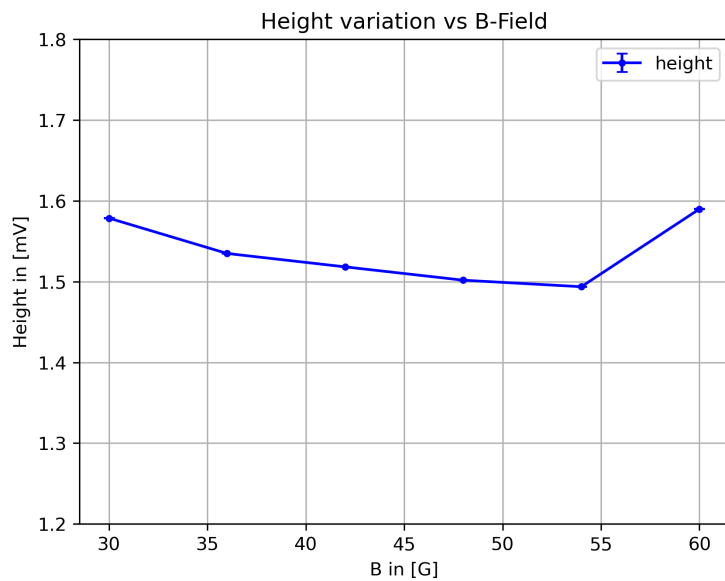


Figure 56: Height variation vs B-Field

## Danksagung

*"All that is gold does not glitter,  
Not all those who wander are lost"  
~ J.R.R. Tolkien, The Fellowship of the Ring*

An dieser Stelle möchte ich allen danken, die mich tatkräftig unterstützt haben in diesem Jahr der Masterarbeit. Besonderer Dank gilt Tobias Schätz, Ulrich Warring, Apruba Das, Deviprasath Palani und Florian Hasse, die mit ihren doch teils sehr verschiedenen Sichtweisen als der Meinen den Blick über den Tellerrand ermöglicht haben. Noch glücklicher hat mich in diesem Jahr gemacht, dass neben Arbeitskollegen auch viele Freunde Teil dieser Arbeitsgruppe geworden sind, um eine Masterarbeit zu schreiben. Namentlich sind dies Leon Göpfert, Freddy Dörr, Andreas Weber, Jonathan Grieshaber und Lucas Eisenhart. Ich danke euch für die schöne gemeinsame Zeit des Experimentierens, Arbeitens und Spaß habens im 4. Stock des GuMies. Auch danke ich allen Freunden an und außerhalb der Physik und meiner Familie für die Unterstützung in der finalen Phase des Studiums. Besonderer möchte ich Jonas Boßerhoff danken, meinem besten Freund, der seit Februar nicht mehr unter uns weilt, RIP.

Jonas, diese Arbeit ist für dich!

